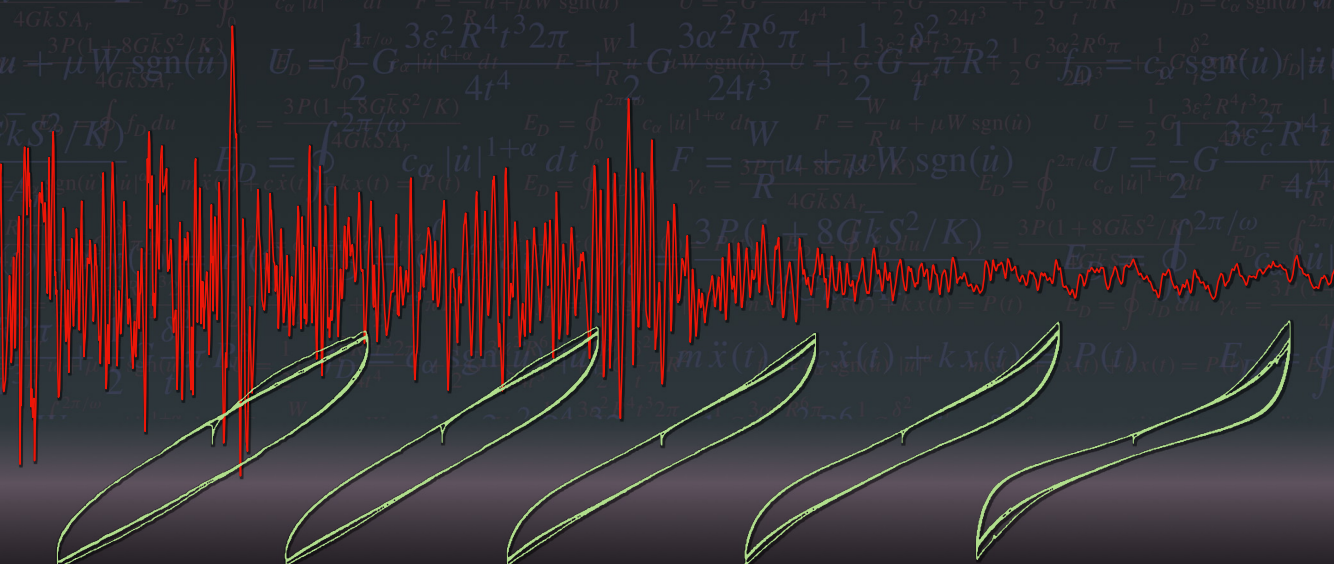


THE JOURNAL OF THE ANTI-SEISMIC SYSTEMS INTERNATIONAL SOCIETY (ASSISI)

Seismic Isolation and Protection Systems



vol 2, no 1

2011

SEISMIC ISOLATION AND PROTECTIVE SYSTEMS

pjm.math.berkeley.edu/siaps

EDITOR-IN-CHIEF

GAINMARIO BENZONI University of California, San Diego, USA

ASSOCIATE EDITORS

JAMES M. KELLY University of California, Berkeley, USA
DAVID WHITTAKER Technical Director of Structural Engineering, Beca, New Zealand
MUSTAFA ERDIK Bogazici University, Istanbul, Turkey

ADDITIONAL EDITORIAL BOARD MEMBERS

MASSIMO FORNI ENEA, Italy
KEITH FULLER Consultant, United Kingdom
ALESSANDRO MARTELLI ENEA, Italy

PRODUCTION


SILVIO LEVY Scientific Editor

See inside back cover or <http://pjm.math.berkeley.edu/siaps/> for submission guidelines.

SIAPS (ISSN 2150–7902) is published in electronic form only. The subscription price for 2011 is US \$150/year. Subscriptions, requests for back issues, and changes of address should be sent to Mathematical Sciences Publishers, Department of Mathematics, University of California, Berkeley, CA 94720–3840.

SIAPS peer-review and production is managed by EditFlow™ from Mathematical Sciences Publishers.

PUBLISHED BY

 **mathematical sciences publishers**
<http://msp.org/>

A NON-PROFIT CORPORATION

Typeset in L^AT_EX

©Copyright 2011 by Mathematical Sciences Publishers

A TRIBUTE TO DR. WILLIAM H. (BILL) ROBINSON

The scientific community involved with seismic isolation was saddened to learn on the passing of Bill Robinson on August 17, 2011. Dr. Robinson, Fellow of the New Zealand Royal Society and founder of Robinson Seismic Inc., was a scientist and seismic engineer and inventor of the lead-rubber bearing (LRB) seismic isolation technology.

We would like to make a special tribute to Dr. Robinson by republishing one of his fundamental papers, introduced by a foreword that was prepared by the author himself when SIAPS was launched in 2010.

Bill, you will be sadly missed.

— The Editorial Board

FOREWORD

to the [reprinting](#) of “Lead-rubber hysteretic bearings suitable. . .”

BILL ROBINSON

Once upon a time — well, actually, April 1970 — in a New Zealand tea room, Bill met Ivan. . . and that was where this particular adventure in seismic isolation began.

Bill — Dr. Bill Robinson — and Ivan — Dr. Ivan Skinner — were both members of New Zealand’s Department of Scientific and Industrial Research, and the tea room in question was part of its Physics and Engineering Laboratory (PEL) on the Gracefield Campus near Wellington. Ivan, head of Engineering Seismology, had briefly returned to New Zealand from a sabbatical in Japan, and told Bill of how he proposed to use steel dampers in the seismic isolation of the new design office being planned for New Zealand’s Ministry of Works (MOW), known as the William Clayton Building.

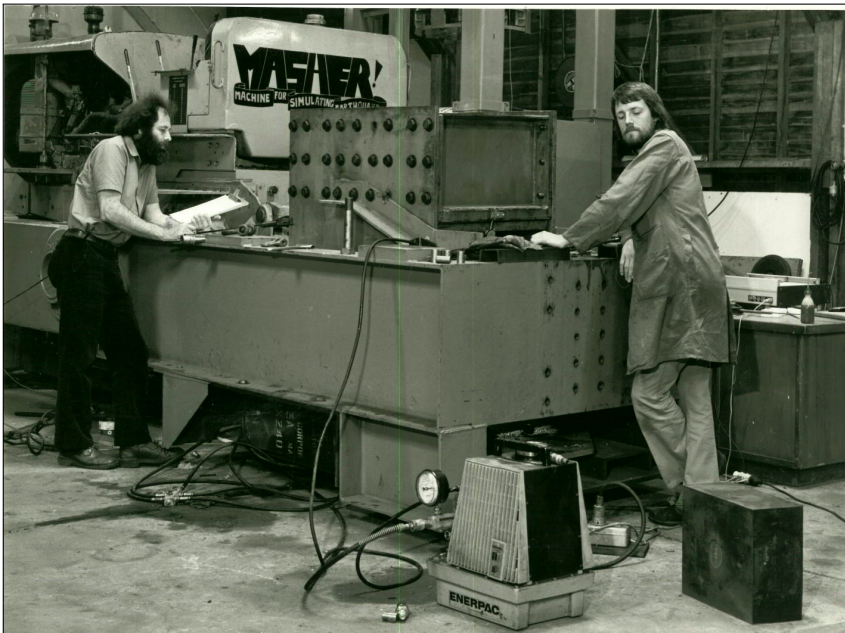


William Clayton Building under construction, 1981.

Bill thought he could find a better material for damping than steel, so he went back to his office and spent the next two hours looking carefully for an element that had a relatively low melting point ($\sim 300^{\circ}\text{C}$), was face-center cubic (fcc), was readily available at a high purity (impurities < 100 ppm)—and all at a reasonable price. The only element that met these demands was lead. Its relatively low melting point ensured that any plastic deformation would be healed at room temperature by the interrelated processes of recovery, recrystallisation and grain growth, while its fcc meant there would always be a slip system available to accommodate any deformation and its high purity would see to it that the plastic deformation could be maintained and results would be consistent.

The next problem was how to deform lead so that a relatively large damping force of 1 to 100 tonnes could be produced. The solution was a lead extrusion damper (LED). This thinking culminated in twenty-four 25 tonne LEDs (± 400 mm) being manufactured and tested by PEL to provide the damping for seismically isolating the Wellington Central Police Station. This 10-storey tower block is supported on long piles in caissons founded 15m below ground in weathered greywacke rock. The near surface-soil layer consisted of marine sediment and fill of dubious quality.

The LED, however, was not an elegant solution for damping the MOW's William Clayton Building, so instead Bill started trying to make a lead shear damper. But, no matter what the shape, they always failed after one quarter of a cycle. Obviously they needed to be supported in some way. As recorded in Bill's lab book, the solution, which occurred to him at home on 2 April 1975, was to place a lead plug through the layers of steel and rubber. It was not until April 1977, though, that his team was able to obtain two cemented laminated rubber bearings from the Engineering Seismology Section, have the workshop drill a 56mm diameter hole in one, press a lead plug in the hole, and test both in an Instron testing machine.



Bill and his technician Alan Tucker operating the MASHER.



Bill and his colleague, Dr. Michael Staines, on the sea ice at Tent Island, McMurdo Sound, Antarctica, near Scott Base. The final version of the paper reprinted on the next few pages was written while Bill was a research fellow at Scott Polar Research Institute, Cambridge, England learning about sea ice.

The results were so promising that Bill immediately contacted the MOW engineers working on the design of the William Clayton building and they decided to sell PEL an old D8 Caterpillar tractor to use as the basis of a test machine. PEL sold the tractor’s blade for more than the cost of the tractor itself and the engineering design team, led by Cam Smart, designed a rig powered by the > 100 KW diesel engine, capable of providing a vertical load of 300 tonnes and a displacement of up to 91 mm. Bill then tested a series of bearings of progressively increasing diameter, until at a lead diameter of 170 mm, after two cycles the gearbox failed! This result was viewed by all as a success and enabled the project to proceed. Today thousands of buildings and bridges worldwide use the lead-rubber bearing.

References

- [Kelly et al. 2011] T. E. Kelly, R. I. Skinner, and W. H. Robinson, *Seismic isolation for designers and structural engineers*, Robinson Seismic Ltd., Petone, New Zealand, 2011.
- [Skinner et al. 2003] R. I. Skinner, W. H. Robinson, and G. H. McVerry, *An introduction to seismic isolation*, Wiley, New York, 2003.

BILL ROBINSON: *Robinson Seismic Limited, PO Box 33093, Petone 5046, New Zealand*
www.rslnz.com

LEAD-RUBBER HYSTERETIC BEARINGS SUITABLE FOR PROTECTING STRUCTURES DURING EARTHQUAKES

WILLIAM H. ROBINSON

Reprinted with permission from *Earthquake Engineering and Structural Dynamics* **10**:4, 593–604 (1982)

Lead-rubber hysteretic bearings provide in a single unit the combined features of vertical load support, horizontal flexibility and energy absorbing capacity required for the base isolation of structures from earthquake attack. The lead-rubber hysteretic bearing is a laminated elastomeric bearing of the type used in bridge structures, with a lead plug down its centre.

Since the invention of the lead-rubber bearing, a total of eleven bearings up to a diameter of 650 mm, with lead plugs ranging from 50 to 170 mm in diameter, have been tested under various conditions, including vertical loads to 3.15 MN, strokes to ± 110 mm, rates from 1 mm/h to 100 mm/s, and temperatures of -35°C to $+45^{\circ}\text{C}$. In all of these tests, the lead-rubber bearings behaved satisfactorily and the hysteresis loops could be described reasonably well by assuming that the lead behaved as an elastic-plastic solid with a yield stress in shear of 10.5 MPa. The bearings showed little rate dependence at ~ 100 mm/s, though at creep rates of ~ 1 mm/h the force due to the lead dropped to 30 per cent of that at typical earthquake frequencies. The effect of many small displacements has been tested with 11 000 cycles at ± 3 mm. A total of 92 lead-rubber bearings have been used in New Zealand to base isolate one building and three bridges. They have yet to be used overseas.

This paper describes the tests on the lead-rubber bearings, the results and a design procedure for selecting the size of the lead plug.

Introduction

Since 1970 a number of papers have been written describing how base-isolated structures can be protected from damage caused by earthquake attack [Skinner et al. 1975a; Skinner and McVerry 1975]. These base-isolated structures normally sit on PTFE sliding bearings or rubber elastomeric bearings. The main effect of the base isolation is to decouple the structure from the ground and increase the resonant period of the structure plus bearings to a value outside the range of periods containing the principal earthquake energies. More complete base isolation studies have shown that further reduction in forces and moments transmitted to the structure occurs if some Coulomb damping, usually ~ 5 per cent of the weight, is placed in parallel with the base isolation [Lee and Medland 1981; Meggett 1978]. Another advantage of the addition of damping is that it may cause a reduction of displacement of the structure by a factor of ~ 2 to a more manageable size of $\sim \pm 100$ mm.

During the seventies a range of hysteretic dampers was invented and developed at the Physics and Engineering Laboratory to provide the required damping for base isolation [Robinson and Greenbank 1975; 1976; Skinner et al. 1975b; 1980]. In New Zealand the plasticity of steel and its good fatigue

Keywords: history, lead-rubber bearings.

properties during cyclic plastic strain have been used in a torsion beam damper installed in the NZ Railways Rangitikei Bridge, in a tapered cantilever damper used in a Dunedin motorway bridge, and more recently in a flexural beam damper designed for Cromwell Bridge. The plastic deformation of lead for hysteretic dampers began with the invention of the lead extrusion damper, a device which behaves as a rigid-plastic solid. Twelve extrusion dampers designed to operate at 150 kN and with a maximum stroke of ± 250 mm have been manufactured by Auckland Nuclear Accessories Ltd and installed by Ministry of Works and Development (MWD) in two overpass bridges in Wellington, New Zealand. The sloping bridge decks are supported vertically by glide bearings and the extrusion dampers connect the decks to the fixed abutments; they have a high stiffness and low creep rate which minimizes any movement of the bridge due to the braking of traffic (~ 1 or 2 mm/yr). [Skinner et al. 1980] is a summary and discussion of the work on hysteretic dampers.

The lead-rubber hysteretic bearing is a more recent innovation [Robinson 1975; Robinson and Tucker 1983; 1977] and consists of an elastomeric bearing with a lead plug down its centre (Figure 1). It is possibly the cheapest solution to the problems of base isolation in that the one unit supports the base-isolated structure, provides an elastic restoring force and also, by the selection of the appropriate size of lead plug, produces the required amount of damping.

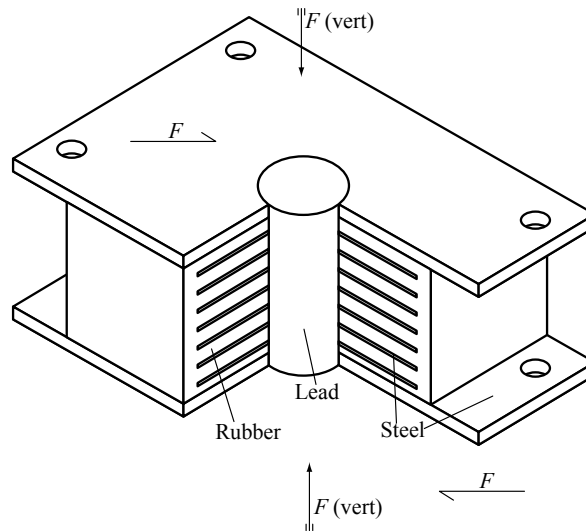


Figure 1. Lead-rubber hysteretic bearing.

In this paper the properties of the lead-rubber hysteretic bearing are described together with its behaviour under various loading conditions: a design procedure is discussed before describing a number of applications which include the building and three bridges which already have been base isolated by lead-rubber bearings.

Description of the lead-rubber hysteretic bearings

Before describing the hysteretic bearing in detail it is worthwhile considering the reasons for choosing lead as the material for the insert in the bearings. First, in shear the lead yields at the relatively low stress of ~ 10 MPa and behaves approximately as an elastic-plastic solid. Thus a reasonable size insert of

~100 mm in diameter is required to produce the necessary plastic damping forces of ~100 kN. Second, at room temperature when lead is plastically deformed it is being ‘hot worked’ and the mechanical properties of the lead are being continuously restored by the interrelated processes of recovery, recrystallization and grain growth which are occurring simultaneously [Birchenell 1959; Wulff et al. 1956]. In fact plastically deforming lead at 20°C is equivalent to plastically deforming iron or steel at a temperature of greater than 450°C. Therefore, lead has good fatigue properties during cycling at plastic strains [Robinson and Greenbank 1976]. Third, because of its use in batteries, lead is readily available at the high purity of 99.9 per cent required for its mechanical properties to be predictable.

The normal elastomeric bearing consists of alternate layers of rubber sheets cemented or vulcanized to steel plates. The cemented elastomeric bearing and the vulcanized version have been used for over two decades in bridge structures. The elastomeric bearing supports the weight of the structure, provides an elastic restoring force and in the case of bridges allows the bridge to expand thermally without causing excessive forces in the bridge structure.

The elastomeric bearing is readily converted into a lead-rubber hysteretic bearing by placing a lead plug down its centre (Figure 1). The hole for the lead plug can be machined through the bearing after manufacture or, if numbers permit, the hole can be made in the steel plates and rubber sheets before they are joined together. The lead is then cast directly into the hole or machined into a plug before being pressed into the hole. For both methods of placing the lead it is imperative that the lead plug is a tight fit in the hole and that it locks with the steel plates and extrudes a little into the layers of rubber. To ensure this occurs it is recommended that the lead plug volume be 1 per cent greater than the hole volume enabling the lead plug to be firmly pressed into the hole. Thus, when the elastomeric bearing is deformed horizontally, the lead insert is forced by the interlocking steel plates to deform over its whole volume in pure shear.

Altogether six different elastomeric bearings were tested with lead inserts (see Table 1). The first, to see if the concept would work, was a small cemented bearing and it was tried with lead plugs of two diameters. The second was a large vulcanized bearing which was progressively fitted with lead inserts of five different diameters, to determine the effect of the diameter of the lead insert on the hysteresis

Dimensions (mm)	d (mm)	k_r (kN/mm)	k_v (kN/mm)	h/d	$x(\max)$ (mm)	$\gamma(\max)$	$F(\text{vert})$ (MN)	Comments
356 × 356 × 140	56, 100	0.5		2.5, 1.4	±68	0.49	0.45	Cemented
650 diam × 197	50, 70, 100, 140, 170	1.75	600	4 to 1.15	±91	0.46	1, 2, 3	Vulcanized
600 × 600 × 207	105	1.70	600	2.0	±110	0.53	1, 2, 3	Vulcanized Two bearings for Wm Clayton Building
280 × 230 × 127	75	0.55	205	1.7	±93	0.73	0.16 to 0.21	Vulcanized One bearing for Toe Toe Bridge
406 × 356 × 177	75	0.50	190	2.4	±83	0.47	0.35	Vulcanized One bearing for Waiotukupuna Bridge

Table 1. Summary of lead-rubber bearings tested.

loop and to demonstrate the feasibility of using lead inserts in large elastomeric bearings. The next two lead-rubber bearings were selected from 82 manufactured for the Wm Clayton Building, Wellington, and the final two, one each from the Toe Toe and Waitotukupuna Bridges.

Properties of the lead-rubber hysteretic bearings

(i) *Test equipment.* To determine the force-displacement hysteresis loops of the various bearings at speeds of 1 mm/h to 100 mm/s three combinations of equipment were used. The first lead-rubber bearing tested was mounted back to back with a bearing not containing a lead plug and the plate between the bearing was moved while a vertical load of up to 450 kN was applied to both bearings via a hydraulic jack (Figure 2). For high speed tests this movement was produced via a linkage to a cam on a modified Caterpillar D8. The creep behaviour was determined by mounting the bearing holder in a 250 kN Instron testing machine capable of operating at 10^{-3} mm/min to 200 mm/min.

After the first bearing had been tested a more rigid bearing holder capable of high vertical forces (3.15 MN) was constructed for the dynamic tests based on the requirements of the bearings for the Wm Clayton Building. The lead-rubber bearings were mounted horizontally, one at a time, in this rig. Underneath the rubber bearing was a horizontally located pressure plate which transmitted the vertical force from four hydraulic jacks to the bearing. On top of the bearing was a moving plate attached via a linkage to the drive of the Caterpillar D8. The upper face of the moving plate was greased and rubbed against fifty-two $20 \times 20 \times 2$ mm squares of PTFE bonded to a steel reaction plate. In the design the



Figure 2. Lead-rubber bearing in 250 kN Instron.

friction force on the lubricated PTFE was estimated to be 1 per cent of the normal reaction with a design vertical pressure up to 30 MPa [Tyler 1977]. The rig was designed for a maximum power of 100 kW, maximum vertical force of 4 MN, maximum horizontal force of 500 kN, a maximum stroke of 250 mm (± 125 mm) and maximum frequency of 0.9 Hz, though in fact for these tests at high loads the maximum power was approximately 70 kW.

(ii) **Hysteresis loops.** In order to derive the force-displacement hysteresis loops from the experimental results it was necessary to subtract the shear force due to the sliding PTFE. This shear force was determined by testing dynamically the 650 mm diameter elastomeric bearing before it was fitted with a lead plug. For this rubber bearing there occurred on reversal of stroke a sudden change in force which was dependent on the vertical load. The sudden change in force on reversal of the direction of shear velocity was taken to be twice the shear force due to the PTFE and was found to be in good agreement with previous work [Tyler 1977].

The force-displacement hysteresis loop of an elastomeric bearing without a lead plug is shown as the dotted curve in Figure 3. This loop, which is for the bearing 650 mm in diameter, is mainly elastic with a shear stiffness, $k_r = 1.75$ kN/mm, and a small amount of hysteresis. Also in the figure is the result for the same bearing containing a lead insert with a diameter of 170 mm. The dashed lines are at the slope of 1.75 kN/mm and are a good approximation to the post yield stiffness, k_{ab} , between the points 'a' and 'b' where 'a' and 'b' are at zero and the maximum displacement respectively. In this case the lead is behaving as a plastic solid which adds ~ 235 kN to the elastic force required to shear the bearing. However, this is one of the better results in that for all of the dynamic tests the post yields stiffness varied between $k_r \pm 40$ per cent with most results between $k_r \pm 25$ per cent. For example, for the Waiotukupuna bearing the post yield stiffness was $k_{ab} = 1.25k_r$ (Figure 4), while for the Wm Clayton bearing $k_{ab} = 0.8k_r$ (Figure 5).

Another factor of interest is the initial elastic part of the force-displacement curve for small forces. This shear stiffness is found to lie between 9 and $15k_r$, with most of the results near $10k_r$. It must be

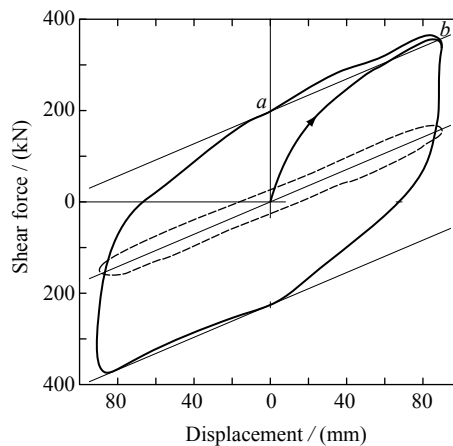


Figure 3. Force-displacement hysteresis loops for 650 mm diameter bearing ($F(\text{vert}) = 3.15$ MN, 0.9 Hz, stroke ± 91 mm). Dotted line is for the bearing without a lead plug while the full line is for a lead plug of 170 mm diameter. Slope of dashed lines is k_r .

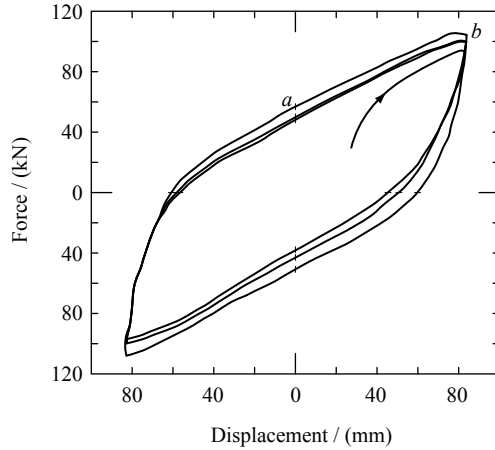


Figure 4. Force-displacement hysteresis loops for Waiotukupuna bearing with a vertical force of 350 kN, stroke of ± 85 mm and 0.9 Hz.

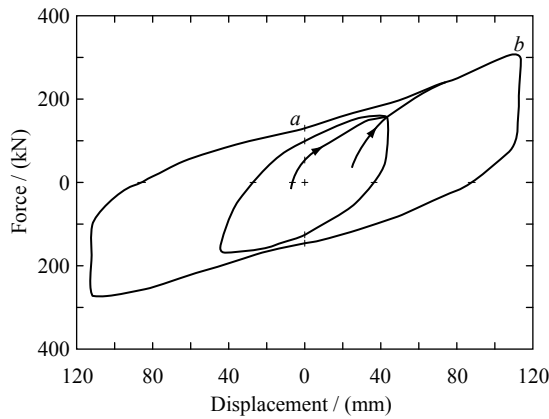


Figure 5. Force-displacement hysteresis loops for the Wm Clayton Building bearing at ± 45 and ± 110 mm with a vertical force of 3.15 MN at 0.9 Hz.

emphasized that the accuracy of these results is poor in that to obtain them it was necessary to subtract the force due to the PTFE bearings from the measured force and at small displacements these forces are comparable.

Thus a reasonable description of the hysteresis loop is a bilinear solid with an initial elastic stiffness $k_1 = 10k_r$ followed by a post yield stiffness $k_2 = k_r$.

(iii) Dependence on the diameter of the lead insert. The dependence of the hysteresis loop on the diameter of the lead insert was investigated by fitting the bearing 650 mm in diameter with a series of inserts from 50 to 170 mm in diameter (Table 1). As expected the important parameter is the cross sectional area of the lead, $A(\text{Pb})$. The variation with $A(\text{Pb})$ of the force at 'a', $F(a)$, and the maximum force $F(b)$ is shown in Figures 6 and 7. In the case of $F(b)$ it is more useful to plot $F(b) - F(r)$, where $F(r)$ is the force due to the rubber calculated from the bearing shear stiffness (k_r). Also included in these two

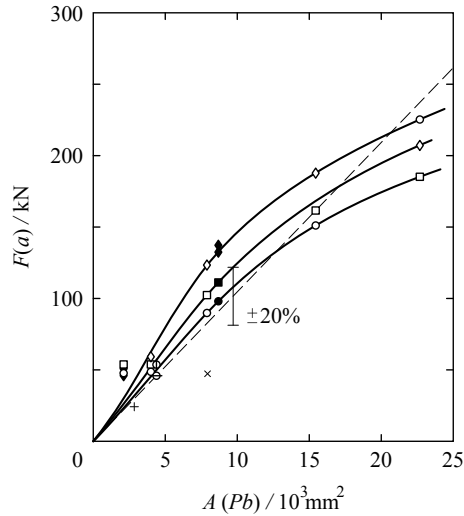


Figure 6. Dependence of force $F(a)$ on cross section area of lead insert. Vertical force \circ 1.05 MN, \square 2.10 MN, \diamond 3.15 MN, open points 650 mm diameter bearing, filled points Wm Clayton Building bearing. $+$ and \times 356 mm square bearing, Φ Waiotukupuna bearing and \oslash Toe Toe bearing. Dashed line is for $\sigma(Pb) = 10.5$ MPa.

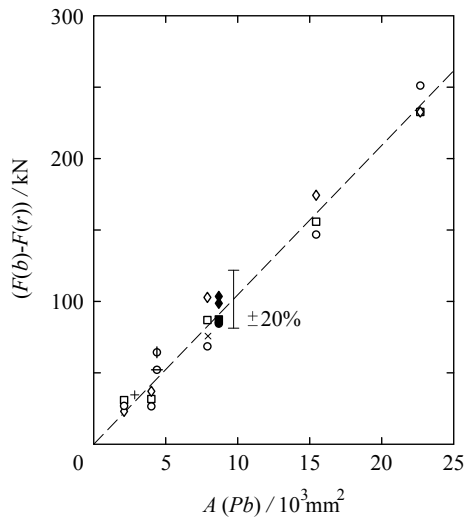


Figure 7. Variation of force $(F(b)-F(r))$ with cross section area of lead. Vertical force \circ 1.05 MN, \square 2.10 MN, \diamond 3.15 MN, open points 650 mm diameter bearing, filled points Wm Clayton Building bearing. $+$ and \times 356 mm square bearing, Φ Waiotukupuna bearing and \oslash Toe Toe bearing. Dashed line is for $\sigma(Pb) = 10.5$ MPa.

figures are the results for all the dynamic tests conducted on the various lead rubber bearings for a shear strain, $\gamma = x(\max)/h$, of ~ 0.5 , where $x(\max)$ is the maximum displacement and h is the total height of the lead in the bearing.

Except for the Waitotukupuna results all the data in Figure 7 lie within ± 20 per cent of a straight line with a slope of 10.5 MPa. Therefore, to a good approximation

$$F(b) = \sigma(\text{Pb})A(\text{Pb}) + k_r x(\text{max}), \quad (1)$$

where $\sigma(\text{Pb}) = 10.5$ MPa, and $A(\text{Pb})$ is the cross sectional area of the lead insert.

The results for the dependence of $F(a)$ on $A(\text{Pb})$ are not so simple with the data following a curve rather than a straight line (Figure 6). However, if $\sigma(a)$, where

$$\sigma(a) = F(a)/A(\text{Pb}) \quad (2)$$

is plotted against the height to diameter ratio (h/d) of the lead insert, then $\sigma(a)$ is found to increase gradually with h/d and is also dependent on the vertical compressive stress applied to the bearing (Figure 8).

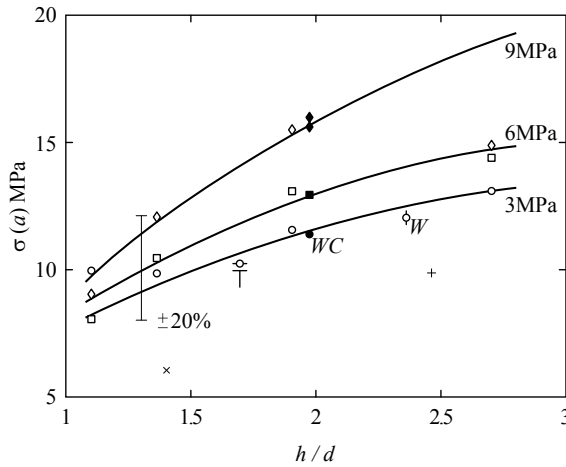


Figure 8. Dependence of lead yield stress, $\sigma(a)$, on the ratio of height to diameter of the lead for vertical stresses of 3, 6 and 9 MPa.

(iv) *Creep.* For a number of applications it is necessary to know the behaviour of the lead-rubber bearing under creep conditions. For example, if a bridge deck is mounted on the bearings then during the normal 24 hour cycle of temperature the bearings will have to accommodate $\sim \pm 3$ mm without producing large forces. To determine the effect of creep rates of ~ 1 mm/h the second lead-rubber bearing made, that is $356 \times 356 \times 140$ mm with a 100 mm lead plug, was mounted in the back to back reaction frame in the Instron (Figure 2). The first result was obtained at 6 mm/h with the force due to the lead alone reaching a maximum after 2.5 h before decreasing slowly. After 6 h the displacement was held constant and the force due to the lead decreased to one half in about one hour and continued to fall with time giving a relaxation time of 1 to 2 h. Another creep test was carried out at 1 mm/h for six hours when the direction was reversed giving the hysteresis shown in Figure 9. For completeness the force, $F(r)$, due to the rubber is included with its ± 20 per cent error bar. The shear stress in the lead plug reached a maximum of 3.2 MPa, which is ~ 30 per cent of the stress of 10.5 MPa for the dynamic tests.

Because of the large errors caused by $F(r)$ it was not possible to determine accurately the rate dependence of the lead in the lead-rubber bearing. To overcome this problem three lead hysteretic dampers,

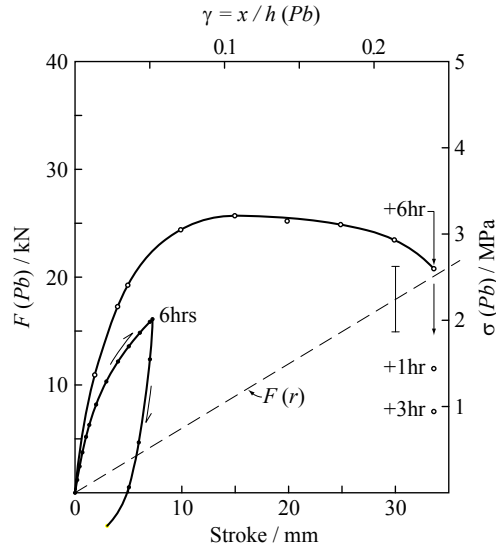


Figure 9. Force due to lead during creep of 356 mm square bearing with 100 mm diameter lead plug and vertical force of 400 kN. Open points 6 mm/h, filled 1 mm/h and dashed line is $F(r)$.

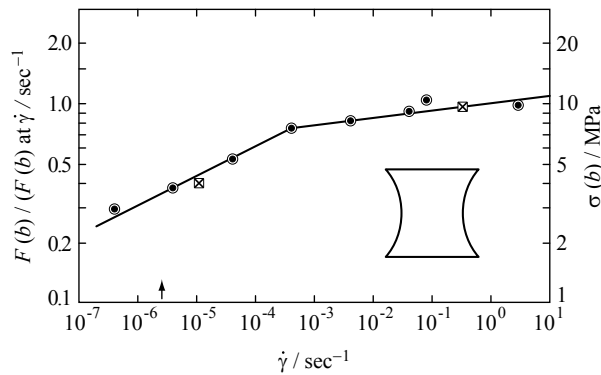


Figure 10. Creep dependence of lead in shear. Lead shear damper, 356 mm square bearing with 100 mm lead insert.

which were designed to operate in shear without a rubber bearing [Robinson 1975; Tucker and Robinson 1976] were tested at various strain rates. These dampers consisted of parabolic lead cylinders with their ends soldered to two brass plates (Figure 10). They were parabolically shaped to minimize the effect of the bending moments which occur away from the neutral axis of the lead during the application of simple shear; in fact to a first approximation the shear stress near the parabolic surface of the lead remained constant. The shear dampers were made with their height equal to waist diameter and had diameters of 24, 42 and 94 mm and nominal $\dot{\gamma} = 1 \text{ s}^{-1}$ forces of 8, 24 and 120 kN respectively. The rate dependence of these dampers, with their shear stress normalized to that at $\dot{\gamma} = 1 \text{ s}^{-1}$, is shown in Figure 10 together with the values obtained for the second lead rubber bearing at 10^{-5} and $3 \times 10^{-1} \text{ s}^{-1}$. These results

follow

$$\sigma(\text{Pb}) = a\dot{\gamma}^b \quad (3)$$

where below $\dot{\gamma} = 3 \times 10^{-4} \text{ s}^{-1}$, $b = 0.15$ and above, $b = 0.035$. For the lead extrusion damper [Robinson and Greenbank 1976] it was found that for the two regions $b = 0.12$ and 0.03 , values within the experimental error of the present work. For slow creep other authors conclude that $b = 0.13$ [Pearson 1944; Pugh 1970].

These results indicate that the lead-rubber bearing has little rate dependence at strain rates of $3 \times 10^{-4} \text{ s}^{-1}$ to 10 s^{-1} , which includes typical earthquake rates of 10^{-1} to 1 s^{-1} , and in fact in this region an increase of rate by a factor of ten causes an increase in force of only 8 per cent. Below strain rates of $4 \times 10^{-4} \text{ s}^{-1}$, the dependence of the shear stress on creep rate is greater, with a 40 per cent change in force for each decade change in rate. However, this means that at creep displacements of $\sim 1 \text{ mm/h}$ for a typical bearing 100 mm high, that is $\dot{\gamma} \sim 3 \times 10^{-6} \text{ s}^{-1}$, the shear stress has dropped to 35 per cent of its value at typical earthquake rates ($\dot{\gamma} \sim 1 \text{ s}^{-1}$).

(v) *Fatigue and temperature.* The lead-rubber bearing can be expected to survive a large number of earthquakes, each of which causes 3 to 5 excursions of $\sim 100 \text{ mm}$. For example, the results for a series of dynamic tests on the 650 mm diameter bearing with a 140 mm diameter lead plug are shown in Figure 11. $F(a)$ and $F(b)$ decreased by 10 and 25 per cent over the first five cycles but recovered some of this decrease in the five minute breaks between tests. An interval of 12 days between the last two tests did not give a greater recovery than that obtained in 5 minutes. The effect of the 24 cycles is shown more clearly in Figure 12 where the two hysteresis loops are the first and twenty-fourth. The area of the twenty-fourth loop is 80 per cent of the first, indicating that the bearing has retained most of its damping capacity over these five simulated earthquakes.

As a further check on the fatigue performance, the 356 mm bearing was dynamically tested at a shear strain of 0.5 for a total of 215 cycles in a two-day period. This bearing was also subject to 11 000 cycles

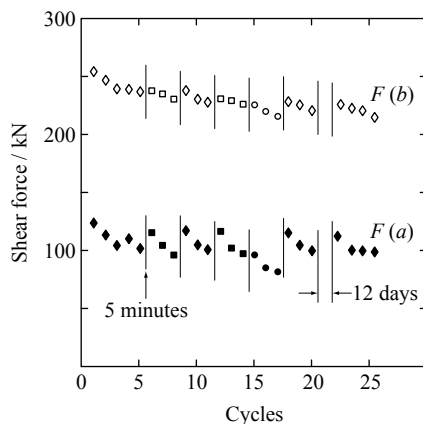


Figure 11. Variation of $F(a)$ (filled points) and $F(b)$ (open points) with number of cycles for 650 mm diameter bearing, 140 mm diameter lead insert, $\pm 91 \text{ mm}$ stroke and 0.9 Hz . \circ 1.05 MN, \square 2.10 MN, \diamond 3.15 MN.

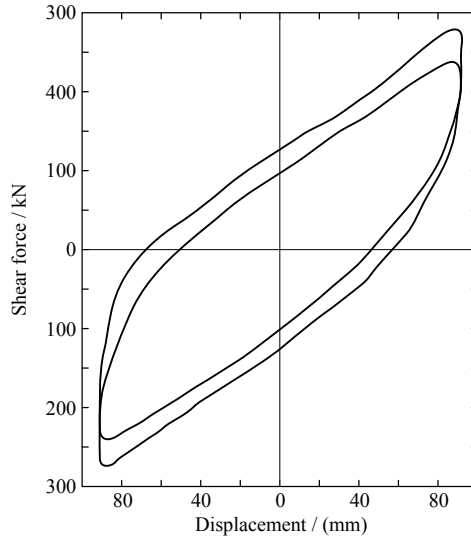


Figure 12. First (outer) and last (inner) hysteresis loops from Figure 11.

at ± 3 mm (0.9 Hz) to demonstrate that it could withstand the daily cycles of thermal expansion which occur in a bridge deck over a period of 30 years.

The 356 mm bearing was also studied with dynamic tests ($\dot{\gamma} \sim 0.5, 0.9$ Hz) at temperatures of -35 , -15 and $+45^\circ\text{C}$ to ensure its performance in extreme temperature environments. The ratio of the force $F(b)$ to that at 18°C for the first cycle was 1.4, 1.2 and 0.9 at -35 , -15 and $+45^\circ\text{C}$ respectively.

After both the fatigue and the temperature tests the lead-rubber bearing operated satisfactorily at 18°C . A more complete report of these and other tests is contained in [Robinson 1981].

Discussion

For strain rates of $\sim 1 \text{ s}^{-1}$ the lead-rubber hysteretic bearing can be treated as a bilinear solid with an initial shear stiffness of $\sim 10k_r$, and a post yield shear stiffness of k_r . The yield of the lead insert can be readily determined from the yield stress of the lead in the bearing of 10.5 MPa. Thus the maximum shear force for a given displacement is the sum of the elastic force of the elastomeric bearing and the plastic force required to deform the lead. The actual post yield stiffness is likely to vary by up to ± 40 per cent from k_r but will most likely be within ± 25 per cent of this value. The initial elastic stiffness has only been estimated from the experimental results and may in fact be in the range of $5k_r$, to $15k_r$. The prediction for the maximum force, $F(b)$, is more accurate and has instead an uncertainty of ± 20 per cent which is the same as expected for the uncertainty in the shear stiffness of manufactured elastomeric bearings. The actual area of the hysteresis loop formed by this bilinear model is approximately 20 per cent greater than the area of the measured hysteresis loop.

For most applications the ratio h/d should be greater than 1.5 but a value > 2 is more appropriate for light vertical loads. If the vertical load is light and h/d is close to one then the lead will not be sheared by the steel plates in the elastomeric bearing. Instead, at the edge of the hole, the steel plates will bend and the lead will deform into a ball which will provide very little damping. The manufactured bearings which were tested had h/d ratios of 1.7 and 2.4 (Table 1).



Figure 13. Wm Clayton Building as at March 1981

So far the lead-rubber hysteretic bearing has been used to base isolate three bridges and one building in New Zealand. The construction of the building was started in 1978 by the NZ Ministry of Works and is now nearing completion (Figure 13). This 97×40 m four-storey building with a reinforced concrete structure sits on eighty lead-rubber bearings manufactured by Empire Rubber Mills, Christchurch, N.Z. Each bearing carries a vertical load of 1 to 2 MN and is capable of taking a horizontal displacement of ± 200 mm. The bearing size and lead diameter were chosen after careful dynamic analysis using 1.5 times the El Centro 1940 earthquake (NS component) and the artificial A1 earthquake. [Meggett 1978] discusses this design in detail and concludes that for these two earthquakes shear displacements of 100 to 150 mm need to be accommodated while acceleration, inter-storey drifts and maximum base shear forces are approximately halved for the base-isolated system. He concludes that reasonable values for the shear stiffness of the elastomeric bearing and lead yield stress are

$$k_r = (1 \text{ to } 2)W \text{ m}^{-1} \quad (4)$$

and

$$F(\text{Pb}) = (0.05 \text{ to } 0.10)W \quad (5)$$

while in fact the bearings were measured with $k_r = 1.1W \text{ m}^{-1}$ and $F(b) = 0.07W$. In a further dynamic study of base-isolated multi-storey buildings [Lee and Medland 1981] concluded that for a bilinear hysteretic damper the effective period of the isolated structure is governed by the post yield stiffness of the isolation system and they give similar results to those obtained by Meggett for maximum displacement,

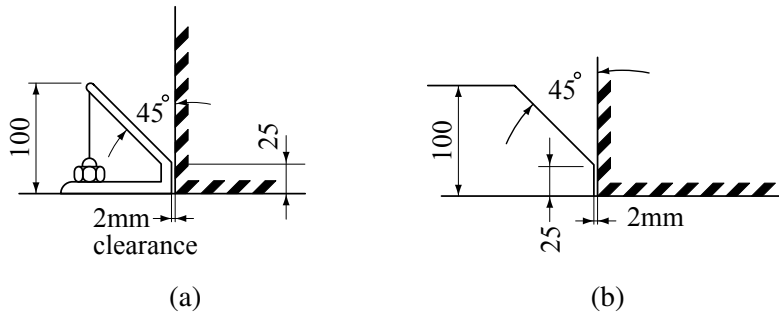


Figure 14. Possible details of the lead-rubber bearing at column footing. (a) On flat foundation and (b) in recess in foundation.

post yield stiffness and yield force. [Lee 1980] also studied the torsion reduction which occurs in asymmetric buildings which have been baseisolated and finds great reductions to twisting movements when the isolation system has properties similar to those determined by Meggett.

For base-isolated bridges, after careful dynamic analysis [Blakeley et al. 1980] give a range of parameters close to those summarized by Meggett and in fact chose for the Toe Toe Bridge an identical shear stiffness ($k_r = 1.1 W m^{-1}$) and a fractionally higher yield force ($F(Pb) = 0.08W$) to those for the Wm Clayton Building.

The lead-rubber bearings base isolating three bridges and one building which have been built are bolted to the structures and to the foundations. The disadvantage in this approach is that large vertical accelerations may cause damage to the bearing by the application of large tensile forces. Possibly a better method is to place the bearing in a recess in the structure and bolt the bearing to the foundation, or *vice versa* (Figure 14). With this arrangement, when there is uplift relative movements of 50 mm can be readily accommodated while even after larger vertical movements of up to 100 mm the bearing will be guided back into its place by the chamfered edges. This layout would satisfy the contention of some engineers that allowing uplift of columns of a building, particularly at corners, would make for relief of earthquake loadings.

Conclusions

- (i) The lead-rubber hysteretic bearing provides an economic solution to the problem of base isolating structures in that one unit provides the three functions of vertical support and horizontal flexibility via the rubber, and hysteretic damping by the plastic deformation of the lead.
- (ii) The lead-rubber hysteretic bearing behaves like a bilinear solid with an initial elastic shear stiffness, $k_1 \sim 10k_r$, a post elastic shear stiffness, $k_2 = k_r$, with the yield force being determined by the shear stress at which the lead in the bearing yields. This shear stress is found to be 10.5 MPa. The area of the measured hysteresis loop is found to be ~ 80 per cent of the loop defined by the bilinear solid model.
- (iii) A total of eleven lead-rubber bearings has been tested at strokes as high as ± 110 mm for three to 75 cycles at ~ 0.9 Hz. These bearings performed well under what is equivalent to strong earthquakes

attacking a base-isolated structure. Other more extreme dynamic tests include cycling at -35 and $+45^{\circ}\text{C}$ and 11 000 cycles at ± 3 mm.

- (iv) The results at shear strain rates of 3×10^{-7} to 3 s^{-1} show that at rates expected during an earthquake ($\sim 1 \text{ s}^{-1}$) the lead-rubber bearing has very little rate dependence while at rates expected during thermal expansion ($\sim 3 \times 10^{-6} \text{ s}^{-1}$) the shear stress is more strongly rate dependent.
- (v) The lead-rubber hysteretic bearing has been used to base isolate three bridges and one building in New Zealand and possibly is the most economic base isolation system available at present.

Acknowledgements

The 650 mm diameter elastomeric bearings were supplied by the New Zealand Ministry of Works and Development.

References

- [Birchenell 1959] C. E. Birchenell, *Physical metallurgy*, McGraw-Hill, London, 1959.
- [Blakeley et al. 1980] R. W. G. Blakeley, L. G. Cormack, and M. J. Stockwell, "Mechanical energy dissipation devices", *Bull. N.Z. Natl. Soc. Earthquake Eng.* **13** (1980), 264–268.
- [Lee 1980] D. M. Lee, "Base isolation for torsion reduction in asymmetric structures under earthquake loading", *Earthquake Eng. Struct. Dyn.* **8**:4 (1980), 349–359.
- [Lee and Medland 1981] D. M. Lee and I. C. Medland, "Base isolation systems for earthquake protection of multi-storey shear structures", *Earthquake Eng. Struct. Dyn.* **7** (1981), 555–568.
- [Meggett 1978] L. M. Meggett, "Analysis and design of a base-isolated reinforced concrete frame building", *Bull. N.Z. Natl. Soc. Earthquake Eng.* **11** (1978), 245–254.
- [Pearson 1944] C. E. Pearson, *The extrusion of metals*, Wiley, New York, 1944.
- [Pugh 1970] H. L. D. Pugh, "Hydrostatic extrusion", in *Mechanical behaviour of materials under pressure*, edited by H. L. D. Pugh, Applied Science, London, 1970.
- [Robinson 1975] W. H. Robinson, New Zealand patent 178949, 14 October 1975. Also U.S. patent 4117637 ("Cyclic shear energy absorber") and Japan patent 49609/77.
- [Robinson 1981] W. H. Robinson, "Lead rubber hysteretic bearings suitable for protecting structures during earthquakes", PEL Report 715, 1981.
- [Robinson and Greenbank 1975] W. H. Robinson and L. R. Greenbank, "Properties of an extrusion energy absorber", *Bull. N.Z. Natl. Soc. Earthquake Eng.* **8** (1975), 287–291.
- [Robinson and Greenbank 1976] W. H. Robinson and L. R. Greenbank, "An extrusion energy absorber suitable for the protection of structures during an earthquake", *Earthquake Eng. Struct. Dyn.* **4**:3 (1976), 251–259.
- [Robinson and Tucker 1977] W. H. Robinson and A. G. Tucker, "A lead-rubber shear damper", *Bull. N.Z. Natl. Soc. Earthquake Eng.* **10** (1977), 151–153.
- [Robinson and Tucker 1983] W. H. Robinson and A. G. Tucker, "Test results for lead-rubber bearings for the William M. Clayton Building, Toe Toe Bridge and Waitokupuna Bridge", *Bull. N.Z. Natl. Soc. Earthquake Eng.* **14**:1 (1983), 21–33.
- [Skinner and McVerry 1975] R. I. Skinner and G. H. McVerry, "Base isolation for increased earthquake resistance of buildings", *Bull. N.Z. Natl. Soc. Earthquake Eng.* **8** (1975), 93–101.
- [Skinner et al. 1975a] R. I. Skinner, J. L. Beck, and G. N. Bycroft, "A practical system for isolating structures from earthquake attack", *Earthquake Eng. Struct. Dyn.* **3**:3 (1975), 297–309.
- [Skinner et al. 1975b] R. I. Skinner, J. M. Kelly, and A. J. Heine, "Hysteretic dampers for earthquake-resistant structures", *Earthquake Eng. Struct. Dyn.* **3** (1975), 287–296.

- [Skinner et al. 1980] R. I. Skinner, R. G. Tyler, A. J. Heine, and W. H. Robinson, “Hysteretic dampers for the protection of structures from earthquakes”, *Bull. N.Z. Natl. Soc. Earthquake Eng.* **13** (1980), 22–36.
- [Tucker and Robinson 1976] A. G. Tucker and W. H. Robinson, “Shear energy absorbers”, PEL Report 518, 1976.
- [Tyler 1977] R. G. Tyler, “Dynamic tests on PTFE sliding layers under earthquake conditions”, *Bull. N.Z. Natl. Soc. Earthquake Eng.* **10** (1977), 129–138.
- [Wulff et al. 1956] J. Wulff, J. F. Taylor, and A. J. Shayler, *Metallurgy for engineers*, Wiley, New York, 1956.

Received 22 May 1981. Revised 2 Nov 1981.

WILLIAM H. ROBINSON: *Physics and Engineering Laboratory, Department of Scientific and Industrial Research, Lower Hutt, New Zealand*

THE USE OF TESTS ON HIGH-SHAPE-FACTOR BEARINGS TO ESTIMATE THE BULK MODULUS OF NATURAL RUBBER

JAMES M. KELLY AND JIUN-WEI LAI

The bulk modulus of elastomeric materials such as natural rubber is an extremely difficult property to measure since the bulk modulus is several orders of magnitude larger than their shear modulus, so that the material will deform only in shear if at all possible. In most applications the deformation is assumed to be a constant volume one and the material is assumed to be incompressible, but there are situations where the compressibility of the material can play an important role and where it is necessary to have an accurate estimate of the bulk modulus. It will be shown in this paper that one way to determine the bulk modulus is to use the measured vertical stiffness of bearings used as seismic isolators to estimate its value. Seismic isolators are usually made with compounds, known as high damping rubbers, that are nonlinear and have large hysteresis, which can make interpretation of the measurements difficult; but in some cases the compounds used, for example linear natural rubber, have almost no hysteresis and are very linear in shear up to very large shear strains. In this paper, test results from a particular seismic isolation project were analyzed using the theory of bearing mechanics to provide an estimate of the bulk modulus for this particular compound and to show how, if tests on bearings with other compounds are available, to interpret the data for this purpose.

1. Introduction

The bulk modulus of elastomeric materials is an extremely difficult property to measure. Elastomers such as natural rubber have a bulk modulus that is several orders of magnitude larger than their shear modulus, so the material will deform in shear only if at all possible. In most applications the deformation can be assumed to be a constant volume one and the material be assumed to be incompressible. However, there are situations where the compressibility of the material can play an important role and where it is necessary to have a more accurate estimate of the bulk modulus. An example of such a case arises in the use of multilayer elastomeric bearings as support pads for bridges or as seismic or vibration isolators for buildings. When these components are designed, the rubber is usually assumed to be incompressible and there is a fairly simple analysis procedure to predict the vertical stiffness of the bearing or isolator. However, it is somewhat surprising that, for quite modest shape factors, the bulk compressibility of the rubber can have an important role; the design formula based on the incompressible model can seriously overpredict the vertical stiffness and the buckling load of a bearing.

Accordingly, it is essential to have an accurate estimate of the bulk modulus. A quick review of the data available on this property for natural rubber in particular reveals that an accurate estimate is difficult to find. For example, the widely used handbook [Lindley 1992] provides a table of bulk modulus values based on the IRHD hardness (International Rubber Hardness Degree) that range from 1000 to 1330 MPa

Keywords: rubber, elastomeric bearings, bulk modulus, base isolation, shape factor.

as the hardness varies from 30 to 75 IRHD. On the other hand, the reference [Fuller et al. 1988] gives values in the range from 2000 to 3500 MPa.

One way to determine the bulk modulus in a somewhat indirect way is to use the measured vertical stiffness of isolators to estimate its value. Seismic isolators are usually made with compounds known as high damping rubbers (HDR) that are nonlinear and have large hysteresis which can make interpretation of the measurements difficult but in some cases the compounds known as linear natural rubber (LNR) have almost no hysteresis and are very linear in shear up to very large shear strains.

A case in point is an isolation project in South Korea [EESK 2007] where a group of four fourteen-story residential buildings are built on isolation systems that combine lead plug rubber bearings (LRB) with low damping rubber bearings. In this project, there are two types of these LNR bearings designated as RB2 and RB3, and there are twenty bearings of each type. Each bearing of both types was tested in both horizontal shear and vertical compression before installation and it was found that the measured vertical stiffnesses were lower by 7 to 19% than the design predictions [EESK 2007]. The results of the horizontal shear tests allowed the shear modulus to be calculated and the vertical stiffness tests could provide an estimate of the bulk modulus. A complication in this case was that all the bearings had a small central hole that was not filled with rubber. At first sight it would seem that such a small hole would have no effect on the vertical stiffness but it was an unexpected result of the theory of bearings both when incompressibility was assumed and when the material was modeled as compressible that the presence of even a very small hole had a large effect on the stiffness and that the hole could not be ignored.

The test results were analyzed using the bearing mechanics theory [Gent and Meinecke 1970] to provide an estimate of the bulk modulus for this particular compound and to show how, if tests on bearings with other compounds are available, to interpret the data for this purpose.

2. Compression of pad within incompressible theory

A linear elastic theory is the most common method used to predict the compression stiffness of a thin elastomeric pad. The first analysis of the compression stiffness was done using an energy approach [Rocard 1937]; further developments were made two decades later [Gent and Lindley 1959; Gent and Meinecke 1970]. The theory given here is a simplified version of these analyses and is applicable to bearings with shape factors (S) in the approximate range $5 < S < 10$.

The analysis is an approximation based on a number of assumptions. Two kinematic assumptions are as follows [Gent and Lindley 1959]:

- (i) Points on a vertical line before deformation lie on a parabola after loading applied.
- (ii) Horizontal planes remain horizontal.

Consider an arbitrarily shaped pad of thickness t and locate a rectangular Cartesian coordinate system, (x, y, z) , in the middle surface of the pad, as shown on the left in Figure 1. The right-hand side of the figure shows the displacements, (u, v, w) , in the coordinate directions under assumptions (i) and (ii):

$$u(x, y, z) = u_0(x, y) \left(1 - \frac{4z^2}{t^2}\right), \quad v(x, y, z) = v_0(x, y) \left(1 - \frac{4z^2}{t^2}\right), \quad w(x, y, z) = w(z). \quad (2-1)$$

This displacement field equation (2-1) satisfies the constraint that the top and bottom surfaces of the pad are bonded to rigid substrates. The assumption of incompressibility produces a further constraint on

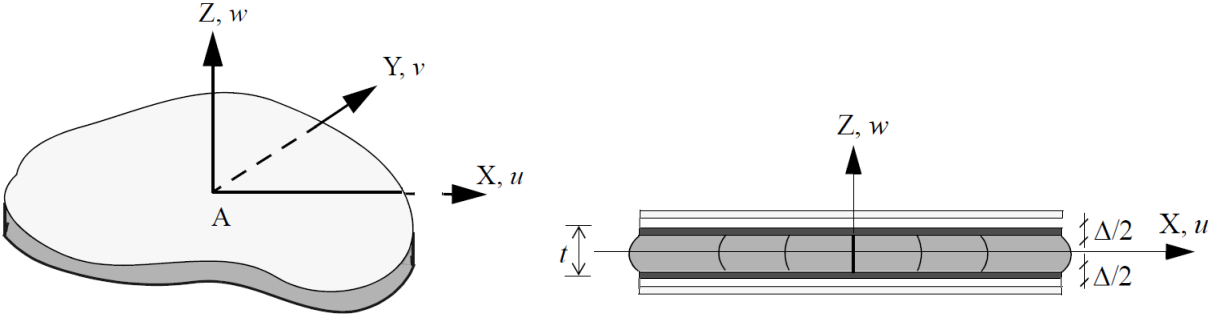


Figure 1. Constrained rubber pad and coordinate system.

the three components of strain, ϵ_{xx} , ϵ_{yy} , ϵ_{zz} , in the form

$$\epsilon_{xx} + \epsilon_{yy} + \epsilon_{zz} = 0. \quad (2-2)$$

Along with (2-1), this leads to

$$(u_{0,x} + v_{0,y}) \left(1 - \frac{4z^2}{t^2}\right) + w_{,z} = 0,$$

where the commas imply partial differentiation with respect to the indicated coordinate. When integrated through the thickness this gives

$$u_{0,x} + v_{0,y} = \frac{3\Delta}{2t}, \quad (2-3)$$

where the change of thickness of the pad is Δ (assume $\Delta > 0$ in compression).

The stress state is assumed to be dominated by the internal pressure, p , such that the normal stress components, τ_{xx} , τ_{yy} , τ_{zz} , differ from $-p$ only by terms of order $(t^2/l^2)p$, i.e.,

$$\tau_{xx} \approx \tau_{yy} \approx \tau_{zz} \approx -p \left[1 + O\left(\frac{t^2}{l^2}\right)\right],$$

where l is a typical dimension of the pad. The shear stress components, τ_{xz} and τ_{yz} , which are generated by the constraints at the top and bottom of the pad, are assumed to be of order $(t/l)p$; the in-plane shear stress, τ_{xy} , is assumed to be of order $(t^2/l^2)p$.

The equilibrium equations of the stresses under these assumptions reduce to

$$\tau_{xx,x} + \tau_{xz,z} = 0, \quad \tau_{yy,y} + \tau_{yz,z} = 0. \quad (2-4)$$

Assuming that the material is linearly elastic, then shear stresses τ_{xz} and τ_{yz} are related to the shear strains, γ_{xz} and γ_{yz} , by

$$\tau_{xz} = G\gamma_{xz}, \quad \tau_{yz} = G\gamma_{yz},$$

with G being the shear modulus of the material; thus,

$$\tau_{xz} = -8Gu_0 \frac{z}{t^2}, \quad \tau_{yz} = -8Gv_0 \frac{z}{t^2}. \quad (2-5)$$

From the equilibrium equations (2-4), therefore,

$$\tau_{xx,x} = \frac{8Gu_0}{t^2}, \quad \tau_{yy,y} = \frac{8Gv_0}{t^2}, \quad (2-6)$$

which when inverted to give u_0, v_0 and inserted into (2-3) gives

$$\frac{t^2}{8G}(\tau_{xx,xx} + \tau_{yy,yy}) = \frac{3\Delta}{2t}. \quad (2-7)$$

In turn, by identifying both τ_{xx} and τ_{yy} as $-p$, this reduces to

$$p_{,xx} + p_{,yy} = \nabla^2 p = -\frac{12G\Delta}{t^3} = -\frac{12G}{t^2}\epsilon_c, \quad (2-8)$$

where $\epsilon_c = \Delta/t$ is the compression strain. The boundary condition, $p = 0$, on the perimeter of the pad completes the system for $p(x, y)$.

The vertical stiffness of a rubber bearing is given by the formula

$$K_V = \frac{E_c A}{t_r},$$

where A is the area of the bearing, t_r is the total thickness of rubber in the bearing and E_c is the instantaneous compression modulus of the rubber-steel composite under the specified level of vertical load. The value of E_c for a single rubber layer is controlled by the shape factor, S , defined as

$$S = \frac{\text{load area}}{\text{force-free (bulge) area}}.$$

This is a dimensionless measure of the aspect ratio of the single layer of the elastomer. Typical shape factors for bearings of different shapes are as follows, where t is the single-layer thickness:

$$\frac{b}{t} \quad \text{for an infinite strip of width } 2b,$$

$$\frac{R}{2t} \quad \text{for an circular pad of radius } R,$$

$$\frac{a}{4t} \quad \text{for a square pad of side length } a.$$

To determine the compression modulus, E_c , one needs to solve for p and integrate over the cross section area A of the pad to determine the resultant normal load, P ; where E_c is then given by

$$E_c = \frac{P}{A\epsilon_c}, \quad (2-9)$$

where A is the area of the pad.

For example, for a circular pad of radius R , as shown in [Figure 2](#), [Equation \(2-8\)](#) reduces to

$$\nabla^2 p = \frac{d^2 p}{dr^2} + \frac{1}{r} \frac{dp}{dr} = -\frac{12G}{t^2}\epsilon_c, \quad r = \sqrt{x^2 + y^2}. \quad (2-10)$$

The solution is [\[Kelly 1997\]](#)

$$p = A \ln r + B - \frac{3G}{t^2} r^2 \epsilon_c,$$

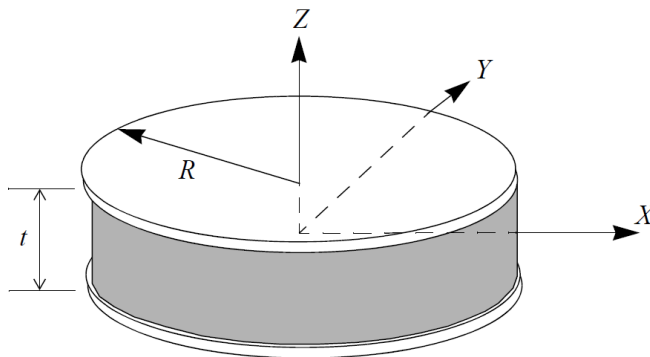


Figure 2. Coordinate system for a circular pad of radius R .

where A and B are constants of integration; because p must be bounded at $r = 0$ and $p = 0$ at $r = R$, the solution becomes

$$p = \frac{3G}{t^2} (R^2 - r^2) \epsilon_c. \quad (2-11)$$

It follows that

$$P = 2\pi \int_0^R p(r) r \, dr = \frac{3G\pi R^4}{2t^2} \epsilon_c, \quad (2-12)$$

and with $S = R/2t$ and $A = \pi R^2$, we have $E_c = 6GS^2$.

2.1. Annular pad. Consider an annular pad with inside radius a , external radius b , and thickness t . The shape factor in this case is

$$S = \frac{\pi(b^2 - a^2)}{2\pi(a + b)t} = \frac{b - a}{2t}. \quad (2-13)$$

The solution of (2-10), with $p(a) = 0$ and $p(b) = 0$, is

$$p(r) = \frac{3G}{t^2} \epsilon_c \left(\frac{(b^2 - a^2) \ln \frac{r}{a}}{\ln \frac{b}{a}} - (r^2 - a^2) \right). \quad (2-14)$$

The total load, P , is given by

$$P = 2\pi \int_a^b p(r) r \, dr = \frac{6\pi G}{t^2} \epsilon_c \frac{b^2 - a^2}{4} \left((b^2 + a^2) - \frac{b^2 - a^2}{\ln \frac{b}{a}} \right), \quad (2-15)$$

from which we have

$$E_c = \frac{P}{A\epsilon_c} = \frac{3G}{2t^2} \left((b^2 + a^2) - \frac{b^2 - a^2}{\ln \frac{b}{a}} \right). \quad (2-16)$$

Using the usual expression for S , we can write this in the form

$$E_c = 6GS^2\lambda, \quad (2-17)$$

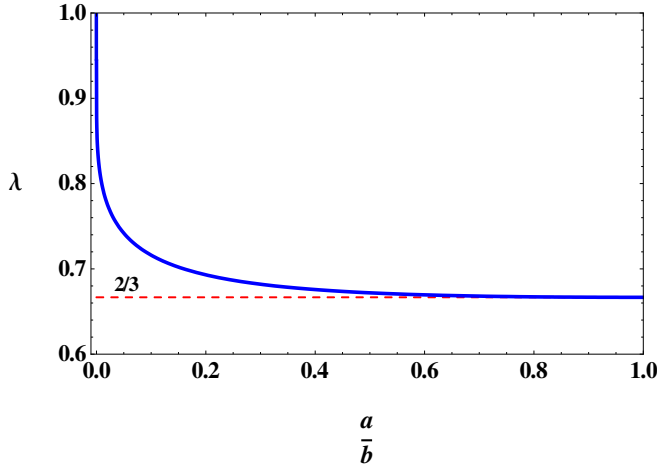


Figure 3. Reduction of compression modulus, E_c , for an annular pad [Kelly 1997].

where

$$\lambda = \frac{(b^2 + a^2) - \frac{b^2 - a^2}{\ln(b/a)}}{(b - a)^2}, \quad (2-18)$$

which, in terms of the ratio a/b , becomes

$$\lambda = \frac{1 + \left(\frac{a}{b}\right)^2 + \frac{1 - (a/b)^2}{\ln(a/b)}}{\left(1 - \frac{a}{b}\right)^2}. \quad (2-19)$$

When a/b tends to 0, the value of λ tends to 1; hence, $E_c \rightarrow 6GS^2$, which is the result for the full circular pad. When a/b tends to 1, by writing $a/b = 1 - \epsilon$ and letting ϵ tend to 0, we find that λ tends to $\frac{2}{3}$ and E_c to $4GS^2$, which is the result for the infinite strip. It is interesting to evaluate how rapidly the result for λ approaches $\frac{2}{3}$. To illustrate this point, we plot in Figure 3 the solution for λ versus the ratio a/b , for $0 < a/b \leq 1$.

Clearly for the case when $a/b > 0.10$, the value of λ is almost two-thirds, indicating that the presence of even a small hole has a large effect on E_c , therefore, in most cases for bearings with central holes, the value of E_c should be taken as $4GS^2$ rather than $6GS^2$.

3. Compression stiffness for circular pads with large shape factors

The theory for the compression of a rubber pad given in the preceding section is based on two assumptions: first, the displacement pattern determined in (2-1); second, the normal stress components in all three directions can be approximated by the pressure, p , in the material. The equation that is solved for p is the integration through the thickness of the pad of the equation of incompressibility (2-2), leading to an equation for $p(x, y)$ of the form given in (2-8). To include the influence of bulk compressibility, we

need only replace the equation of incompressibility constraint (2-2) by

$$\epsilon_{xx} + \epsilon_{yy} + \epsilon_{zz} = -\frac{p}{K},$$

where K is the bulk modulus. Integration through the thickness leads to an equation for $p(x, y)$ of the form

$$\nabla^2 p - \frac{12p}{t^2} \frac{G}{K} = -\frac{12G}{t^2} \epsilon_c, \quad (3-1)$$

which is solved as before, with $p = 0$ on the edge of the pad.

We now consider a circular pad with a large shape factor, an external radius, R , and thickness, t . The pressure in the pad is axisymmetric: $p = p(r)$, where $0 \leq r \leq R$; therefore, (3-1) becomes

$$\frac{d^2 p}{dr^2} + \frac{1}{r} \frac{dp}{dr} - \lambda^2 (p - K \epsilon_c) = 0, \quad \lambda^2 = \frac{12G}{K t^2} \quad (3-2)$$

with $p = 0$ at $r = R$.

The solution involves I_0 and K_0 , the modified Bessel functions of the first and second kind [Kelly 1997]. Because the solution is bounded at $r = 0$, the term in K_0 is excluded and the general solution for $p(r)$ is given by

$$p(r) = K \left(1 - \frac{I_0(\lambda r)}{I_0(\lambda R)} \right) \epsilon_c. \quad (3-3)$$

Integrating p over the area of the pad gives

$$P = K \pi R^2 \left(1 - \frac{2}{\lambda R} \frac{I_1(\lambda R)}{I_0(\lambda R)} \right) \epsilon_c,$$

where I_1 is the modified Bessel function of first kind of order one. The resulting expression for the compression modulus is

$$E_c = K \left(1 - \frac{2}{\lambda R} \frac{I_1(\lambda R)}{I_0(\lambda R)} \right), \quad (3-4)$$

where

$$\lambda R = \sqrt{\frac{12G R^2}{K t^2}} = \sqrt{\frac{48G}{K}} S$$

and the shape factor S equals $\frac{R}{2t}$.

3.1. Annular pad. In the case of a pad of inside radius a and outside radius b the solution of (3-2) is [Constantinou et al. 1992]

$$p(r) = (A I_0(\lambda r) + B K_0(\lambda r) + 1) K \epsilon_c, \quad (3-5)$$

and the fact that $p(a) = 0$ and $p(b) = 0$ leads to

$$A = -\frac{[K_0(\lambda b) - K_0(\lambda a)]}{I_0(\lambda a) K_0(\lambda b) - I_0(\lambda b) K_0(\lambda a)}, \quad B = \frac{[I_0(\lambda b) - I_0(\lambda a)]}{I_0(\lambda a) K_0(\lambda b) - I_0(\lambda b) K_0(\lambda a)}.$$

Integrating (3-5) with these values of A and B gives for P the value

$$2\pi K \epsilon_c \left((K_0(\lambda b) - K_0(\lambda a))(\lambda b I_1(\lambda b) - \lambda a I_1(\lambda a)) + (I_0(\lambda b) - I_0(\lambda a))(\lambda b K_1(\lambda b) - \lambda a K_1(\lambda a)) + \frac{b^2 - a^2}{2} \right),$$

from which using (2-9) leads to the result

$$E_c = K \left(1 - \frac{2(K_0(\lambda b) - K_0(\lambda a))(\lambda b I_1(\lambda b) - \lambda a I_1(\lambda a))}{\lambda^2(b^2 - a^2)(I_0(\lambda a)K_0(\lambda b) - I_0(\lambda b)K_0(\lambda a))} - \frac{2(I_0(\lambda b) - I_0(\lambda a))(\lambda b K_1(\lambda b) - \lambda a K_1(\lambda a))}{\lambda^2(b^2 - a^2)(I_0(\lambda a)K_0(\lambda b) - I_0(\lambda b)K_0(\lambda a))} \right). \quad (3-6)$$

To use this result to determine the bulk modulus from the test data we first normalize E_c with respect to $6GS^2$, the value for a complete pad based on the radius R (here = b) when incompressibility is assumed, and note that

$$\lambda^2 R^2 = \frac{48GS^2}{K},$$

so that

$$\frac{K}{6GS^2} = \frac{8}{\lambda^2 R^2}.$$

To account for the small hole in the tested pads we set $b = R$ and $a = \epsilon R$, where ϵ is less than 0.1 in the two examples tested.

When compressibility is included, the presence of a small hole has a large effect on the compression modulus. To show this, we combine

$$y = \frac{E_c}{6GS^2} \quad \text{and} \quad x = \lambda R$$

with (3-6), obtaining the result

$$y = \frac{8}{x^2} \left(1 - \frac{2}{x} \cdot \frac{A_1 + A_2}{A_3} \right), \quad (3-7)$$

where

$$A_1 = (K_0(x) - K_0(\epsilon x))(I_1(x) - \epsilon I_1(\epsilon x)),$$

$$A_2 = (K_1(x) - \epsilon K_1(\epsilon x))(I_0(x) - I_0(\epsilon x)),$$

$$A_3 = I_0(\epsilon x)K_0(x) - I_0(x)K_0(\epsilon x).$$

Suppose we take particular values of G , K , S based on no hole and vary ϵ . It is then clear that the hole has a large effect. Let $G = 0.9375$ MPa, $K = 2000$ MPa and $S = 20$ for which the value of $x = 3$ in this case. The value of the normalized modulus y when $\epsilon = 0$ is 0.4089 and the curve of y as a function of ϵ over the range $0 \leq \epsilon \leq 0.1$ is shown in Figure 4. It is obvious that the slope of the curve at zero is negative infinity and this is what produces the large effect on the modulus.

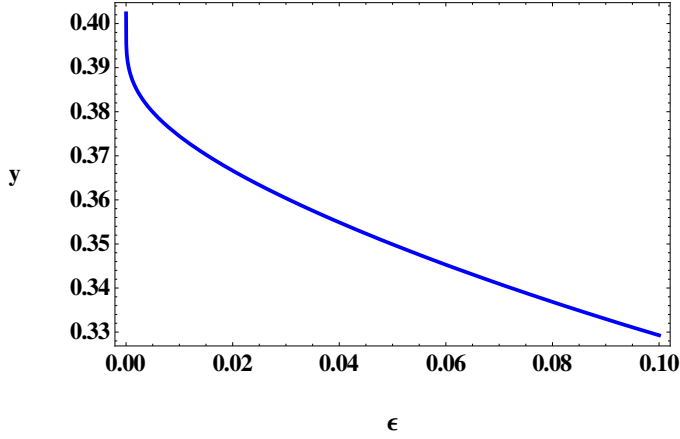


Figure 4. Reduction of normalized modulus, y , for an annular pad.

4. Influence of compressibility on buckling of bearings

It will be necessary to demonstrate that the buckling load of both types of bearings are sufficiently high in comparison to the design and test loads that there is no interaction between the axial load and the horizontal stiffness. The horizontal stiffness measurements will be used to provide the actual value of the shear modulus. Note that the presence of a small hole has a large effect on the vertical stiffness and has very little effect on the response of a bending moment. When computing the bending stiffness of a bearing, the hole can be ignored. However, the bending stiffness plays an essential role in the determination of the buckling load of a bearing. It has been shown [Kelly 1997] that bulk compressibility in the rubber has a surprisingly large effect on both the compression stiffness and bending stiffness of a bearing even for shape factors as low as 10. The buckling load P_{cr} of a bearing is given by [Kelly 1997]

$$P_{cr} = \sqrt{P_S P_E}, \quad (4-1)$$

where

$$P_S = GA \cdot \frac{h}{t_r} \quad \text{and} \quad P_E = \frac{\pi^2}{h^2} \cdot \left(\frac{1}{3} E_c I\right) \cdot \frac{h}{t_r}, \quad (4-2)$$

leading to

$$P_{cr} = \left(GA \frac{h}{t_r}\right)^{1/2} \left(\frac{\pi^2}{h^2} \frac{1}{3} 6GS^2 Ar^2 \frac{h}{t_r}\right)^{1/2} = \sqrt{GA \frac{h}{t_r} \frac{\pi^2}{h^2} \frac{1}{3} 6GS^2 Ar^2 \frac{h}{t_r}} = \sqrt{2 \frac{\pi^2}{h^2} G^2 S^2 A^2 r^2},$$

$$P_{cr} = \frac{\sqrt{2\pi} G S A r}{t_r},$$

where the radius of gyration is denoted by $r = \sqrt{I/A} = \Phi/4$, for a circular bearing with diameter, Φ . The critical pressure, $p_{cr} = P_{cr}/A$, can be expressed in terms of S and the quantity S_2 , referred to as the aspect ratio or the *second shape factor*, defined by

$$S_2 = \frac{\Phi}{t_r}.$$

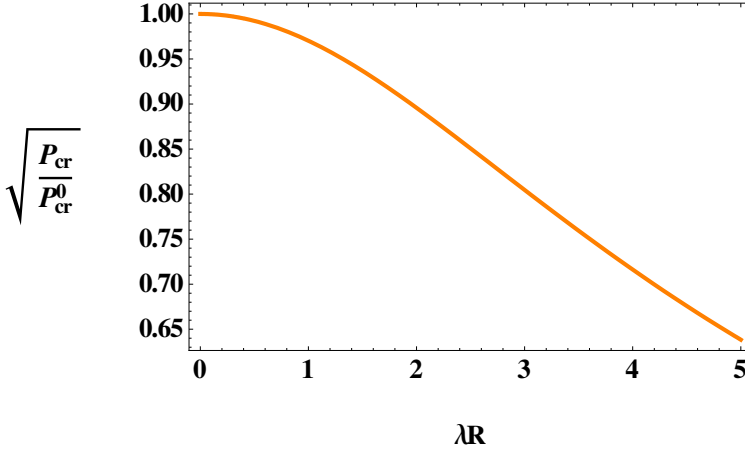


Figure 5. Effect of compressibility on buckling load of a bearing.

Thus, for a circular bearing

$$\frac{P_{cr}}{G} = \frac{\pi}{2\sqrt{2}} S S_2. \quad (4-3)$$

The impression given by (4-3) is that it is possible to improve the stability of a bearing with a certain diameter and thickness of rubber by the simple process of increasing the shape factor, i.e., increasing the number of layers and reducing their thickness. However, because of the effect of bulk compressibility on the effective stiffness, the improvement is limited. The expression $\frac{1}{3} E_c I$ in (4-2) is the effective bending stiffness $(EI)_{\text{eff}}$ of a pad when the material is assumed to be incompressible and we will denote it by $(EI)_{\text{inc}} = 2GS^2I$. We assume that the buckling load is given by the solution in (4-1), but substitute for $(EI)_{\text{eff}}$ the expression [Kelly 1997]

$$(EI)_{\text{eff}} = \frac{\pi K R^4}{4} \left(1 - \frac{4I_2(\lambda R)}{\lambda R I_1(\lambda R)} \right),$$

where $\lambda R = \sqrt{48GS^2/K}$. The resulting value of the critical load can be reduced to an expression depending only on the quantity λR , by dividing by the result for the critical load when the material is taken as incompressible, leading to

$$\left(\frac{P_{cr}}{P_{cr}^0} \right)^2 = \frac{24}{\lambda^2 R^2} \left(1 - \frac{4I_2(\lambda R)}{\lambda R I_1(\lambda R)} \right).$$

The reduction in terms of the varying shape factor are shown in Figure 5. The most convenient way to calculate the buckling load when bulk compressibility is included is to note that GA is unchanged, so that we have

$$P_{cr} = P_{\text{inc}} \sqrt{\frac{EI_{\text{eff}}}{EI_{\text{inc}}}},$$

where P_{cr} is the critical load for the compressible case and P_{inc} that for the incompressible case. The easiest way to estimate the buckling pressure for the two types of bearings is to calculate the buckling

property	RB2	RB3
diameter of bearing (mm)	900	850
diameter of steel plate (mm)	860	810
diameter of hole (mm)	60	60
number of rubber layers	48	48
rubber thickness per layer (mm)	6	6
number of test specimens	20	20

Table 1. Dimensions of the two types of bearings [EESK 2007].

pressure assuming incompressibility and then reduce this by the factor

$$\sqrt{\frac{24}{\lambda^2 R^2} \left(1 - \frac{4I_2(\lambda R)}{\lambda R I_1(\lambda R)} \right)},$$

using the nominal values of G and K to compute the appropriate values of λR in the reduction factor.

There are two types of isolators in the test program, designated RB2 and RB3 [EESK 2007]. Twenty bearings of each type were tested for horizontal stiffness and vertical stiffness. The rubber compound, individual rubber layer thickness and the number of layers are the same for both types. The differences between the two types are the rubber diameters and the steel shim diameters. Both types have a small central hole of 60 mm diameter that is not filled with rubber. The dimension of the bearings are given in Table 1. The nominal shear modulus of the compound is 0.40 MPa and we assume that the value of K for the purpose of this estimate of the buckling pressure is 2000 MPa. For the dimensions of RB2 and these nominal moduli, the P_{inc} for RB2 is 52 MPa and for RB3 is 46.4 MPa. The value of $\lambda^2 R^2$ for RB2 is 13.5 giving a reduction factor of 0.744 and for RB3 these are 12.0 and 0.7625 respectively. Thus the critical pressures are 38.7 MPa for RB2 and 35.4 MPa for RB3. The interaction between the horizontal stiffness and the vertical load in an elastomeric bearing is given by the expression [Kelly 1997]

$$K_H = \frac{GA_S}{h} \left(1 - \left(\frac{P}{P_{cr}} \right)^2 \right),$$

where P is the actual compressive load; the same equation applies to the pressures, which are 10.29 MPa and 7.61 MPa, respectively, so that the effect is negligible.

5. Test results for the two bearing types

To compute the actual shear modulus of the compound, we use the horizontal stiffness and the full rubber diameter allowing for the area of the hole and for the compression modulus, we use the steel shim area again allowing for the presence of the hole. The shape factors that will be used to determine the bulk modulus through the normalized compression modulus are obtained from the full shim diameter (neglecting the hole) and are 35.83 for RB2 and 33.75 for RB3. The test results for the 20 bearings of each type are given in Table 2. The average horizontal stiffnesses are 0.877 MN/m for RB2 and 0.837 MN/m for RB3. The average vertical stiffnesses are 1947 MN/m for RB2 and 1635 MN/m for RB3. In the case

specimen	RB2		RB3	
	K_v (MN/m)	K_h (MN/m)	K_v (MN/m)	K_h (MN/m)
1	1866.53	0.843	1577.59	0.805
2	2022.69	0.870	1589.76	0.805
3	1902.96	0.870	1666.83	0.794
4	1886.03	0.854	1630.09	0.794
5	1979.11	0.939	1669.56	0.823
6	1955.13	0.868	1584.82	0.847
7	1951.63	0.843	1591.33	0.813
8	1981.81	0.864	1612.79	0.860
9	1951.99	0.835	1632.81	0.823
10	1934.86	0.868	1606.14	0.841
11	1916.89	0.939	1620.63	0.857
12	1877.72	0.854	1563.80	0.836
13	1930.42	0.825	1678.67	0.847
14	1909.77	0.825	1588.89	0.813
15	1950.82	0.864	1675.26	0.893
16	1900.65	0.835	1560.71	0.836
17	2055.71	0.962	1665.53	0.857
18	2034.03	0.962	1726.50	0.893
19	2013.98	0.914	1870.02	0.860
20	1924.18	0.914	1596.16	0.841
Average	1947.35	0.877	1635.39	0.837

Table 2. Test results for the RB2 and RB3 bearings.

of RB2 the average horizontal stiffness using the equation

$$K_h = \frac{GA}{t_r}$$

with the area $A = 0.6334 \text{ m}^2$ and $t_r = 0.288 \text{ m}$, the value of G is 0.399 MN/m^2 . The nominal value was 0.40 MN/m^2 . From this value of G and the value of the shape factor $S = 35.83$, we have $y = E_c/6GS^2 = 0.3157$ which when equated with (3-7) leads to $x = \lambda R = 3.277$ and this in turn using the definition of $\lambda R = \sqrt{48GS^2/K}$ leads to the value of K as 2361 MN/m^2 . The similar computations for RB3 give $G = 0.426 \text{ MN/m}^2$, $y = E_c/6GS^2 = 0.3159$, $x = \lambda R = 3.206$ and $K = 2266 \text{ MN/m}^2$. These results are very consistent with each other and suggest that one might safely assume that the modulus to be used in bearing design might be 2300 MN/m^2 . The surprising result is that there is such a large difference in the shear modulus between the two sets of bearings. Without knowing more about the construction process for each set it is difficult to explain why there should be such a difference, but it seems to be systematic rather than random.

6. Conclusion

It has been shown that it is possible to estimate the bulk modulus of natural rubber from test results on bearings used as seismic isolators. The estimated bulk moduli of rubber using the proposed method are reasonably consistent values for the bulk modulus given the difficulty of accurately measuring the vertical stiffness of a bearing in compression test machine. The extremely large stiffness and the relatively low level of the test pressure indicate that the vertical displacement is very small and small errors in this measurement will have a large influence on the calculation of the stiffness and on the estimate of the bulk modulus. Nevertheless it remains one of practical method to determine the bulk modulus from experimental results. What is somewhat surprising in this case is the difference between the shear modulus estimates for the two types of bearings. Given that there is not a great deal of difference between the sizes of each type, it is strange that the compound should give such a large difference in the modulus.

References

- [Constantinou et al. 1992] M. C. Constantinou, A. Kartoum, and J. M. Kelly, “Analysis of compression of hollow circular elastomeric bearings”, *Engin. Struct.* **14**:2 (1992), 103–111.
- [EESK 2007] Earthquake Engineering Society of Korea, “Report for the 2nd peer review on the design of Gimpo Gochon apartment structures with base isolation system (27 September 2007)”, Seoul, 2007.
- [Fuller et al. 1988] K. N. G. Fuller, M. J. Gregory, J. A. Harris, A. H. Muhr, A. D. Roberts, and A. Severson, “Engineering use of natural rubber”, Chapter 19 in *Natural rubber science and technology*, edited by A. D. Roberts, New York, 1988.
- [Gent and Lindley 1959] A. N. Gent and P. B. Lindley, “Compression of bonded rubber blocks”, *Proc. Inst. Mech. Engin.* **173**:3 (1959), 111–122.
- [Gent and Meinecke 1970] A. N. Gent and E. A. Meinecke, “Compression, bending and shear of bonded rubber blocks”, *Polymer Engin. Sci.* **10**:1 (1970), 48–53.
- [Kelly 1997] J. M. Kelly, *Earthquake-resistant design with rubber*, 2nd ed., Springer, London, 1997. ISBN: 3-540-76131-4.
- [Lindley 1992] P. B. Lindley, *Engineering design with natural rubber*, 5th ed., Malaysian Rubber Producers’ Research Association (MRPRA), 1992.
- [Rocard 1937] Y. Rocard, “Note sur le calcul des propriétés élastiques des supports en caoutchouc adhérent”, *J. Phys. Radium* **8** (1937), 197–203.

Received 13 Jul 2010. Accepted 24 Aug 2011.

JAMES M. KELLY: jmkelly@berkeley.edu
*Earthquake Engineering Research Center, University of California, Berkeley, 1301 South 46th Street,
Richmond CA 94804-4698, United States*

JIUN-WEI LAI: adrian-jwlai@berkeley.edu
*Department of Civil and Environmental Engineering, University of California, 760 Davis Hall, Berkeley, CA 94720-1710,
United States*

PASSIVE DAMPING DEVICES FOR EARTHQUAKE PROTECTION OF BRIDGES AND BUILDINGS

CHRISTIAN MEINHARDT, DANIEL SIEPE AND PETER NAWROTZKI

This contribution describes the practical application of tuned mass control systems (TMCS) to bridges and buildings. Besides the experimental verification of significant reduction effects, results the results of a theoretical analysis that document the achievable improvements on the seismic response even in case of large structural damping ratios, is presented. Optimization approaches for these passive control systems will be discussed as well as practical considerations regarding the resulting specification of the TMCS. For the discussion, theoretical approaches will be introduced and results of additional numerical calculations will be presented. Design considerations for the selection of the parameters of the TMCS that take into account the nonlinearities due to the possible decrease of structural stiffness and the increase of structural damping due to cracks and local damages, will be discussed as well.

In the context of TMCS, two example projects will be introduced. One example explains the application of TMCS systems to a low damped elevated bridge structure and design solutions for these systems are presented as well as in-situ test methodologies to verify the increase of structural damping. The other example describes the application of TMCS systems as part of a consolidation strategy to successfully retrofit a large RC-structure / masonry wall building. Results of numerical calculations — verified by in-situ ambient vibration measurements — that examine the reduction effect of the TMCS in combination with additional measures will be shown together with cost effective design solutions.

1. Introduction

Increasing the structural damping of constructions to reduce the dynamic response to seismic loading is a common and well-examined strategy which is considered as a correction factor for response spectra in several codes and standards (see [Figure 1](#)).

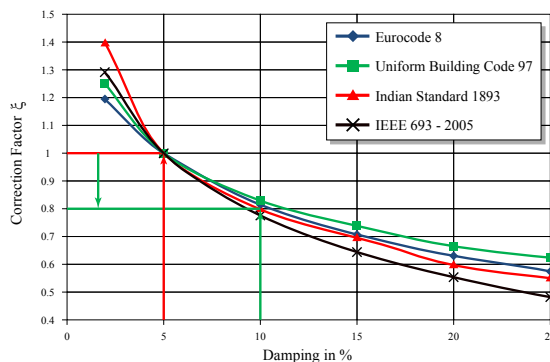


Figure 1. Effects of damping increase.

Keywords: passive damping devices, optimization approach, earthquake protection, tuned mass control systems.

One method to achieve an increase of structural damping is the application of passive energy absorbing devices such as tuned mass control systems (TMCS), though this method is still under debate. While some researchers have observed a noticeable reduction of the structural response to earthquake loads, the effectiveness has been denied by others.

Considering the evidence, which has been shown in experimental tests as described in [Section 2](#) and [\[Rakicevic et al. 2006\]](#) that passive appendages cause a reduction of the structural seismic response, it has been noticed in theoretical investigations that the effectiveness of these systems is strongly dependent on the specification of the guiding TMCS parameters such as effective mass, tuning frequency, and internal damping ratio. Since the commonly known optimization criteria formulated in [\[Den Hartog 1956\]](#) are only applicable for a harmonic excitation, these resulting conventional specifications do not lead to the desired reduction effects for earthquake loads.

To apply TMCS successfully, their specification has to be optimized by applying load characteristics that reflect those of seismic loading. In the following, several methods to estimate an optimum specification of TMCS for light dampened structures and also structures with bigger structural damping ratios will be discussed. The introduced methods are compared with numerical calculations. Additionally, the resulting specification shall be discussed under practical considerations.

The objective of this theoretical approach is the concrete practical application of TMCS equipment to an elevated bridge structure and to a RC structure/ masonry wall building by using the generalized results. In addition FE-models of both structures have been used to verify the effectiveness of the specified system and effects for practical considerations have been assessed. The results of the numerical analysis, the design, and the implementation of the TMCS units will be introduced in this contribution.

2. Experimental investigations

Several practical tests of a five-story steel frame model equipped with a TMCS, tested on a biaxial shaking table, have been performed at IZIS (Institute of Earthquake Engineering and Engineering Seismology) in Skopje, Macedonia. [Figure 2](#) shows a five-story steel frame model equipped with a TMCS, tested



Figure 2. Shaking table test of TMCS.

on a biaxial shaking table. The dimensions of the table are about 5.0 m in both horizontal directions. The shaking table is suitable for pay loads up to 30.0 tons and is able to generate horizontal acceleration of 1.0 g, as well as vertical acceleration of 0.5 g. Each floor of the steel structure has got a height of 0.75 m, while all three spans in the longitudinal direction amount to 1.5 m. The one span in transversal direction amounts to 1.5 m. The total mass of the steel structure is 19.0 tons, and the mass of the TMCS is 0.26 tons, which corresponds to about 1.3% of the entire mass. The structure in the middle span has a special bracing substructure (the red steel structure in [Figure 2](#)), which is used to adjust the required stiffness and damping for the tests.

At the beginning the modal parameters (natural frequencies, damping) of the structure have been tested and verified by different test methods (hammer test, steady-state vibration and random vibration test simulated by the shaking table). The main premises of the described tests were to investigate the reduction effects for different type of seismic load characteristics with different frequency contents so the structure underwent a couple of measured and artificial seismic waves with different intensities. Among them were several well-known seismic time-histories as Northridge, Kobe, Mexico City, Vrancea (Romania) and Izmit (Turkey).

The inherent structural damping of the steel frame has not been varied since the focus of the investigations was on the behavior of the system structure + TMCS under seismic loading.

The efficiency of the system was investigated by comparing the results of the frame with activated and with blocked TMCS.

At first, the model was tested with unlocked TMCS, and all selected earthquakes were simulated for minimum three different intensities. The same procedure has been repeated with the model with locked TMCS. During the tests time history responses of relative displacements, acceleration values and bending strains are recorded at different locations at the structure.

In [Figure 3](#) a comparison of relative displacements for three different earthquake time records at top of the structure shows an improvement of seismic performance by nearly 40%.

The investigations have shown that the TMCS reduces the structural responses by about 25–40%. In parallel to the experimental investigations also several numerical investigations have been performed. Qualitatively the results of these calculations correspond well to the measured data. For more information please refer to [\[Rakicevic et al. 2006\]](#).

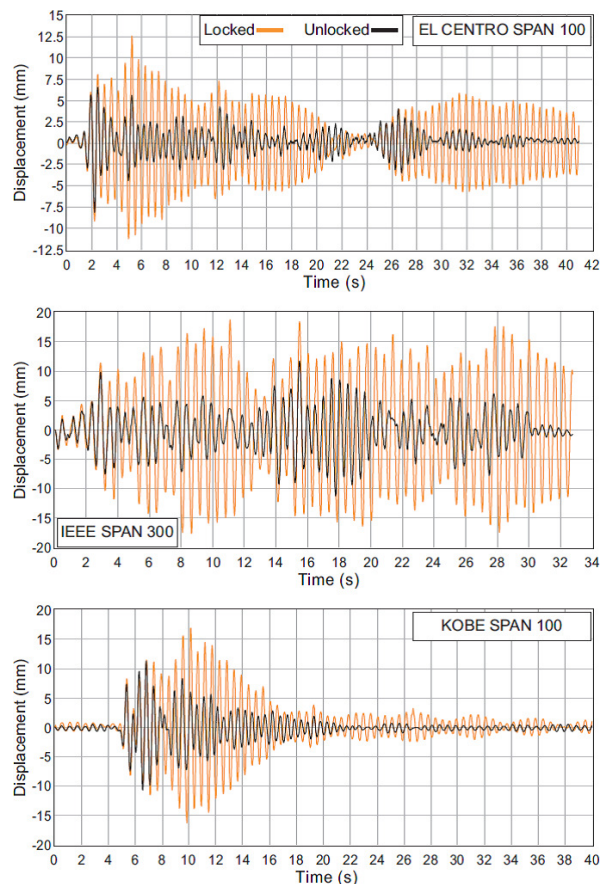


Figure 3. Recorded responses with activated (black curve) and locked TMCS (orange curve).

3. Theoretical investigations

Additionally to the experimental tests theoretical investigations have been performed for simplified analytical models, example structures and existing structures (e.g. bridges and buildings) with a focus on the optimization of the system specifications for the characteristics of seismic loading and for varying inherent structural damping ratios. Prior to detailed numerical calculations of the existing structures optimization approach was examined to determine the optimal parameters of the TMCS.

3.1. Optimization for a single-degree-of-freedom model. To derive an optimal specification for the TMCS, the characteristics of seismic loading has to be approximated. A legitimate approach is the assumption that ordinary earthquake excitation can be approximated with sufficient accuracy by a stationary white noise stochastic process (see Figure 4).

According to [Ayorinde and Warburton 1980] for an analogous model (see Figure 5) the optimization can be found by minimizing the variance σ_x^2 of the structural displacements X .

The displacement X is related to the constant white noise spectral density S_0 ; we have

$$\sigma_x^2 = [E(x^2(t))] = S_0 \int_{-\infty}^{\infty} |H(\nu)|^2 d\nu, \quad (1)$$

in which $H(\nu)$ is the complex response function of the displayed analogous model with the tuning frequency of the TMCS f_T and the natural frequency of the structure f_S .

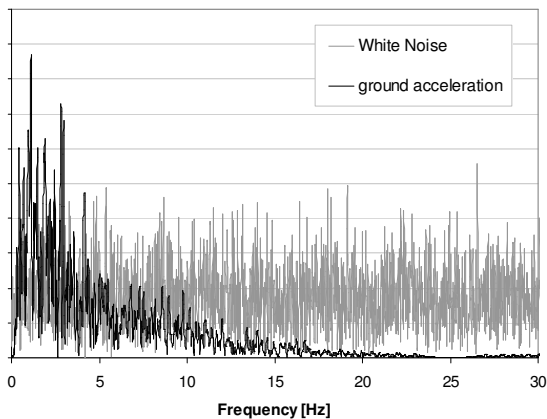


Figure 4. Frequency content of stationary random white noise and a measured ground acceleration time history.

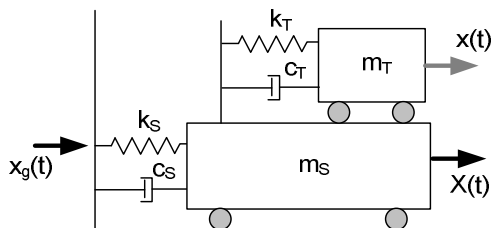


Figure 5. TMCS model as a two-degree-of-freedom appendage.

The complex response function amounts to

$$H(\nu) = \frac{\frac{m_T}{m_S} + \frac{\left(\frac{f_T}{f_S}\right)^2 + 2i\zeta_T\left(\frac{\nu}{f_S}\right)\frac{f_T}{f_S}}{\left(\frac{f_T}{f_S}\right)^2 - \frac{\nu}{f_S} + 2i\zeta_T\left(\frac{\nu}{f_S}\right)\frac{f_T}{f_S}}}{\frac{m_T}{m_S}\left(1 - \left(\frac{f_T}{f_S}\right)^2 + 2i\zeta_T\left(\frac{\nu}{f_S}\right)\frac{f_T}{f_S}\right)} \cdot \left(\frac{\nu}{f_S}\right)^2 \cdot \left(\frac{f_T}{f_S}\right)^2. \quad (2)$$

To optimize the TMCS parameters f_T and ζ_T a performance index J_0 has to be introduced that complies with the mentioned variance σ_x^2 :

$$J_0 = S_0 \int_{-\infty}^{\infty} |H(\nu)|^2 d\nu \quad (3)$$

The minimization process of J_0 can be expressed for slightly damped, or (better) undamped, structures in an analytical solution:

$$\left(\frac{f_T}{f_M}\right)_{\text{opt}} = \frac{\sqrt{1 - \frac{m_T}{2 \cdot m_S}}}{1 + \frac{m_T}{m_S}}, \quad (4)$$

$$\zeta_{\text{opt}} = \sqrt{\frac{\frac{m_T}{m_S}\left(1 - \frac{m_T}{4 \cdot m_S}\right)}{4 \cdot \left(1 + \frac{m_T}{m_S}\right) \cdot \left(1 - \frac{m_T}{2 \cdot m_S}\right)}}. \quad (5)$$

Assuming a low damping for most structures that require seismic control devices is absolutely inappropriate. Inherent structural damping for RC-structures has to be considered as well as the nonlinear damping behavior for large deformations that might occur during an earthquake. So there are other approaches by solving the complex eigenvalue problem $|\mathbf{A} - \lambda \mathbf{I}|$ that derives from the free vibration equation for a system matrix \mathbf{A} (see [Villaverde and Koyama 1993]); the problem can be written as

$$\begin{aligned} \left(\frac{\lambda}{\omega_0}\right)^4 + \left[2\frac{f_T}{f_M}\zeta_T\left(1 + \frac{m_T}{m_S}\right) + 2\beta\right]\left(\frac{\lambda}{\omega_0}\right)^3 + \left[1 + \frac{m_T}{m_S}\left(\frac{f_T}{f_M}\right)^2 + 4\frac{f_T}{f_M}\zeta_T\beta\right]\left(\frac{\lambda}{\omega_0}\right)^2 \\ + 2\frac{f_T}{f_M}\left(\zeta_T + \beta\left(\frac{f_T}{f_M}\right)\right)\frac{\lambda}{\omega_0} + \left(\frac{f_T}{f_M}\right)^2 = 0, \quad (6) \end{aligned}$$

which contains the stiffness and damping information of the main system (ω_0 and β), the mass ratio between the main structure and the TMCS and the TMCS parameters for the tuning-frequency and internal damping ratio.

The solution of the eigenvalue problem is in complex conjugate pairs with complex eigenvalues:

$$\lambda_{r,r+1} = -\bar{\omega}_r \zeta_r \pm i\bar{\omega}_r \sqrt{1 - \zeta_r^2} \quad (7)$$

The optimum TMCS specification is determined when the difference between the damping values ζ_{T1} and ζ_{T3} resulting from the eigenvalues is minimal.

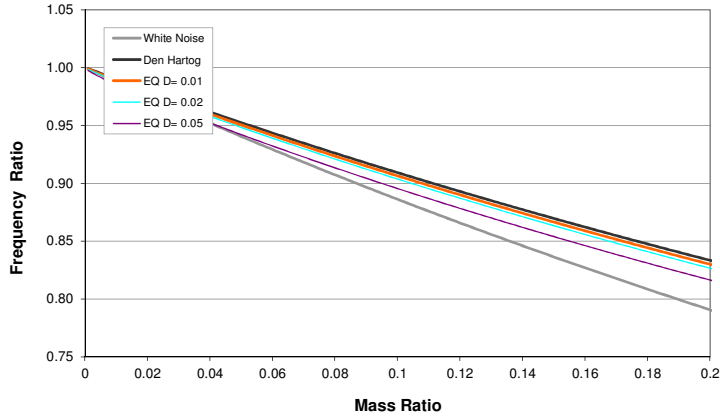


Figure 6. Optimum frequency ratio as a function of the mass ratio for different inherent damping ratios.

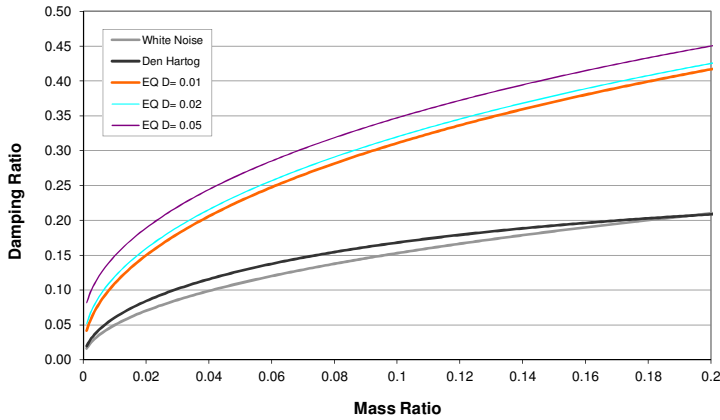


Figure 7. Optimum internal damping ratio as a function of the mass ratio.

The iterative analysis can be done numerically [Sadek et al. 1997] and leads to the optimum values, shown in Figures 6 and 7. As a comparison, the resulting values for an optimization according to Den Hartog and for an approach using white noise excitation are displayed as well.

3.2. Optimization for a multiple-degree-of-freedom model. To assess the reduction effect of TMCS on multiple-degree-of-freedom structures such as multistory buildings, numerical calculations of a six-story have been done for which a TMCS has been applied. The inherent damping ratios of the building, as well as the ratio between the modal mass of the relevant mode and the mass of the TMCS have been varied. The reduction has been assessed also for different internal damping ratios of the TMCS such as the optimal damping according to the Den Hartog optimization and the previously introduced criteria. The numerical analysis has been done for the time domain using ground acceleration time records from the Northridge Earthquake, the El Centro Earthquake and the USNRC standard time history. Figure 8, left, shows the time records that have been used for a one-directional base excitation. The numerical first horizontal bending mode is in range of the highest spectral density for each time record (Figure 8,

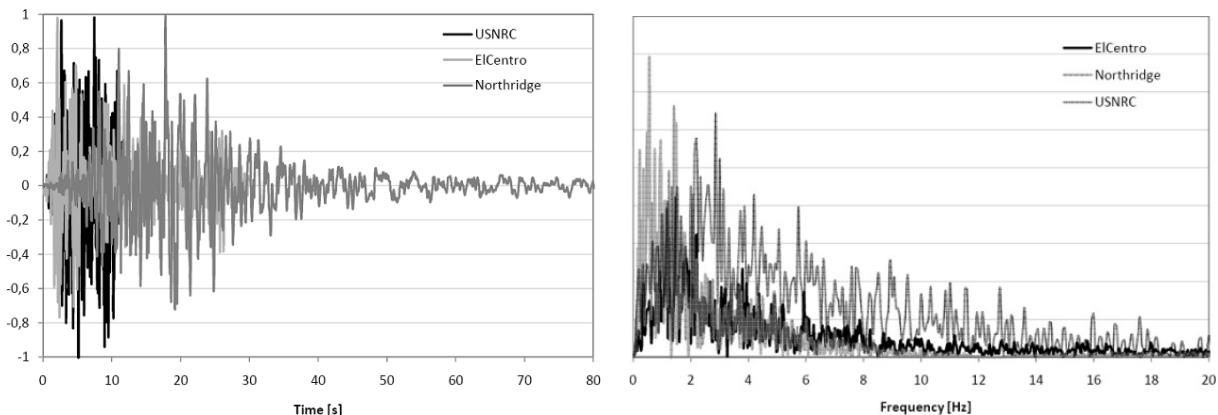


Figure 8. Left: time records of the applied earthquakes. Right: spectral density of the applied earthquakes.

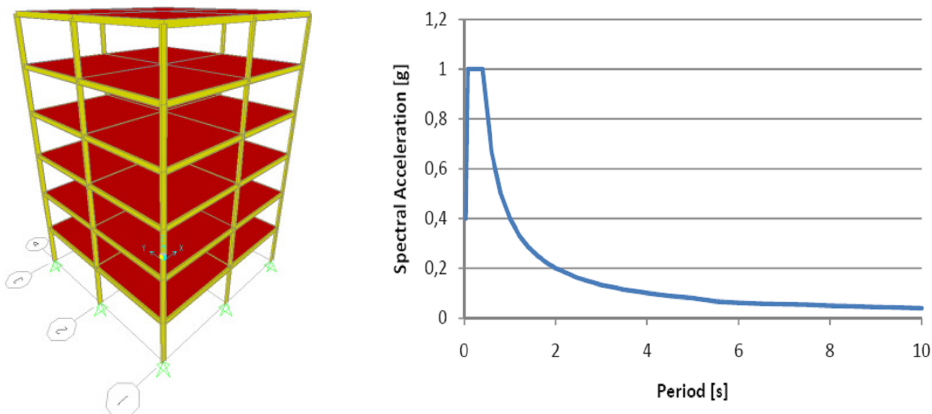


Figure 9. Left: model of the six-story building analyzed. Right: UBC 97 response spectrum used.

bottom), so it can be assumed that the structure has a sufficient dynamic response in that mode to which the TMCS is tuned for.

A response spectra analysis has also been performed with the same model and the same variation of the TMCS parameters to assess the reduction effect of a TMCS. For the analysis the UBC 97 response spectrum for 5% damping and a seismic coefficient of 0.4 has been used (Figure 9, right). The maximum displacements of the system with TMCS have been normalized to the displacements without TMCS to derive a reduction factor (u_T/u_0).

The calculated time responses of the building for the different ground acceleration time histories were transformed into the frequency domain to obtain an effective value u_e by deriving the square root of the sum-of-squares for each FFT-line (see Figure 10). Again a reduction factor (u_{Te}/u_{0e}) has been calculated to determine the TMCS effectiveness, where u_{Te} are the displacements of the structure TMCS and u_{0e} without.

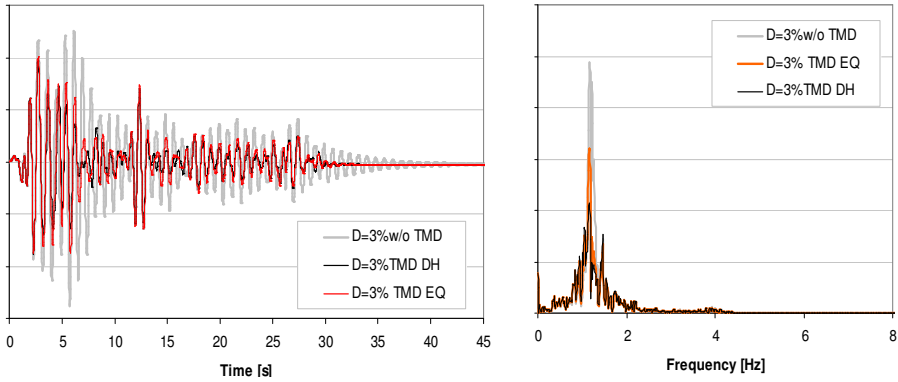


Figure 10. Left: calculated time responses of the model (3% inherent damping) without TMCs and with TMCs (DH = Den Hartog; EQ = specification and optimization according to [Ayorinde and Warburton 1980]). Right: corresponding frequency spectra to obtain the sum of squares.

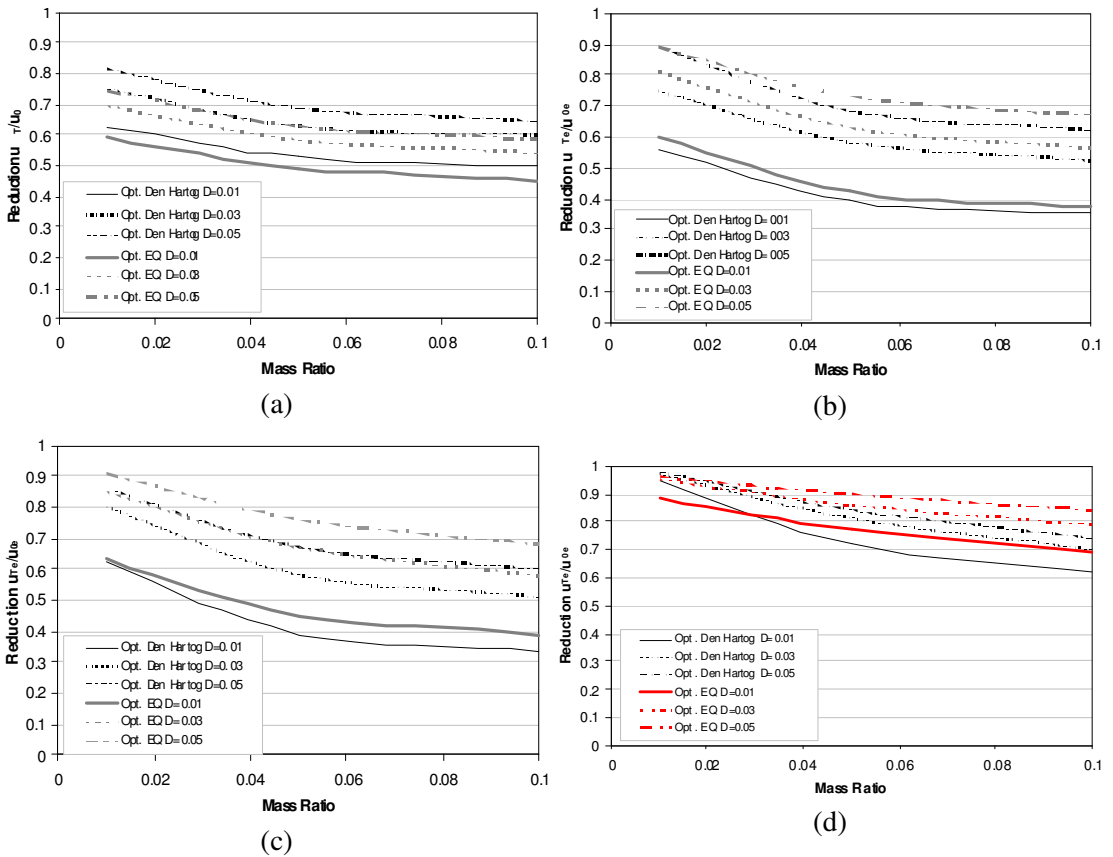


Figure 11. Calculated reduction factors for different inherent damping ratios and for different optimization approaches: response spectrum analysis (a), time domain analysis with the USNRC earthquake (b), El Centro earthquake (c), Northridge earthquake (d).

Figure 11 shows the calculated reduction factors against the mass ratio between the modal mass of the structures relevant mode and the mass of the applied TMCS for different inherent damping ratios of the structure. For the response spectrum analysis the maximum reduction that can be achieved is 55% for a big mass ratio and structures with a low inherent damping ratio. A reduction in excess of 30% can be achieved also for higher inherent damping ratios. It can be seen that a bigger reduction can be achieved when the optimized damping values are applied according to the introduced approach are applied.

The results from the performed time domain analyses show an even bigger reduction for the calculations with the time records of the El Centro and the USNRC earthquake. Only the calculations for the Northridge earthquake show a rather small reduction of the structural seismic response by the application of a TMCS (10–30%). In addition it can be noticed that an optimization of the internal damping doesn't increase the effectiveness as it was observed for the results of the response spectrum analysis. The cause for this effect can be found in the theory for a two-degree-of-freedom model where the amplification function of a highly damped appendage to a main system shows a reduced amplification over a broader frequency range than for appendages with lower damping. Considering a broad frequency range instead of a time response due to a stochastic time record, leads to the observed effect.

The characteristics of the applied earthquake-time records are also the reason of the varying results for the three different analyzed earthquakes. The USNRC earthquake and the El Centro earthquake have their highest energy content in the frequency range in which the analyzed building tends to respond, so the buildings response has a larger free-vibration participation than for the Northridge earthquake which has its highest energy contents at lower frequencies. By having a higher free vibration participation due to the characteristics of the ground acceleration time record, the TMCS also tends to be more effective for an Den Hartog optimizations since the building response has more harmonic components. In this regard, the difference of the reduction factors for an optimization according to Den Hartog and the optimization for seismic loads is less distinctive for the Northridge earthquake than for the USNRC and El Centro earthquakes.

In light of the results presented, it can be summarized that the application of a TMCS leads to a significant reduction for sufficient mass ratios if the internal damping ratio is bigger then the optimum value according to the optimization for harmonic loads (Den Hartog). A higher internal damping ratio of the TMCS leads to a better effectiveness for an excitation that leads to a smaller free-vibration participation of the structure.

The average value of the reduction factors for the three examined earthquakes is in range of those calculated for the response spectrum analysis. The effectiveness is more distinctive for lighter damped structures.

3.3. Practical considerations. For a practical application of a TMCS, additional effects that occur in reality have to be considered. Nonlinearities due to the structural degradation of the structure during seismic loading, such as the decrease of structural stiffness and the increase of structural damping due to cracks and local damages should be considered for the determination of the optimum device specification.

To assess the robustness of a TMCS specification regarding these two effects, the reduction factors of the introduced model were calculated varying for an inherent structural damping of 8% for different frequency ratios — actual tuning frequency of the TMCS to the optimum tuning frequency (see Figures 12 and 13).

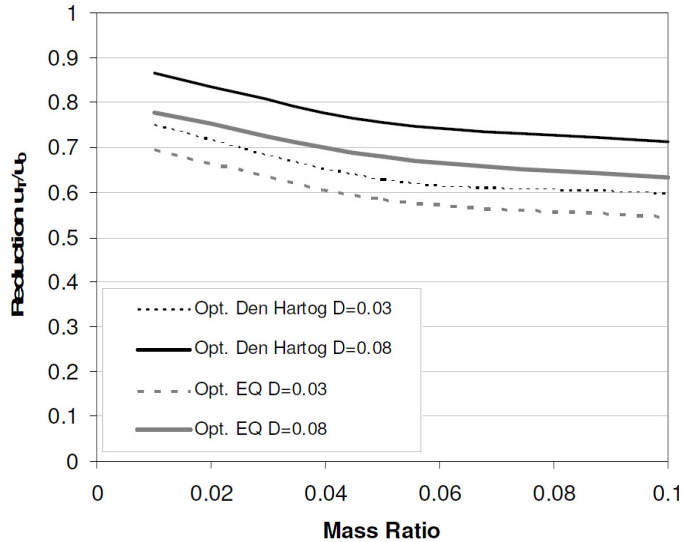


Figure 12. Calculated reduction factors for 8% inherent damping.

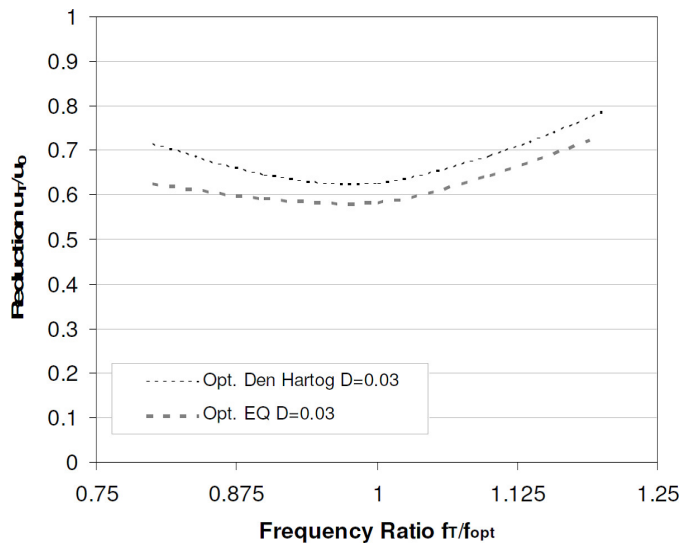


Figure 13. Calculated reduction factors for different frequency ratios.

The results show that the TMCS is more effective for a detuned system if a higher internal damping is applied. For this case the TMCS is effective in a broader frequency range, which matters when the stiffness of the structures decreases during an earthquake. It can also be seen that even with a big structural damping value a distinctive reduction can be achieved again if a higher internal damping is applied. Another point that has to be considered is the resulting displacements of the TMCS-mass. The higher internal damping ratio can again be used to reduce the resulting displacements.

4. Project example: TMCS for an elevated bridge structure

4.1. Introduction. The Puente Oriente, also known as Puente El Alamo, is an elevated bridge structure near Guadalajara, Mexico, and will be used as a fly-over distributor road for the local highway system.

The total length of the structure is approximately 500 m and the average span of each bay is 40 m. The substructure underneath the reinforced concrete deck consists of steel columns and two main steel beams with a trapezoidal cross section (see Figure 14). To reduce the rocking vibrations of the bridge deck under seismic loads, 8 TMCS units, each with an effective mass, have been applied underneath the deck in range of the central column structures (see Figures 15 and 20).



Figure 14. Bridge during construction.

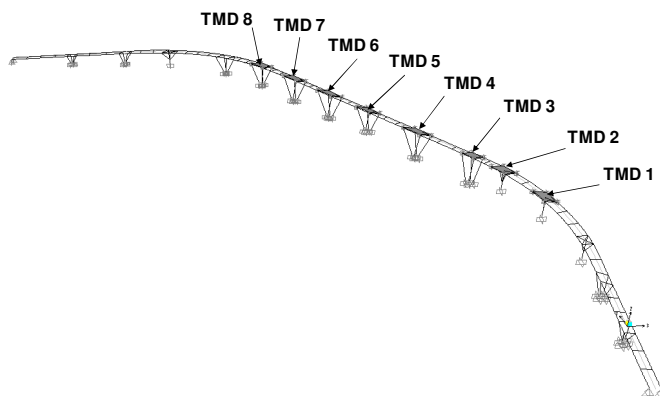


Figure 15. FE-Model of the bridge / positions of the TMD's.

Prior to the final design of the units several numerical calculation have been completed to determine an optimal mass ratio and to verify the corresponding specification according to the previously described procedures.

4.2. Specification of TMCS: calculation of the effectiveness of the designed devices. The bridge structure was modeled by using the commercial finite element program SAP2000 (CSI Berkeley, Inc.). A plot of the bridge and the 8 arranged masses is shown in Figure 15. The TMCS was modeled as single masses connected to the main structure by spring and damper elements. The parameters for these elements have been chosen according to the optimization criteria and verified variation calculations.

The structural response was calculated by performing a response spectrum analysis with and without TMCS units. The design spectrum (see Figure 16) was defined by the local authorities. The numerical modal analysis, which is necessary to accomplish the response spectrum analysis, showed that the relevant vibration mode is in range of 1.69 Hz (see Figure 17).

The resulting reduction factors of the occurring displacements and accelerations for load cases that consider the orientation of the bridge are shown in Figure 18.

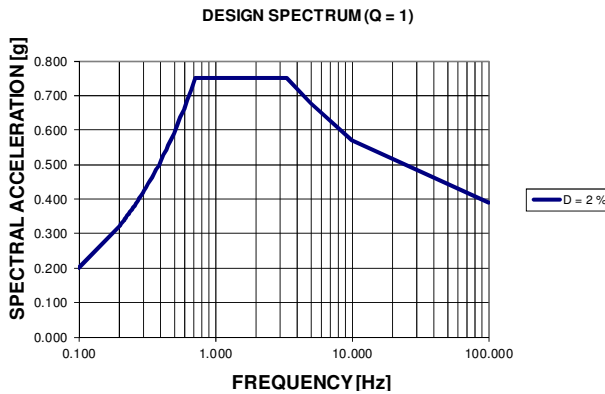


Figure 16. Design spectrum.

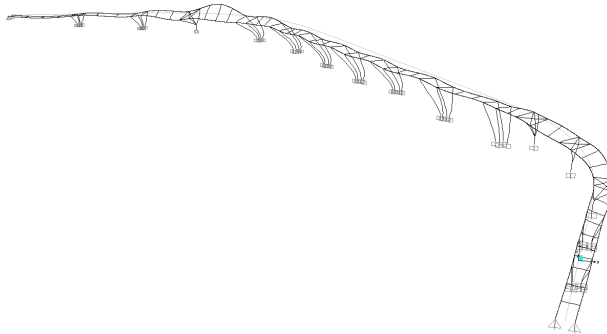


Figure 17. Relevant mode shape (1.69 Hz) of the bridge.

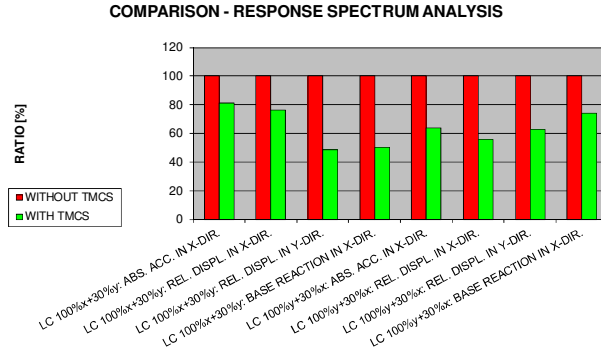


Figure 18. Reduction factors from the response spectrum analysis.

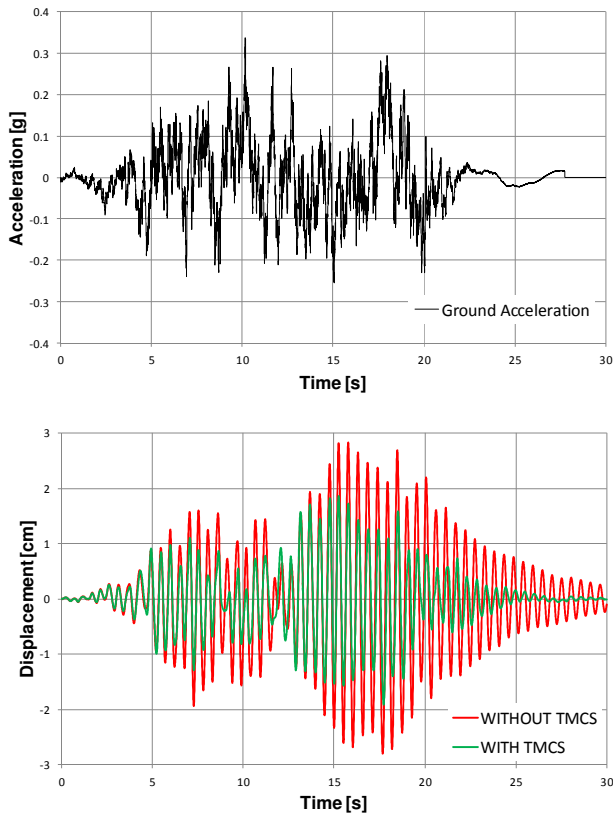


Figure 19. Top: Generated time history for ground acceleration. Bottom: structural responses without and with TMCS.

Additionally, an artificial time history of the ground acceleration has been generated using the given spectrum. [Figure 19](#) shows the input data and the structural response to that seismic load without and with TMCS.

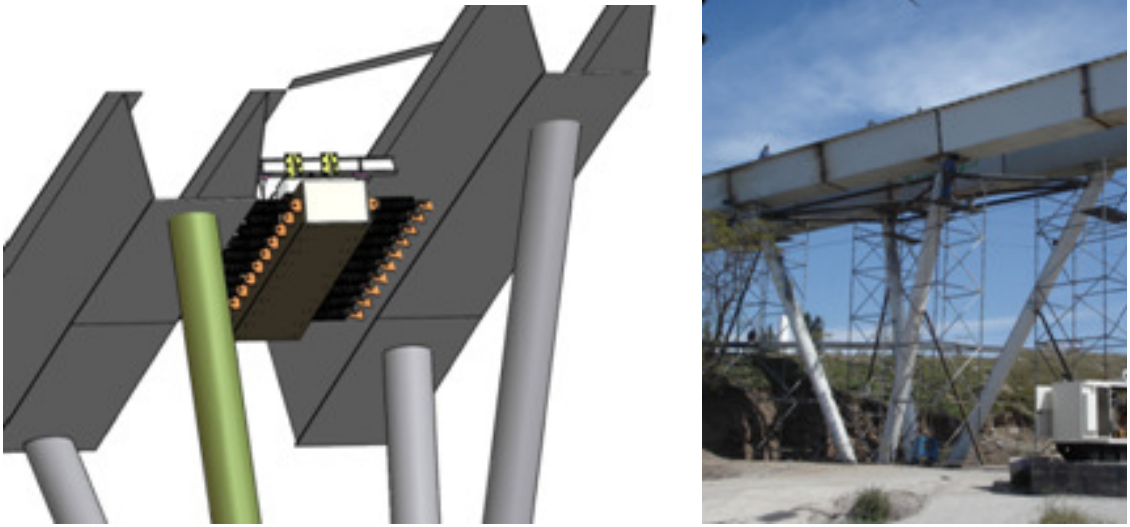


Figure 20. Left: TMCS at designated location. Right: bridge substructure prior to installation.

The results of the time history analyses show a significant reduction of the structural responses when a TMCS is applied. Qualitatively the results of the time history analysis correspond very well to the results of the response spectrum analysis. The numerical results of both types of analysis shows a high efficiency of the TMCS in regard to the earthquake protection.

4.3. TMCS design. The TMCS units were designed to be laterally effective once attached to the bridge deck. Each unit consists of an effective mass which has been designed as a concrete filled steel bin. The mass is supported on pendulum rods to allow frictionless oscillations.

The required internal damping is achieved by Viscodamper[®] (by GERB Vibration Control Systems) units that provide an ideal viscous damping behavior which is independent from the shear velocity. The damper can be adjusted by varying the shear area while the whole TMCS system can be tuned with horizontal tuning springs which connect the elastically supports mass and the main structure (see [Figure 20](#)).

Prior to installation, the damping units will be tested on a shaking table, where force/motion diagrams will be recorded to verify the units damping coefficient and to determine the additional stiffness of the damping unit that has to be considered for the tuning setup on site.

4.4. In situ tests. Once the TMCS units are installed, ambient vibration measurements at the bridge structure will be performed to assess the modal parameters (natural frequencies, corresponding mode shapes and damping ratios) of the bridge before the TMCS units will be adjusted on site.

Ambient vibration testing is more or less the only way to obtain the modal parameters of large structures as a forced excitation means a too big effort. The wind velocity spectrum and/or the traffic spectrum is showing content over a broad frequency range. It can again be assumed that the statistic average of the ambient excitation equates a white noise excitation, which excites all relevant structural modes. For this reason, ambient vibration records can be used to determine the natural frequencies and the structural damping of the bridge structure.

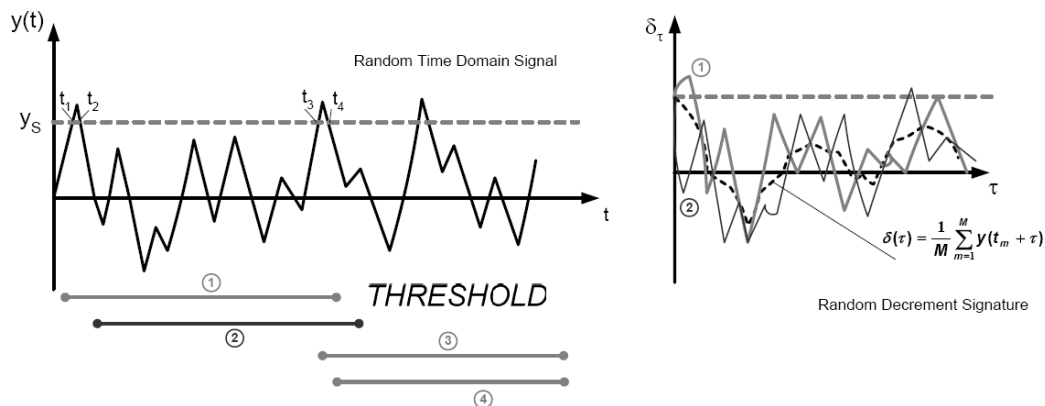


Figure 21. Principle of the random decrement method.

Several methods can be used to assess the damping using the ambient vibration records. For damping assessment, the random decrement method will be applied. The principle of this method is presented in [Figure 21](#).

Based on the theory that the random excitation consists of a deterministic component which corresponds to free vibration terms and a random component which corresponds to forced vibrations, the random part can be eliminated by averaging a large number of blocks that fulfill a certain threshold criteria and are extracted from the time domain signal with a certain length τ . The random decrement signature (RDS) results from the formula

$$\delta(\tau) = \frac{1}{M} \sum_{m=1}^M y(t_m + \tau), \quad (8)$$

and the resulting damping ratio can be derived by the known logarithmic decrement, whereas the quality of the RDS strongly depends on the selection of the segment duration τ and the threshold y_s .

The structural response for ambient excitation (wind and traffic) usually occurs in several modes. To withdraw the damping ratio for a single mode, the time records have to be processed with a bandpass filter for each relevant natural frequency. The random decrement method has been commonly accepted for system identification analyses of structures and buildings. The design of the TMCS and the excitation due to traffic with a comparatively high energy input allows the assessment of the TMCS effectiveness by comparing the structural damping with blocked and with activated TMD.

To assess the structural damping of the bridge structure with the random decrement method, recorded time histories of the vibration velocities in lateral direction with blocked and activated TMCS will be consulted. The signatures for several variations of the threshold will be normalized and averaged to achieve a stochastically approved damping ratio.

5. Project example: TMCS for a building

5.1. Introduction. The structure of the Palatul Victoria (see [Figure 22](#)) consists of 6 different parts, which are separated by joints. The clearance is very small and in case of an earthquake high interstorey



Figure 22. The Palatul Victoria in Bucharest, Romania.

drift ratios as well as hammering effects can be expected. Damages could result for columns, walls and panelling and the necessary repair work would be tremendous. As a consequence the building could experience a period of downtime, not acceptable due to the importance of this venue for the Government of Romania.

In order to prevent this scenario a suitable sequence of interventions was designed. In a first stage some of the building slabs were coupled in order to reduce relative motions between portions of the building. In order to reduce the interstory drift ratios traditional strengthening techniques were considered. Among them, the insertion of additional shear walls was decided even though limited in number and size by the existing structural configuration. The installation of shear walls had to be complemented by additional measures. For this purpose a suitable TMCS was developed.

5.2. Specification of TMCS: calculations. The building consists of reinforced concrete members, as well as of brickwork. The total length is about 95 m, the width about 52 m and the height of the main parts about 24 m. The total mass of the building is assessed at about 35,000 tons and the main frequencies are about 2.0 Hz in the longitudinal direction and 1.8 Hz in the transverse direction. These values vary slightly according to the different parts of the whole structure.

Using the finite element software SAP2000 a three dimensional model of the structure was prepared. The computer model was validated against the measured eigenfrequencies of the building. Altogether three different computer models were created to consider the single steps of the consolidation strategy as follows:

- Model A: Original system with joints, without shear walls and without TMCS.
- Model B: System with additional shear walls and with some connected slabs.
- Model C: System with additional shear walls, with some connected slabs and with TMCS.

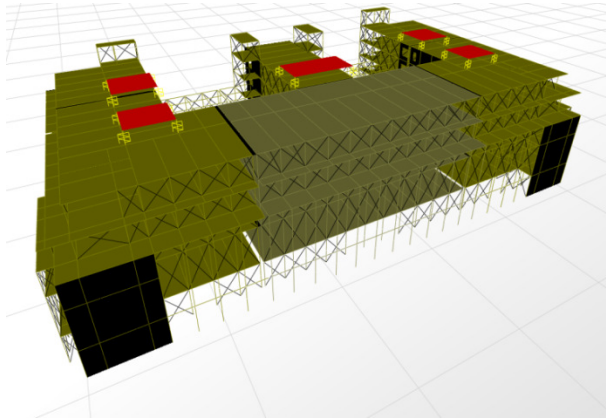


Figure 23. Computer model.

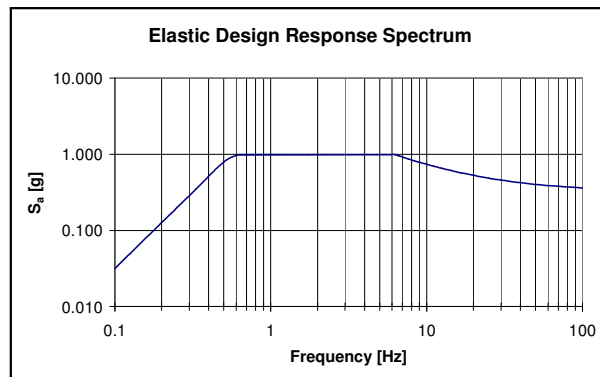


Figure 24. Design spectrum ($D = 5\%$).

After implementation of the measures the weight of the total structure is increased to about 38,800 tons. A plot of the Model C is shown in [Figure 23](#).

The elastic response spectrum (see [Figure 24](#)), which has to be taken into account, can be described as follows:

- Peak ground acceleration 0.36 g
- Spectral amplification factor: 2.75
- Resonance plateau with 0.99 g at 0.63–6.30 Hz

Several calculations (response spectrum analyses and time history analyses) were performed to define the optimal parameters for the TMCS. A TMCS—located on the roof top of different building segments—consisting of the following elements was chosen:

- 5 concrete blocks (each one has a mass of about 96 tons) / supported by sliding bearings.
- Each block is connected with spring elements to the roof in both horizontal directions.
- Damper elements are arranged.

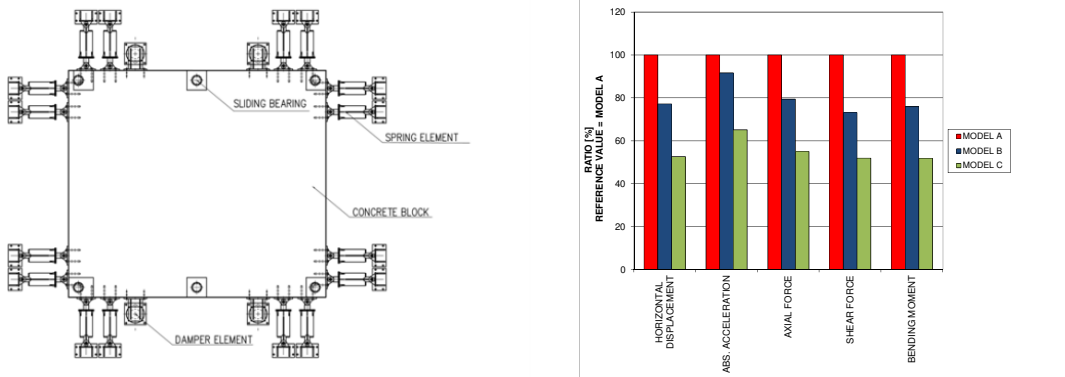


Figure 25. Left: principle of TMCS. Right: efficiency of TMCS.

A principle sketch of one block of the TMCS is presented in [Figure 25](#), left.

The results of the calculations show that the TMCS significantly reduces the top story displacements, interstory drifts, response accelerations and consequently induced internal stress responses due to earthquakes. In [Figure 25](#), right, the corresponding efficiency of the proposed measures are shown, by comparing some important values.

The first step (Model B = additional shear walls and connected floors) lead only to an improvement of about 10 to 20%. This was not sufficient in regard to the demands of the important structure.

The additional implementation of the TMCS (Model C) was required to achieve an improvement of more than 35%.

5.3. Manufacturing of devices. The required devices (spring elements and Viscodamper[®] from GERB Vibration Control Systems) are developed and manufactured. Due to the uncertainties of the conventional stiffening of the building structure by adding the new shear walls and the connection of some slabs, a special kind of spring element was required. It is possible to use different kind of springs inside the spring element. Thus, it is possible to adjust the stiffness of the element very easily. The spring elements (see [Figure 26](#)) are tested in axial direction to check the stiffness of the elements.

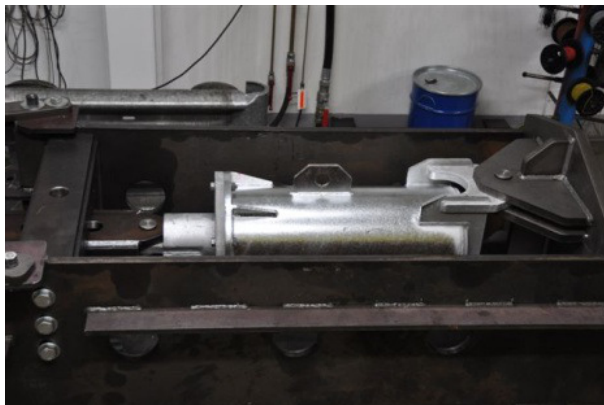


Figure 26. Spring element in test rig.



Figure 27. Viscodamper® in test rig.



Figure 28. New shear wall.

The Viscodamper® units (see [Figure 27](#)) were tested to verify the required damping resistance values. Due to the very high seismic excitation, a suitable damper had to be developed and tested.

5.4. Installation works and in situ tests. At the moment the installation process is nearly completed. The Romanian construction company started with the implementation of the new shear walls ([Figure 28](#)) and the connection of the slabs.

Afterwards the five concrete blocks were poured and the required embedded parts for the connection between spring element / damper element and the roof were fabricated and installed. As a next step one of the blocks was equipped with spring and damper devices (see [Figure 29](#)).

Prior to the final installation of all spring elements, vibration measurements were performed and are currently being analyzed. The objective of these initial ambient vibration measurements is to verify the calculated resulting natural frequencies of the building structure after the implementation of the shear walls, connection of the slabs and arrangement of the masses of the TMCS. Additionally, also the specific



Figure 29. TMCS at roof of building.

parameters of the TMCS in their current setup were determined. In a next step the final specification of the required spring stiffness and damping properties will be derived and the TMCS will be adjusted accordingly to complete the installation process (scheduled for summer 2011).

6. Conclusion and outlook

Experimental shaking table tests and theoretical investigations have shown that the application of passive control systems can lead to a significant reduction of the dynamic response to seismic loading. While the experimental investigations showed that a reduction can be achieved for several examined time histories, theoretical analyses showed that the effectiveness of these systems is strongly dependent on the specification of the guiding TMCS parameters such as effective mass, tuning frequency and internal damping ratio.

To achieve the highest effectiveness possible for tuned mass control systems (TMCS) for earthquake protection that are installed at an elevated bridge structure in Guadalajara, Mexico, and a building in Bucharest, Romania, theoretical approaches have been introduced and several numerical studies have been done to verify the optimum specification of the control system. Depending on the free-vibration participation of the structural response, the optimum reduction can be achieved with the Den Hartog Criteria or with recommended higher internal damping ratios of the TMCS.

Practical considerations showed that a higher internal damping leads to a more robust specification in terms of varying structural stiffness and inherent damping. Additional numerical calculations of the bridge and the building discussed here, verified the chosen TMCS parameters.

Both TMCS devices that are introduced in this contribution have been installed. In-situ tests are currently being performed to determine structural and TMCS parameters. The dynamic loading of the bridge structure due to traffic and the design of the TMCS allow a direct verification of the effectiveness of the system, once the test data have been analyzed. The test results of the TMCS for the RC structure/masonry wall building and of the building itself will be used for model updating to perform a final theoretical analysis.

References

- [Ayorinde and Warburton 1980] E. O. Ayorinde and G. B. Warburton, “Minimizing structural vibrations with absorbers”, *Earthquake Eng. Struct. Dyn.* **8** (1980), 219–236.
- [Den Hartog 1956] J. P. Den Hartog, *Mechanical vibrations*, 4th ed., McGraw-Hill, New York, 1956.
- [Rakicevic et al. 2006] Z. Rakicevic, A. Zlatevska, D. Jurukovski, and P. Nawrotzki, “Analytical estimation of the effectiveness of tuned mass control systems using shaking table experiments”, in *4th World Conference on Structural Control and Monitoring*, San Diego, 2006.
- [Sadek et al. 1997] F. Sadek, B. Mohraz, A. W. Taylor, and R. M. Chung, “A method of estimating the parameters of tuned mass dampers for seismic applications”, *Earthquake Eng. Struct. Dyn.* **26** (1997), 617–635.
- [Villaverde and Koyama 1993] R. Villaverde and L. A. Koyama, “Damped resonant appendages to increase inherent damping in buildings”, *Earthquake Eng. Struct. Dyn.* **22** (1993), 491–507.

Received 31 Mar 2011. Revised 27 Jun 2011. Accepted 1 Sep 2011.

CHRISTIAN MEINHARDT: christian.meinhardt@gerb.de

GERB Schwingungsisolierungen GmbH & Co. KG, Roedernallee 174-176, D-13407 Berlin Germany

DANIEL SIEPE: daniel.siepe@gerb.de

GERB Engineering GmbH, Ruhrallee 311, D-45136 Essen, Germany

PETER NAWROTZKI: peter.nawrotzki@gerb.de

GERB Schwingungsisolierungen GmbH & Co. KG, Roedernallee 174-176, D-13407 Berlin Germany

REPORT ON THE EFFECTS OF SEISMIC ISOLATION METHODS FROM THE 2011 TOHOKU–PACIFIC EARTHQUAKE

YUTAKA NAKAMURA, TETSUYA HANZAWA, MASANOBU HASEBE,
KEIICHI OKADA, MIKA KANEKO AND MASAACKI SARUTA

The earthquake that occurred on March 11, 2011 off the Pacific Coast of Tohoku caused devastating damage to the northeast Pacific coast region of Japan. We discuss the response to this earthquake of three buildings in Shimizu Corporation’s Institute of Technology in Tokyo, each with a different type of seismic isolation, and that of a test building for seismic isolation jointly built by Shimizu Corporation and Tohoku University on the Sendai campus in Miyagi prefecture, which was near the earthquake’s epicenter. The effects of seismic isolation methods were verified through the observed earthquake responses of the four buildings. In each of the three seismic isolated buildings at the Institute, the observed accelerations on the floors were reduced to about half compared to those on the ground. In the test seismic isolated building in Tohoku University, the observed accelerations on the roof were reduced to about one third compared to those in an adjacent conventional seismically designed building.

1. Introduction

The number of seismic isolated buildings has increased in Japan since the 1995 Kobe Earthquake, and the total number of seismic isolated buildings is said to exceed 2,500, excluding individual seismic isolated houses. In the early implementation of seismic isolation methods, most of the buildings employed ordinary rubber bearings and dampers that were simply installed underneath a structure. The effects of such ordinary seismic isolation methods have been already confirmed through the observed records of past earthquakes in Japan.

Recently, various kinds of new seismic isolation methods have been developed and applied to actual buildings. In Shimizu Corporation’s Institute of Technology in Tokyo, there are three different types of seismic isolated buildings, each of which employs a newly developed seismic isolation method: column-top seismic isolation, core-suspended isolation, or partially floating seismic isolation. Each seismic isolated building was installed with earthquake-sensing devices to verify the effects of the applied seismic isolation method.

In addition, Shimizu Corporation and Tohoku University jointly built two three-story reinforced concrete buildings next to each other in the Sendai campus (in Miyagi prefecture): one is a conventional seismically designed building, and the other is a seismic isolated building with six high-damping rubber bearings installed underneath the structure. Although the applied seismic isolation method was an ordinary method, the test buildings stood near the epicenter of the earthquake that occurred at 14:46 on March 11, 2011 off the Pacific coast of Tohoku — hereafter called the 2011 Tohoku–Pacific Earthquake.

Keywords: 2011 Tohoku–Pacific Earthquake, Pacific coast, seismic isolated building, rubber bearing, seismic observation, earthquake response.

(See figure on the right.) Thus it was possible to verify the effects of seismic isolation by directly comparing the earthquake responses in the seismic isolated building with those in the adjacent conventional seismically designed building.

This report describes the effects of the applied seismic isolation methods that were verified through the observed earthquake responses of the above-mentioned four seismic isolated buildings subjected to the 2011 Tohoku–Pacific Earthquake.

2. Overview of the earthquake

The 2011 Tohoku–Pacific Earthquake was an interplate earthquake, occurring on the boundary between the Pacific plate and the Continental plate. Its magnitude was reported as being 9.0, the highest ever recorded in Japan. The scale of this event ranks fourth in the world. The fault plane extended to about 500 km in a North–South direction (length) and about 200 km in an East–West direction (width).

The huge scale of the 2011 Tohoku–Pacific Earthquake produced strong shaking across a broad area. The area with seismic intensity larger than 6– extended to 450 km, and the area with seismic intensity larger than 6+ extended to 300 km. The area with high seismic intensity due to this earthquake was much broader than those in recent destructive inland earthquakes, as shown in [Figure 1](#).

The observed ground motions had a definite feature of a long duration because of the large scale of the fault plane, compared to those of some previous destructive earthquakes, as is shown in [Figure 2](#). The

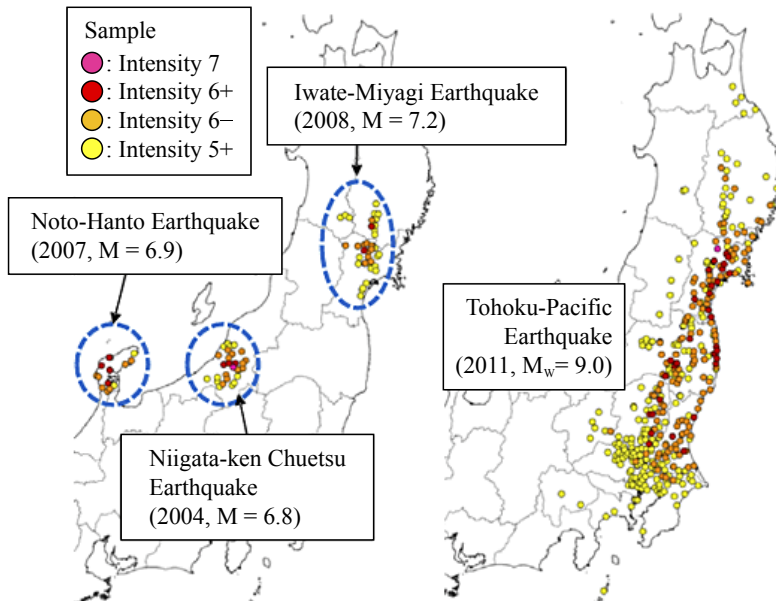
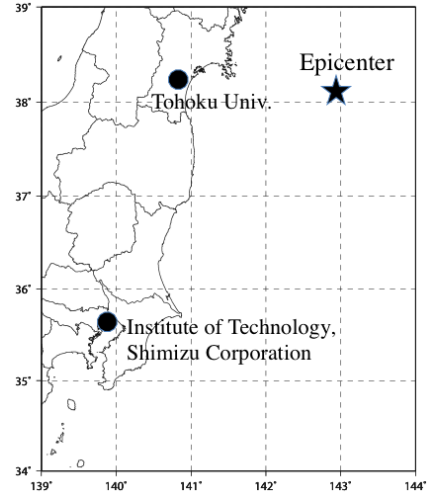


Figure 1. The spatial distribution of the areas with seismic intensity larger than 5+ (in comparison with recent destructive inland earthquakes).



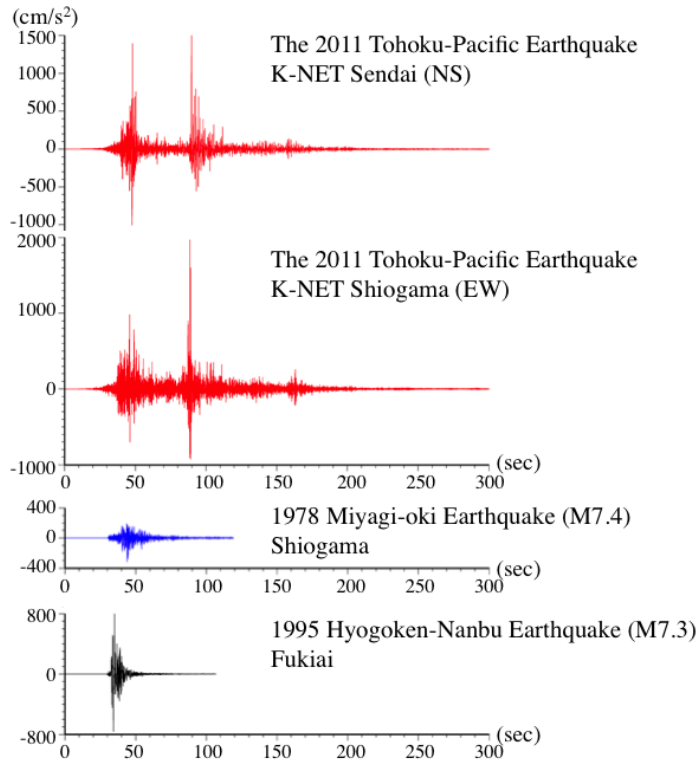


Figure 2. Comparison of observed records at K-NET Sendai and K-NET Shiogama of the 2011 Tohoku-Pacific Earthquake with those from previous destructive earthquakes.

observed ground motions and the response acceleration spectra at Tohoku University and at the institute are shown in [Figure 3](#).

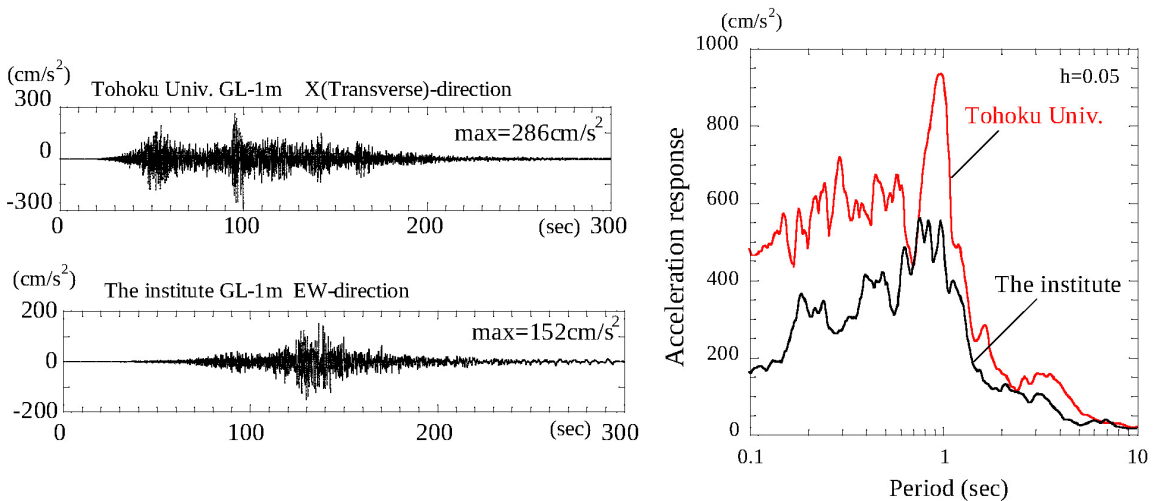


Figure 3. Observed ground motions and response spectra.

3. Overview of the four seismic isolated buildings

Three different types of seismic isolated buildings stand in the grounds of the Shimizu Corporation's Institute of Technology in Tokyo. Each of the three buildings employs a different seismic isolation method, and is installed with earthquake-sensing devices. In addition, Shimizu Corporation and Tohoku University jointly built a test building for seismic isolation within the Sendai campus (in Miyagi prefecture), and have carried out seismographic observations since 1986. The overview of the four seismic isolated buildings is described below.

3.1. The Main Building: a column-top seismic isolation system. The Main Building in the institute is a 6-story, long-span, seismic isolated structure which utilizes a column-top seismic isolation (CTSI) system [Nakamura et al. 2009]. Table 1 gives the design details of the building. The building uses a large-scale trussed cage structure, the upper part of which is supported on six isolators on independent

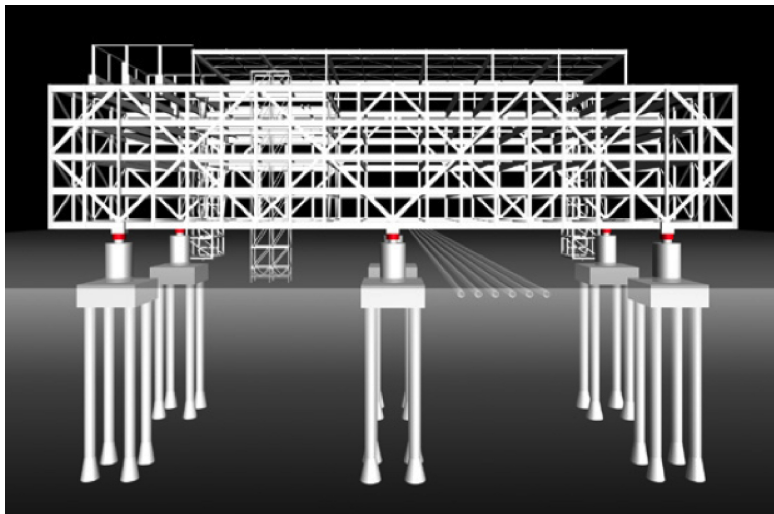


Figure 4. The Main Building (top) and diagram of its structural system.



Figure 5. Seismic isolators (lead rubber bearings) on top of first-floor pilotis in the Main Building.

columns, creating an expansive area at ground level, as shown in Figures 4 and 5. Mega-truss frames and rigid frames with bracings are used to provide a large free office space of $80\text{ m} \times 40\text{ m}$. Four concrete piles support each isolated column, eliminating the need for footing girders underground.

The seismic isolators are lead rubber bearings of 1,000 mm or 1,100 mm in diameter, as shown in Figure 5, left. Because of the soft soil conditions of the site, the natural period of the seismic isolated structure is designed to be 4.0 s at 200% shear strain level of the isolator. The maximum vertical stress for dead and live loads is an average of 14.1 N/mm^2 .

3.2. The Safety and Security Center: a core-suspended isolation system. A core-suspended isolation (CSI) system consists of a reinforced concrete core on top of which a seismic isolation mechanism composed of a double layer of inclined rubber bearings is installed to create a pendulum isolation mechanism [Nakamura et al. 2011]. The Safety and Security Center, shown in Figure 6, is the first building to utilize the CSI system. Table 2 gives the design details of the building.

Floor area	Total: 9634 m^2 , 2nd–5th floors: 1600 m^2 ($20\text{ m} \times 80\text{ m}$)
Height	Total: 27.6 m; 1st story: 6.8 m; 2nd–5th stories: 4.0 m; penthouse: 4.8 m
Structure	Steel frames and reinforced concrete slabs, total weight: 7000 ton Six lead rubber bearings (LRBs) in total, $G = 0.39\text{ MPa}$
Rubber bearings	Three LRBs: diameter: 1000 mm, rubber layers: $6.7\text{ mm} \times 30$ $S1 = 37.3$, $S2 = 5.0$, horizontal stiffness = 20400 kN/m Three LRBs: diameter: 1100 mm, rubber layers: $7.4\text{ mm} \times 27$ $S1 = 37.2$, $S2 = 5.5$, horizontal stiffness = 24800 kN/m Maximum deformation of performance: 450 mm
First mode period (design value)	4.0 s at 200% shear strain level

Table 1. Details of the Main Building.

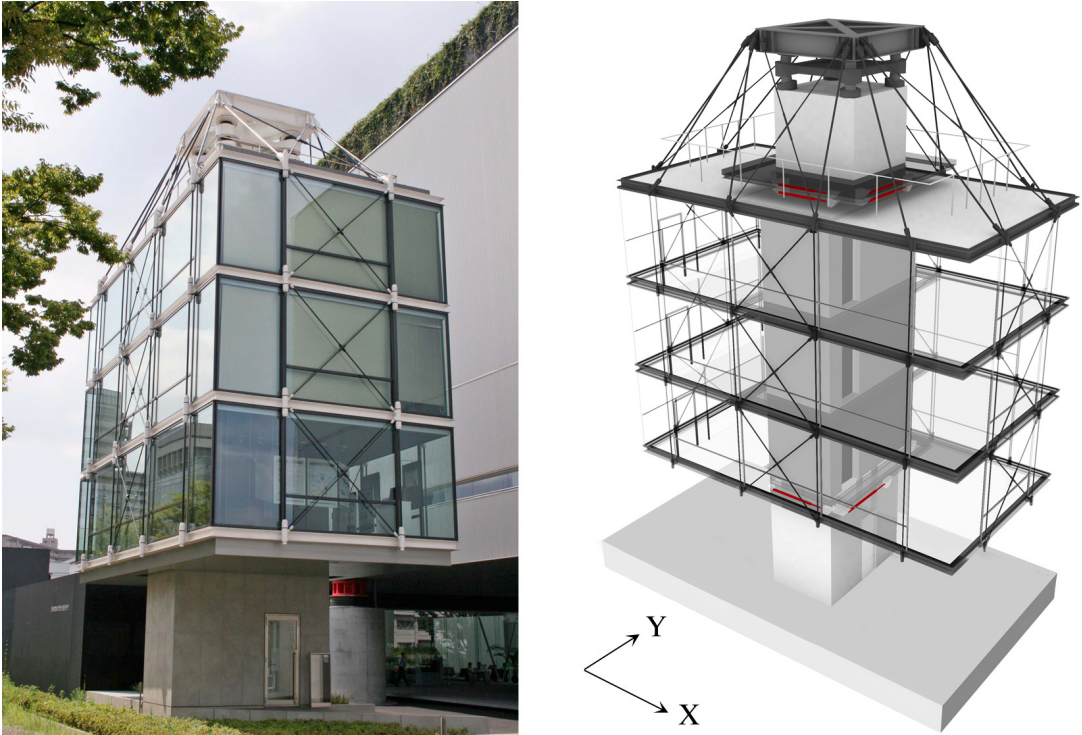


Figure 6. The Safety and Security Center and diagram of its structural system.

The pendulum seismic isolation mechanism for the building consists of two layers each of four inclined rubber bearings, installed at the top of a reinforced concrete core, from which three floors of office structure are suspended by high-strength steel rods, as shown in Figures 6 and 7. Fluid dampers are placed between the core shaft and the suspended office structure to control the motion of the building. The first mode period is designed to be around 5 s in both the X - and Y -directions.

Floor area	Total: 213.65 m ² ; 1st floor: 9.05 m ² ; 2nd–4th floors: 66.15 m ² ; penthouse: 6.15 m ²
Height	Total: 18.75 m; 1st story: 4.15 m; 2nd–4th stories: 3.0 m
Core shaft	Reinforced concrete wall 200 mm thick; 400 mm clearance joint
Suspended structure	Total weight: 180 ton; steel rod column 42 mm diameter
Rubber bearings	Two layers each of four inclined rubber bearings, diameter: 300 mm S1 = 35.7, S2 = 3.11, G = 0.29 MPa, horizontal stiffness = 215 kN/m Maximum deformation of performance: 155 mm
Tilt angles	Lower layer: $\phi_1 = 9.9$ degrees; upper layer: $\phi_2 = 6.6$ degrees
First mode period (design value)	5.08 s in X -dir, 5.14 s in Y -dir.

Table 2. Details of the Safety and Security Center.

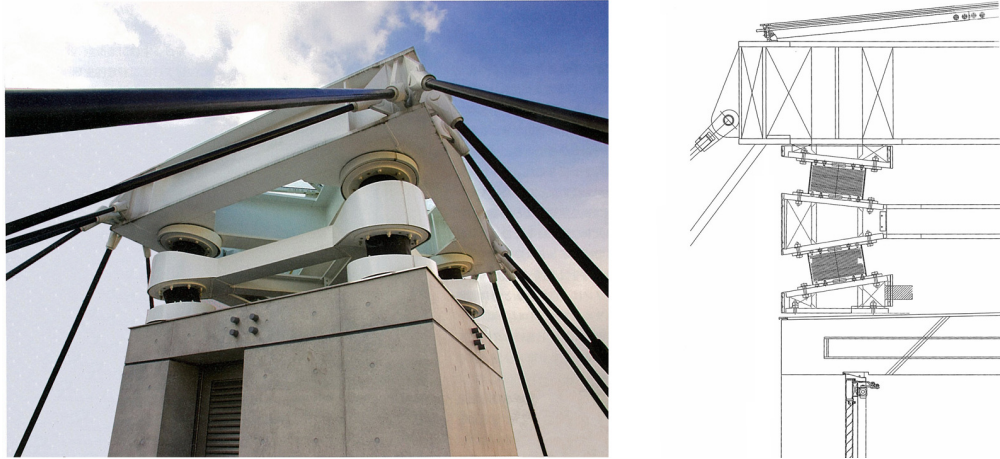


Figure 7. The core-suspended isolation system, comprising two layers, each of four inclined rubber bearings.

3.3. The Wind Tunnel Testing Laboratory: a partially floating seismic isolation system. A partially floating seismic isolation (PFSI) system utilizes buoyant floatation forces to partially support the gravity weight of the protected structure, along with rubber bearings [Saruta et al. 2007]. In addition, the system utilizes a porous media attached to sides of the basin as a means of damping the structural motion.

The Wind Tunnel Testing Laboratory, shown in Figures 8 and 9, is the first building to utilize the PFSI



Figure 8. The Wind Tunnel Testing Laboratory.

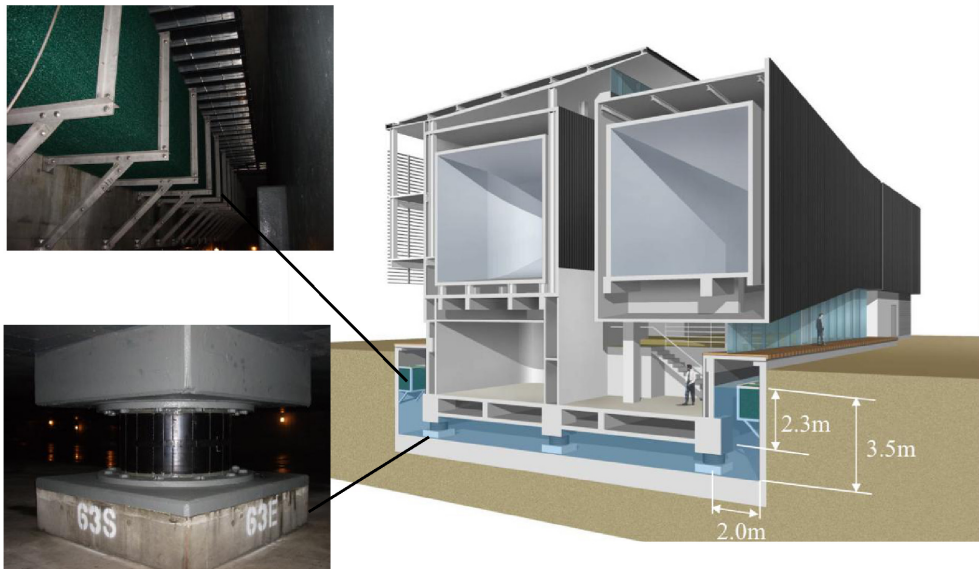


Figure 9. A cross section of and the structural system of the partially floating seismic isolation system.

system. The basement, as shown in Figure 9, is of 2.3 m draft, and half of the weight of the structure is supported by buoyancy. Table 3 gives the design details of the building. The natural period of the seismic isolated structure is designed to be 4.1 s.

Floor area	Total: 1253 m ² (3 stories above the ground, 1 underground floor)
Height	Total: 17.2 m (12.7 m above the ground, 4.5 m underground)
Structure	Reinforced concrete (partly, steel structure)
Weight	Total weight: 2900 ton
Draft of structure	2.3 m (Half of weight is supported by buoyancy) 14 high-damping rubber bearings (HDRBs) in total, $G = 0.39$ MPa, covered by lining rubber including steel flange plates (Figure 9, lower left)
Rubber bearings	7 HDRBs: diameter: 650 mm, rubber layers: 4.4 mm \times 45 $S1 = 36.1$, $S2 = 3.28$, horizontal stiffness = 3230 kN/m maximum deformation of performance: 461 mm 7 HDRBs: diameter: 700 mm, rubber layers: 4.7 mm \times 43 $S1 = 36.4$, $S2 = 3.46$, horizontal stiffness = 3670 kN/m maximum deformation of performance: 485 mm
Reservoir	Area: 830 m ² , depth: 4.5 m, volume of water: 1540 ton
First mode period (design value)	4.1 s

Table 3. Details of the Wind Tunnel Testing Laboratory.

3.4. The test buildings in Tohoku University. Shimizu Corporation and Tohoku University jointly built two adjacent three-story reinforced concrete buildings in the Sendai campus (Miyagi prefecture) as shown in Figure 10: one is a conventional seismically designed building, and the other is a seismic isolated building with six high-damping rubber bearings installed underneath the structure [Saruta et al. 1989]. Table 4 gives the design details of the test buildings.



Figure 10. Test buildings at Tohoku University. Left: conventional seismically designed building; right: seismic isolated building.

Floor area	Each building	Total: 180 m ² ; 1st–3rd floors: 60 m ² (6 m × 10 m)
Height	Each building	Total: 9.9 m; 1st–3rd stories: 3.3 m
Structure	Each building	Reinforced concrete
Weight	Conventional building	Total weight: 176 ton
	Seismic isolated building	Total weight: 255 ton
Rubber bearings	Seismic isolated building	6 HDRBs: diameter: 435 mm rubber layers: 6.7 mm × 18 S1 = 16.2, S2 = 3.6 horizontal stiffness = 627 kN/m
First mode period (design value)	Conventional building	0.3 s
	Seismic isolated building	1.6 s (at deformation of bearing = 8 cm)

Table 4. Details of the test buildings in Tohoku University.

4. Observed earthquake responses of the four seismic isolated buildings

A structural health monitoring (SHM) system was implemented into the four seismic isolated buildings to detect their seismic performance [Okada et al. 2009]. The effects of applied seismic isolation methods were verified through the observed earthquake responses of the four seismic isolated buildings subjected to the 2011 Tohoku–Pacific Earthquake.

4.1. The Main Building. Figure 11 shows the maximum acceleration responses of the Main Building when subjected to the 2011 Tohoku–Pacific Earthquake. Observed acceleration waves on the ground and 6th floors are shown in Figure 12. The maximum accelerations on the floors of the seismic isolated structure were story-wise almost uniform, and reduced to about half compared to those on the ground.

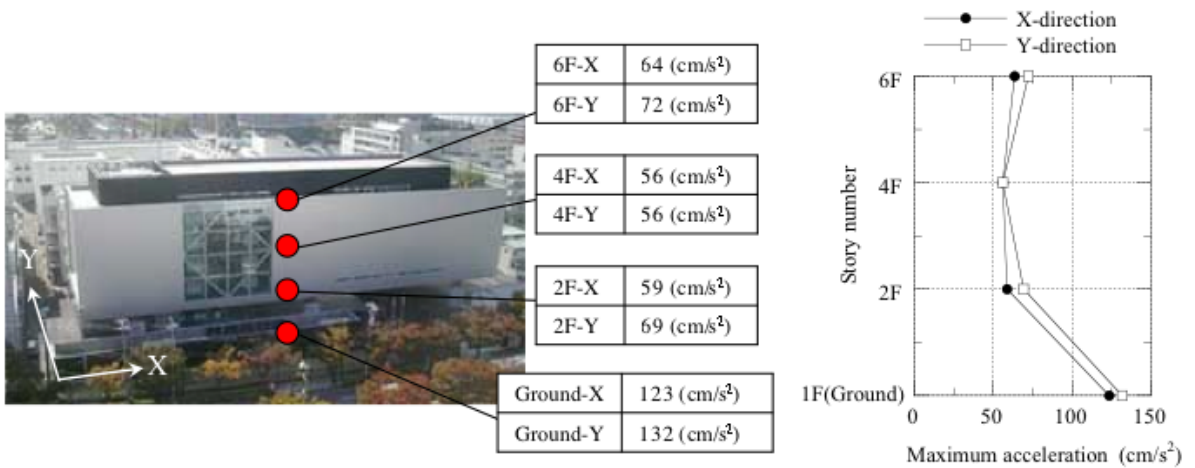


Figure 11. Maximum responses of the Main Building.

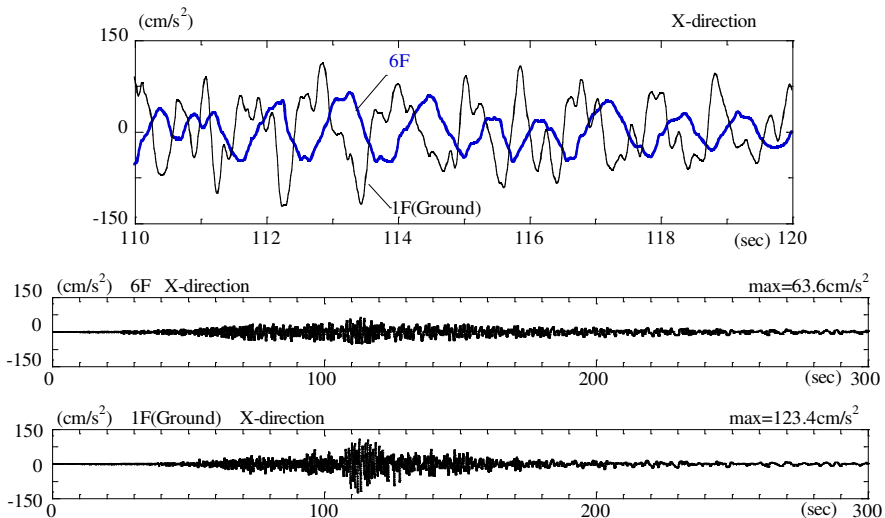


Figure 12. Observed acceleration waves on the ground and on the 6th floor of the Main Building.

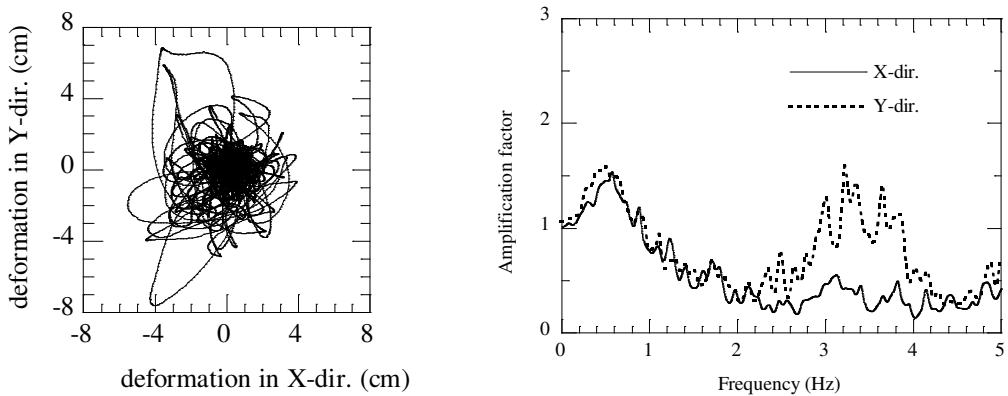


Figure 13. Main Building observations: locus of the horizontal deformation of an LRB (left) and transfer function of the acceleration (6th floor relative to ground floor).

The locus of the horizontal deformation of a lead rubber bearing is shown in Figure 13, left. The maximum displacement of the rubber bearing was 8.6 cm, which was much less than the maximum deformation of performance, which was 45 cm.

Figure 13, right, shows the transfer functions of the observed accelerations on the 6th floor relative to those on the ground. The transfer function indicates that the fundamental natural period of the seismic isolated structure was about 2 s, which is shorter than the designed first-mode period.

4.2. The Safety and Security Center. Figure 14 shows the maximum acceleration responses of the Safety and Security Center when subjected to the 2011 Tohoku–Pacific Earthquake. Though the acceleration responses were amplified at the top of the core structure, the CSI system reduced them and the

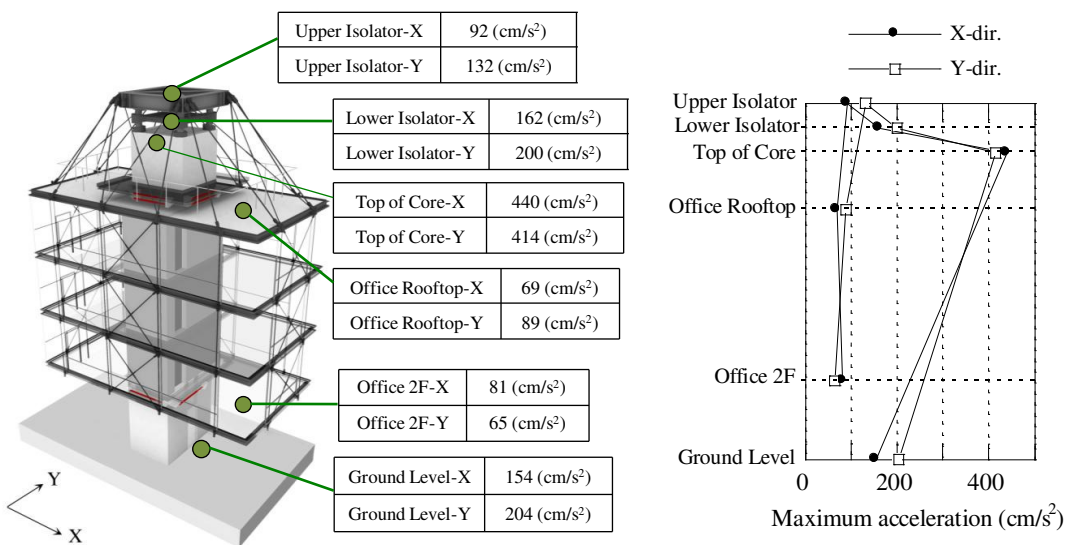


Figure 14. Maximum responses of the Safety and Security Center.

maximum accelerations on the floors in the hung structure were reduced to about half in the X-direction, and to about one third in the Y-direction, compared to those on the ground, respectively. Observed acceleration waves on the ground level and on the 2nd floor in the office are shown in Figure 15.

Figure 16, left, shows the locus of the horizontal relative displacement between the core structure and the 2nd floor in the office. The maximum relative displacement was about 8 cm, much less than the clearance of 40 cm. Figure 16, right, shows the transfer functions of the observed accelerations in

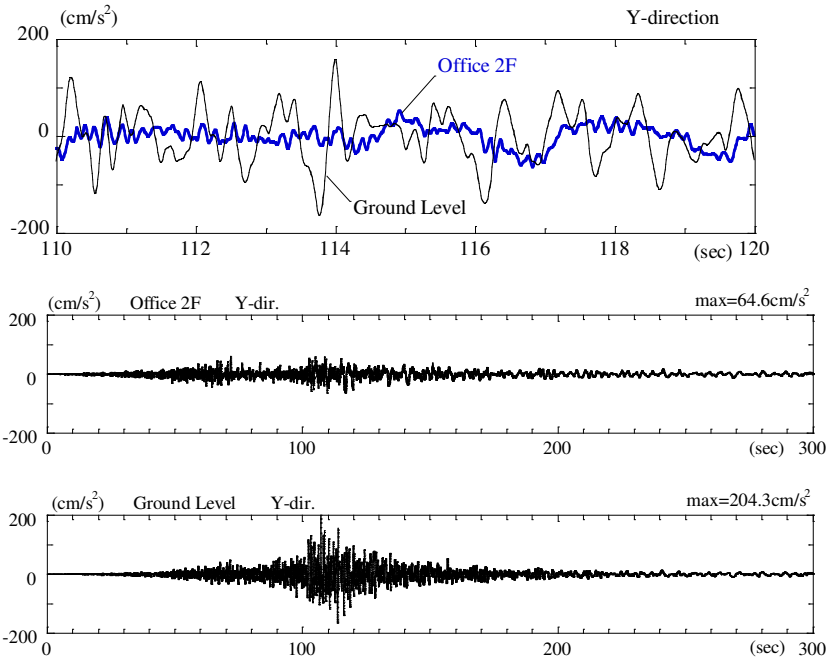


Figure 15. Observed acceleration waves on the ground level and in an office on the 2nd floor of the Safety and Security Center.

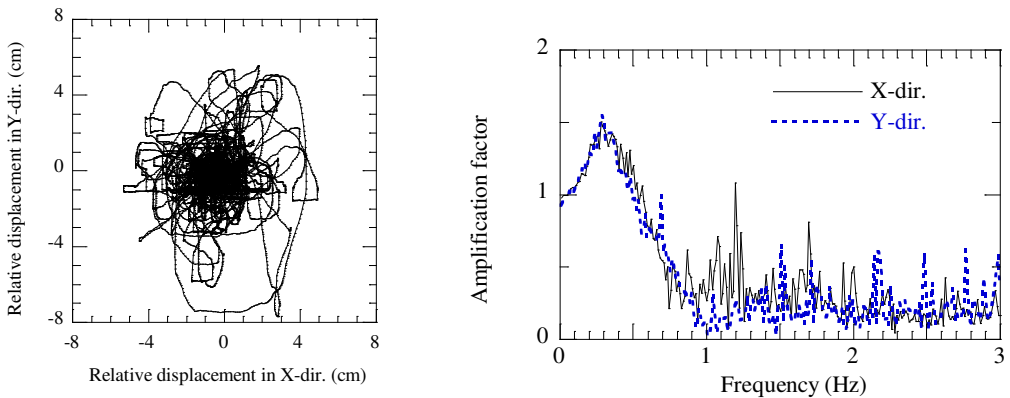


Figure 16. Safety and Security Center: Relative displacement between a 2nd floor office and the core structure (left), and acceleration transfer function for 2nd floor office on relative to ground level.

the 2nd floor office relative to those on the ground level, which indicate that the fundamental natural period of the hung structure was 3.6 s (0.28 Hz) in the X -direction, and 3.4 s (0.29 Hz) in the Y -direction, respectively. These values are shorter than the designed first-mode periods.

4.3. The Wind Tunnel Testing Laboratory. Figure 17 shows the maximum acceleration responses of the Wind Tunnel Testing Laboratory when subjected to the 2011 Tohoku–Pacific Earthquake. On the roof, the acceleration response in the Y -direction was amplified because the top part of the building is partially made of steel. The maximum accelerations in the 1st basement level and on the 2nd floor of the structure were reduced to about half in both directions, compared to those at the base of the pit.

Figure 18, left, plots the locus of the horizontal deformation of a rubber bearing. The maximum displacement of the rubber bearing was 7.8 cm, much less than the maximum deformation of performance,

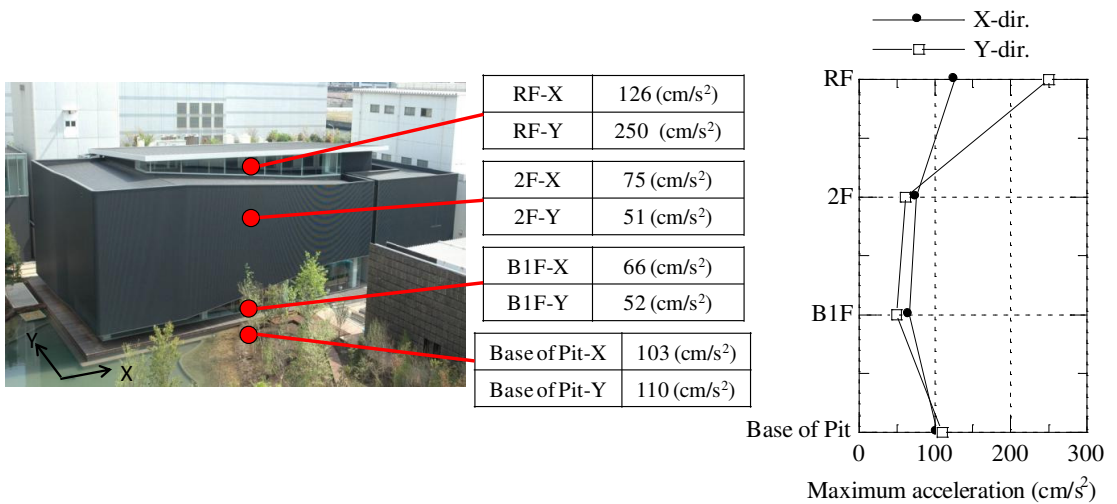


Figure 17. Maximum responses of the Wind Tunnel Testing Laboratory.

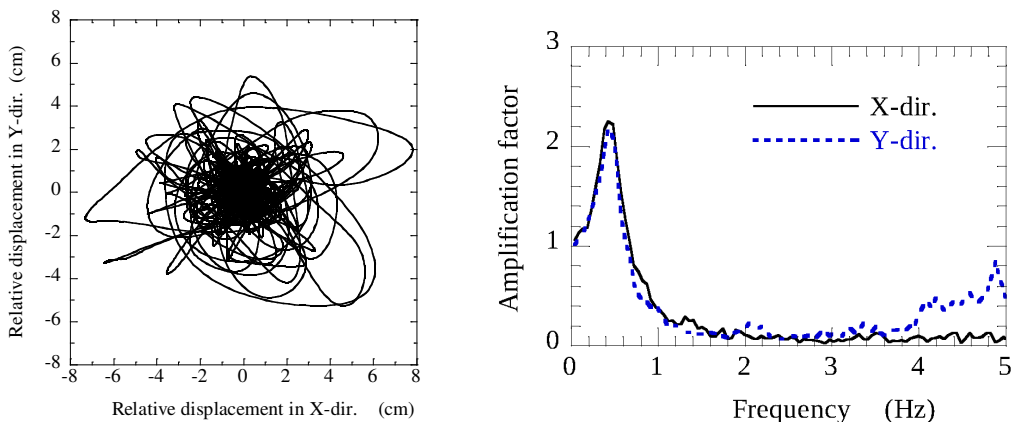


Figure 18. Wind Tunnel Testing Laboratory: locus of the horizontal deformation of a rubber bearing (left) and acceleration Transfer functions for 1st basement level versus base of the pit.

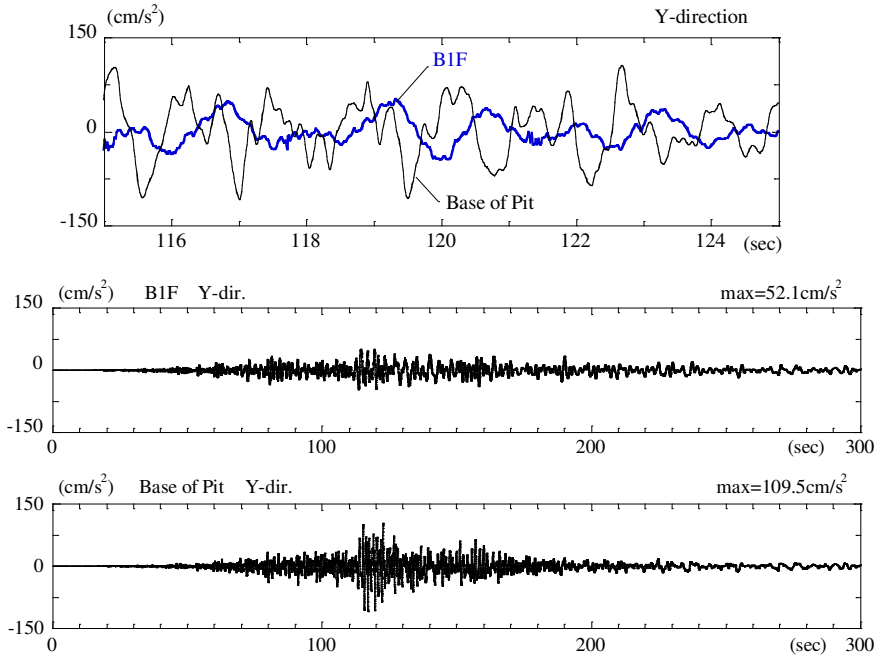


Figure 19. Observed acceleration waves at the base of the pit and on the 1st basement level in the Wind Tunnel Testing Laboratory.

which was 46 cm. [Figure 18](#), right, shows the transfer function of the observed accelerations on the 1st basement level to those at the base of the pit, which indicates that the fundamental natural period of the isolated structure was 2 s (0.5 Hz). This value is shorter than the designed first-mode period. The observed acceleration waves at the base of the pit and on the 1st basement level are shown in [Figure 19](#).

4.4. The test buildings in Tohoku University. Maximum acceleration responses of the two test buildings when subjected to the 2011 Tohoku–Pacific Earthquake are shown in [Figures 20](#) and [21](#). In the seismic

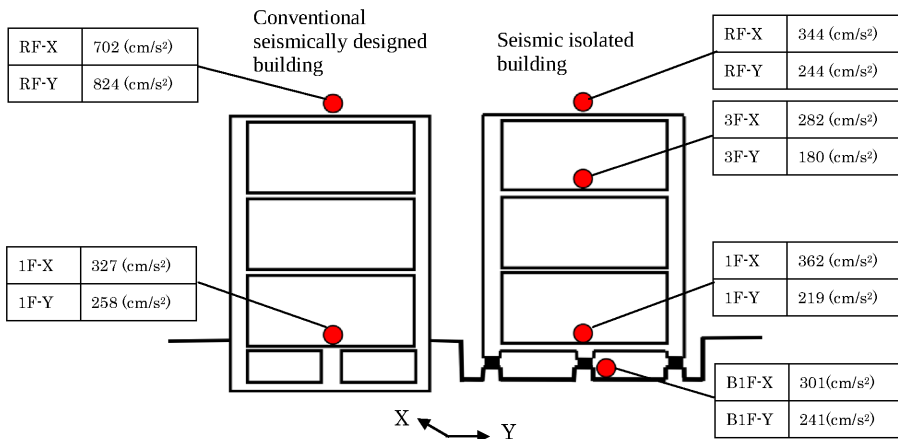


Figure 20. Maximum responses of the test buildings in Tohoku University.

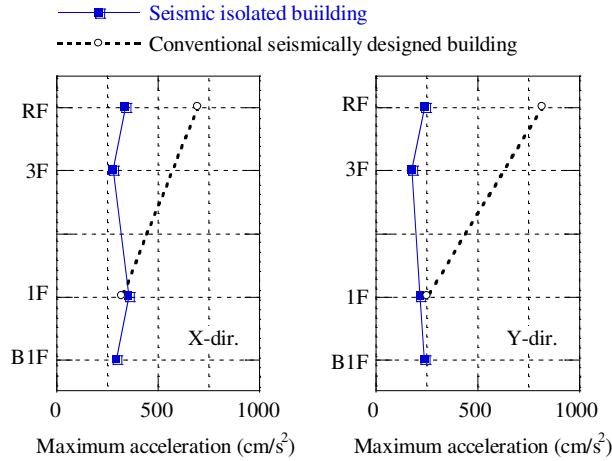


Figure 21. Maximum responses of the test buildings in Tohoku University (continued).

isolated building, the observed accelerations on the roof were reduced to about half in the X-direction, and to about one third in the Y-direction, respectively, compared to those in the adjacent conventional seismically designed building.

Figures 22 and 23 show the observed acceleration waves in the test buildings. In Figure 23, the observed acceleration wave on the roof of the seismic isolated building is expanded and overlaid onto that of the conventional seismically designed building, clearly demonstrating the differences in the earthquake responses of the two test buildings.

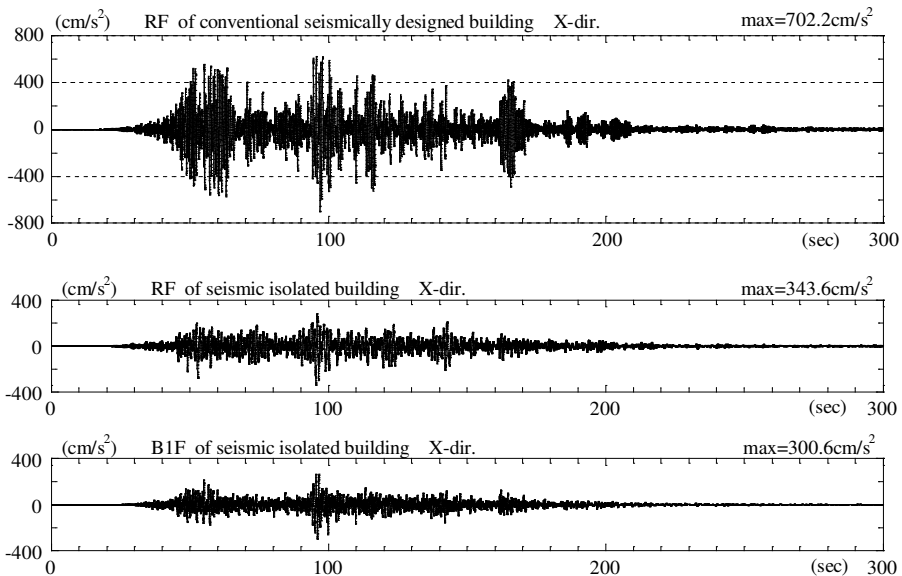


Figure 22. Observed acceleration waves in the conventional seismically designed building (RF) and in the seismic isolated building (1st basement level and RF).

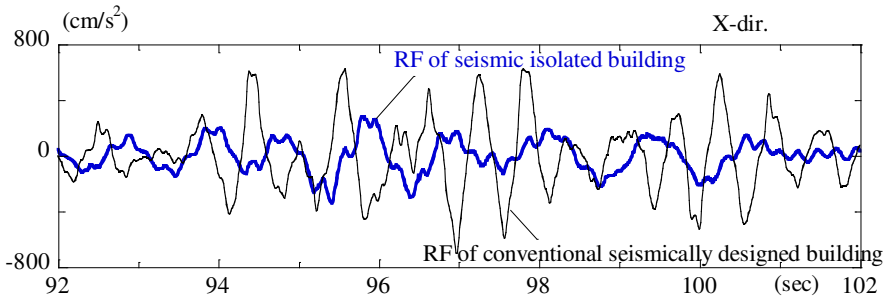


Figure 23. Observed acceleration waves on the RF in the two test buildings in Tohoku University.

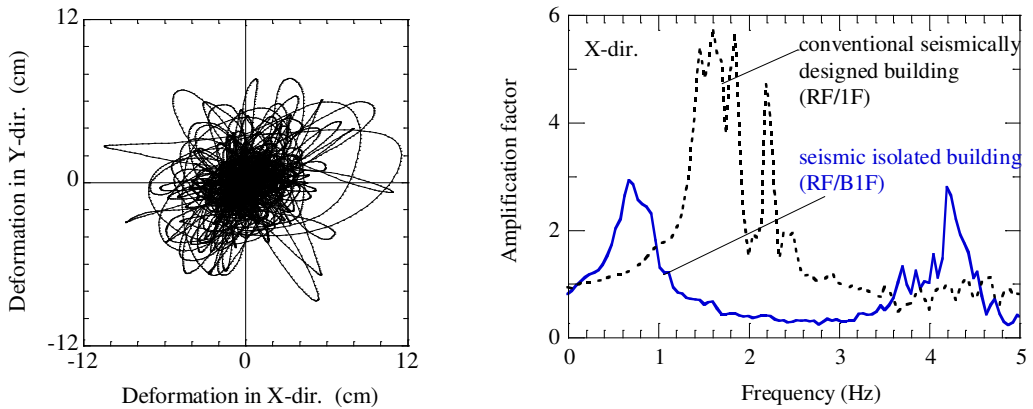


Figure 24. Left: locus of the horizontal deformation of the rubber bearing of the seismic isolated building in Tohoku University. Right: transfer functions of the observed accelerations (RF / 1F, RF/B1F) of the test buildings in Tohoku University.

The locus of the horizontal deformation of a rubber bearing is shown in [Figure 24](#), left. The maximum displacement of the rubber bearing was 11.5 cm, which was less than the maximum deformation of performance, which was 36 cm.

[Figure 24](#), right, shows the transfer function of the observed accelerations on the roof to the 1st basement of the seismic isolated building, along with the one of the conventional seismically designed building. The fundamental natural period of the seismic isolated building was 1.6 s (0.6 Hz) in the X-direction, while that of the conventional seismically designed building was 0.6 s (1.6 Hz).

5. Vertical responses of the seismic isolated structures

The applied seismic isolation methods were installed with the intent of decreasing the horizontal earthquake responses of the structure, and have been proven to be quite effective in reducing the horizontal acceleration responses through the observed records of the 2011 Tohoku–Pacific Earthquake, as described above. Here, we discuss whether seismic isolation methods are also effective in reducing vertical responses.

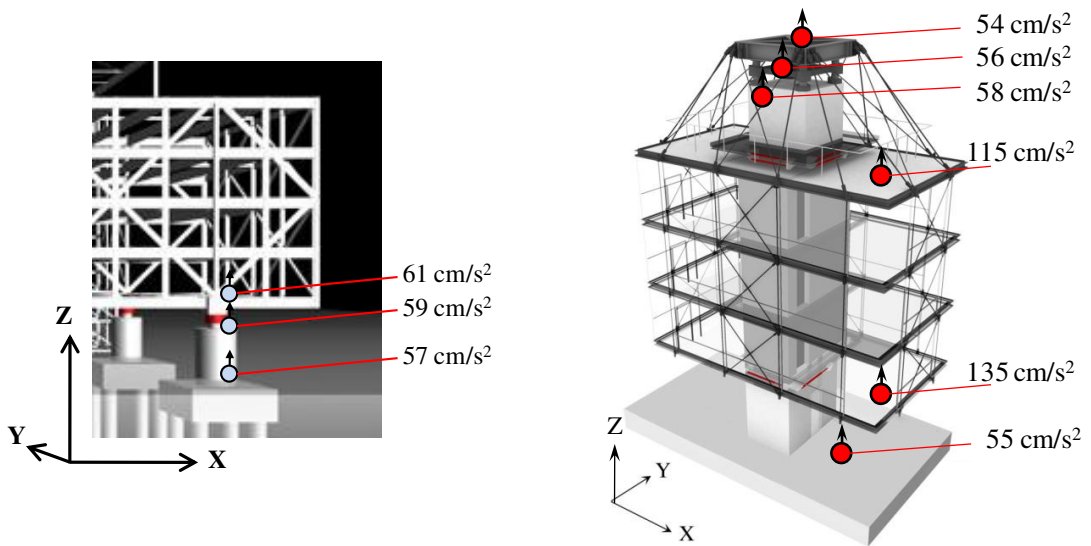


Figure 25. Maximum acceleration responses in the vertical direction of the Main Building (left) and of the Safety and Security Center (right).

Seismographs for the vertical direction were installed in the Main Building and the Safety and Security Center. Figure 25 shows the maximum acceleration responses in the vertical direction of the Main Building and of the Safety and Security Center. In the Main Building, as shown in Figure 25, left, the value of the maximum acceleration above the isolator was almost same as that below the isolator. In the Safety and Security Center, as shown in Figure 25, right, the values of the maximum acceleration response were almost constant from the ground level to the top of the core structure, while those for the hung office were even amplified to two to three times as much as that on the ground level.

These results illustrate that seismic isolation methods are not effective in reducing the vertical responses of a structure. The amplification of the vertical responses in a building may need to be taken into consideration, especially in long-span structures and in hung structures.

6. Conclusions

The 2011 Tohoku–Pacific Earthquake that occurred on March 11, 2011 caused devastating damage to the northeast Pacific coast region of Japan. The magnitude was reported as being 9.0, the highest magnitude ever recorded in Japan. The huge scale of this earthquake produced strong shaking across a broad area. The observed ground motions had a definite feature of a long duration because of the large scale of the fault plane.

Three different types of seismic isolated buildings stand in the Shimizu Corporation’s Institute of Technology in Tokyo. Each of the three buildings employs a different seismic isolation method: the Main Building by column-top seismic isolation (CTSI) system, the Safety and Security Center by core-suspended isolation (CSI) system, and the Wind Tunnel Testing Laboratory by partially floating seismic isolation (PFSI) system. Shimizu Corporation and Tohoku University jointly built a test building for

seismic isolation in the Sendai campus (in Miyagi prefecture), which was near the epicenter of the 2011 Tohoku–Pacific Earthquake.

The effects of applied seismic isolation methods were verified through the observed earthquake responses of the four seismic isolated buildings subjected to the 2011 Tohoku–Pacific Earthquake. In each of the three seismic isolated buildings in the institute, the observed accelerations on the floors were reduced to about half compared to those on the ground. In the test seismic isolated building in Tohoku University, the observed accelerations on the roof were reduced to about one third compared to those in the adjacent conventional seismically designed building.

The observed vertical responses in the seismic isolated buildings illustrate that seismic isolation methods are not effective in reducing the vertical responses of the structure. The amplification of vertical responses in a building may need to be taken into consideration, especially in the long-span structures and in hung structures.

References

- [Nakamura et al. 2009] Y. Nakamura, T. Saito, and K. Tamura, “A seismic isolated long-span overhanging urban infrastructure”, *J. Disaster Res.* **4**:3 (2009), 192–198.
- [Nakamura et al. 2011] Y. Nakamura, M. Saruta, A. Wada, T. Takeuchi, S. Hikone, and T. Takahashi, “Development of the core-suspended isolation system”, *Earthquake Engin. Struct. Dyn.* **40** (2011), 429–447.
- [Okada et al. 2009] K. Okada, Y. Nakamura, and M. Saruta, “Application of earthquake early warning system to seismic-isolated buildings”, *J. Disaster Res.* **4**:4 (2009), 242–250.
- [Saruta et al. 1989] M. Saruta, H. Watanabe, and M. Izumi, “Proof test of base-isolated building using high damping rubber bearing”, pp. 631–636 in *Transactions of the 10th International Conference on Structural Mechanics in Reactor Technology* (Anaheim, CA, 1989), vol. K2, 1989.
- [Saruta et al. 2007] M. Saruta, T. Ohyama, T. Nozu, M. Hasebe, T. Hori, H. Tsuchiya, and N. Murota, “Application of a partially-floating seismic isolation system”, in *10th World Conference on Seismic Isolation, Energy Dissipation and Active Vibrations Control of Structures* (Istanbul, 2007), 2007.

Received 16 Jun 2011. Accepted 24 Aug 2011.

YUTAKA NAKAMURA: yutaka.nakamura@shimz.co.jp

Institute of Technology, Shimizu Corporation, 3-4-17, Etchujima Koto-ku, Tokyo 135-8530, Japan

TETSUYA HANZAWA: hanzawa_t@shimz.co.jp

Institute of Technology, Shimizu Corporation, 3-4-17, Etchujima Koto-ku, Tokyo 135-8530, Japan

MASANOBU HASEBE: hasebe_m@shimz.co.jp

Institute of Technology, Shimizu Corporation, 3-4-17, Etchujima Koto-ku, Tokyo 135-8530, Japan

KEIICHI OKADA: okka@shimz.co.jp

Institute of Technology, Shimizu Corporation, 3-4-17, Etchujima Koto-ku, Tokyo 135-8530, Japan

MIKA KANEKO: mika@shimz.co.jp

Institute of Technology, Shimizu Corporation, 3-4-17, Etchujima Koto-ku, Tokyo 135-8530, Japan

MASAOKI SARUTA: saruta@shimz.co.jp

Institute of Technology, Shimizu Corporation, 3-4-17, Etchujima Koto-ku, Tokyo 135-8530, Japan

AN EXPERIMENTAL MODEL OF BUCKLING RESTRAINED BRACES FOR MULTI-PERFORMANCE OPTIMUM DESIGN

NOEMI BONESSIO, GIUSEPPE LOMIENTO AND GIANMARIO BENZONI

This paper presents the formulation of an analytical model of buckling restrained braces (BRBs) and its implementation into a structural optimization procedure in order to design the protection system of an existing structure. The procedure, based on a multi-performance approach, provides the minimum cost design solution, through sizing and topology optimization of the BRBs, for the retrofit of an existing structure. An analytical formulation for the BRBs is developed in order to introduce an efficient characterization of these devices into the structural optimization procedure. The prediction provided by the proposed analytical model is compared with the results of an experimental test campaign and the bilinear model.

1. Introduction

Passive energy dissipators such as viscous-fluid dampers, viscous-elastic dampers, metallic ductile dampers and friction dampers are widely used to reduce the dynamic response of civil engineering structures due to seismic and wind loads. The effectiveness of the dampers depends on the capability to absorb the structural vibration energy and to dissipate it through their inherent hysteresis behavior in order to reduce structural damages [Soong and Dargush 1997]. Among these dissipating devices, buckling restrained braces (BRBs) have been developed and applied for the seismic protection of building structures since their hysteretic behavior could be kept stable for cyclic tensile and compressive loads and desirable yielding forces are easily obtained by sizing their inner steel core. In addition they offer consistent energy dissipation capability and easy manufacturing, installation and maintenance [Black et al. 2002; Kiggins and Uang 2006; Lopez and Sabelli 2004; Sabelli 2001; Sabelli et al. 2003; Wada et al. 1998]. The optimal mechanical characteristics of the dampers depend on the structural configuration in which they are located, on the performance level and on the entity of the applied horizontal loads. Sizing and topology optimization procedures can be efficiently used in order to determine their characteristics and their location in a generic structural scheme.

Recently, performance-based design is getting more importance, overcoming traditional prescriptive design methods towards full reliability-based design methodologies. The present paper uses performance-based design concepts and casts them into a multiple-objective optimization procedure. In many studies, mono- or multi-optimization tools have been applied to the structural design [Frangopol 1995; Breitung et al. 1998; Thoft-Christensen and Sorensen 1987; Fu and Frangopol 1990]. In particular, the structural optimization procedure developed in [Bonessio 2010] has been here specialized into a specific procedure to retrofit an existing structure with a BRB system. The procedure provides the minimum cost design

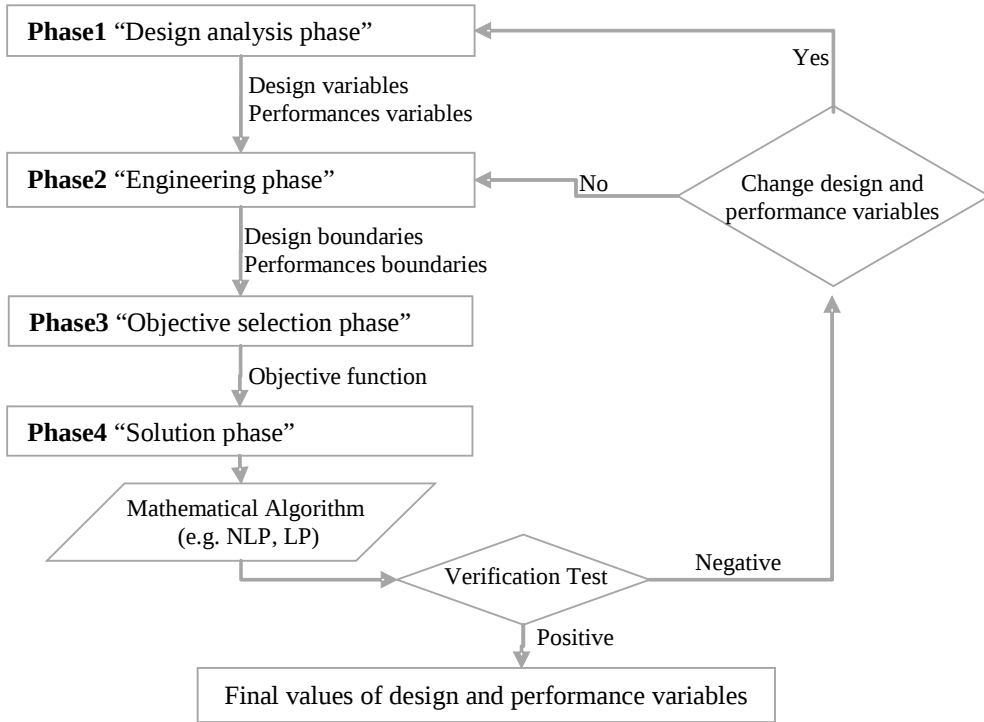
Keywords: buckling restrained braces, experimental tests, analytical model, performance-based design, structural optimization.

solution through the optimization of the braces characteristics and locations on the structure, while respecting several performance requirements. The proposed approach is based on a complete mechanical representation of the existing frame and the braces [Lomiento et al. 2010].

In many studies, the simple bilinear representation of the cyclic behavior of BRBs has shown to underestimate their actual capacity in the small deformation range [Tremblay et al. 2004; Fahnestock et al. 2004]. More accurate models, generally used to perform nonlinear time history analyses, prevent a closed-form definition of parameters commonly used in optimization procedures, such as effective stiffness and damping. For the BRBs, an original mechanical model based on experimental data is here proposed and formulated in a closed form to be easily integrated into the optimization algorithm.

2. Structural optimization procedure

The general procedure is schematized in four consecutive phases as follows:



2.1. Phase 1: Design analysis phase. In this phase the variables involved in the optimization process are identified and defined as design variables and performance variables. The design variables are the final objectives of the optimization process while the performance variables are used to check the conformity of the structure with the performance requirements. The axial stiffness of the braces and their dissipative capacity together with their location in plan and in elevation are considered as design variables. The behavior of each dissipative brace is characterized by an effective damping ratio and an effective stiffness that will be optimized by the proposed algorithm.

The generic structural scheme consists in a three-dimensional structure with p floors ($k = 1 \dots p$) and m columns ($j = 1 \dots m$) for a total of $n = p(m - 1)$ structural bays, available to allocate the braces; the i -th brace ($i = 1 \dots n$) is located in the i -th structural bay, pinned or bolted to the frame.

The design variables to be optimized are stored in two vectors. The first one is the $n \times 1$ vector \mathbf{k} :

$$\mathbf{k} = [k_1 \ k_2 \ \dots \ k_i \ \dots \ k_n]^T \quad (2-1)$$

where k_i is the normalized axial stiffness of the i -th brace, given by:

$$k_i = \frac{K_i}{K_i^{\text{ref}}} \quad (2-2)$$

K_i is the axial stiffness of the i -th brace and K_i^{ref} is the axial stiffness associated with a conventional cross-sectional area used as a reference to initialize the procedure. The second $n \times 1$ vector $\boldsymbol{\xi}$ is defined as

$$\boldsymbol{\xi} = [\xi_1 \ \xi_2 \ \dots \ \xi_i \ \dots \ \xi_n]^T \quad (2-3)$$

where ξ_i is the damping ratio of the i -th brace. The total stiffness matrix $\mathbf{K}_{\text{tot}}(\mathbf{k}, \boldsymbol{\xi})$, condensed on the lateral displacement, and the total damping ratio of the structure $\xi_{\text{tot}}(\mathbf{k}, \boldsymbol{\xi})$ are considered as performance variables. The performance variables need to be expressed as a function of the design vectors \mathbf{k} and $\boldsymbol{\xi}$ in order to be implemented in the optimization algorithm. These correlations are proposed by Bonessio, where parametric analyses on the global stiffness matrix and on the total damping have been performed [Bonessio 2010].

2.2. Phase 2: The engineering phase. Several engineering boundaries on design and performance variables are set in the form of inequalities and equations. The design boundaries are expressed as

$$\mathbf{k} = [k_1 \ k_2 \ \dots \ k_i \ \dots \ k_n]^T \geq \mathbf{0}, \quad (2-4)$$

$$\boldsymbol{\xi} = [\xi_1 \ \xi_2 \ \dots \ \xi_i \ \dots \ \xi_n]^T \geq \mathbf{0}, \quad (2-5)$$

$$\xi_i = f_i(k_i) \quad \text{for } i = 1 \dots n. \quad (2-6)$$

Equations (2-4) and (2-5) express a physical limitation on stiffness and damping ratio, valid for all type of braces. The set of equations (2-6) is specific for the particular type of braces used and represents the correlation between effective stiffness and damping ratio, as formulated in the next paragraph for the BRBs. The accuracy of the mechanical model of the braces influences the optimum values of the design variables and consequently the efficiency of the earthquake protection system. The performance boundaries are inequalities that involve the performance variables $\mathbf{K}_{\text{tot}}(\mathbf{k}, \boldsymbol{\xi})$ and $\xi_{\text{tot}}(\mathbf{k}, \boldsymbol{\xi})$:

$$\bar{\mathbf{p}} \leq \mathbf{K}_{\text{tot}}(\mathbf{k}, \boldsymbol{\xi}) \cdot \bar{\mathbf{u}}, \quad (2-7)$$

$$\xi_{\text{tot}}(\mathbf{k}, \boldsymbol{\xi}) \leq \bar{\xi}_{\text{tot}} \quad (2-8)$$

where $\bar{\mathbf{p}}$ is a vector of assigned lateral loads, for each performance level, $\bar{\mathbf{u}}$ is the vector of the maximum allowable displacements, and $\bar{\xi}_{\text{tot}}$ is the maximum allowed damping ratio.

2.3. Phase 3: The objective selection phase. The definition of the objective of the design procedure represents the goal of this phase. For this application the objective is the cost-minimization of the protection system. The cost W of the system is mainly associated with the size of the braces and consequently related to their stiffness:

$$W(\mathbf{k}) = \mathbf{c}^T \mathbf{k} \quad (2-9)$$

where the vector $\mathbf{c}^T = [c_1 \ c_2 \ \dots \ c_i \ \dots \ c_n]$ includes information about the geometry and the material properties of the braces.

2.4. Phase 4: The solution phase. The final phase consists of the evaluation of the optimal numerical values for the design variables. For instance, for the sizing and topology optimization of a BRB protection system, a standard nonlinear programming (NLP) problem has to be solved. The sequential solution technique is proposed as a tool to treat the NLP problem as a linear programming problem [Bonessio 2010]. The generic formulation of the problem, in agreement with the classical format of mathematical programming, is expressed as follows, using equations (2-1) to (2-9):

$$\begin{aligned} & \text{Find } k_1, k_2, \dots, k_n \text{ and } \xi_1, \xi_2, \dots, \xi_n \\ & \text{minimizing } W(\mathbf{k}) = \mathbf{c}^T \mathbf{k} \\ & \text{subject to } \mathbf{k} \geq \mathbf{0}, \\ & \quad \quad \quad \boldsymbol{\xi} \geq \mathbf{0}, \\ & \quad \quad \quad \bar{p} \leq \mathbf{K}_{\text{tot}}(\mathbf{k}, \boldsymbol{\xi}) \cdot \bar{\mathbf{u}}, \\ & \quad \quad \quad \xi_1 = f_1(k_1), \dots, \xi_n = f_n(k_n). \end{aligned} \quad (2-10)$$

The procedure is able to determine the stiffness k_i and the damping ratio ξ_i of the brace placed in the i -th location of the frame, for a maximum of n braces in the n possible locations. In the allowable set of values for each design variable k_i , zero values is also included. This allows some of the n braces to be eliminated so topology of the protection system can also be optimized.

3. Experimental characterization

3.1. Specimens and testing protocol. A total of 3 sets A, B and C of full-scale specimens were tested, each set comprising two nominally identical specimens. Each specimen was composed of a central core plate, which was confined in a concrete-filled square hollow square section with different characteristics in terms the yield strength of core F_{ya} , the cross sectional area A and the lengths L_b, L_c, L_e, L_t, L_y referred to different portions of the brace, as shown schematically in Figure 1.

The devices were tested at the Caltrans SRMD Testing Facility, at the University of California San Diego campus, that consists of a 6 DOFs shaking table specifically designed for full scale testing of isolators and energy dissipators. The displacement range of the table in longitudinal direction is ± 1.22 m with a maximum horizontal capacity of 9,000 kN. The peak velocity of the table longitudinal motion is 1.8 m/s. The installation procedure of the devices on the testing machine is consistent with the standard installation of BRBs. The ends of each brace were spliced to a cruciform gusset bracket by high-strength bolts. Both the gusset plates on the specimen and on the connection were sandblasted to a Class B faying surface [AISC 1998]. Figure 2 shows the testing rig configuration. More information about the testing rig is provided in [Benzoni and Seible 1998].

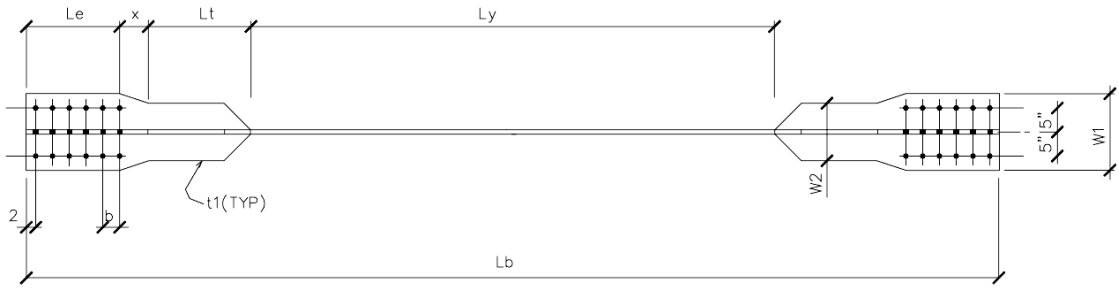


Figure 1. Layout of the central core plate of the test specimens.

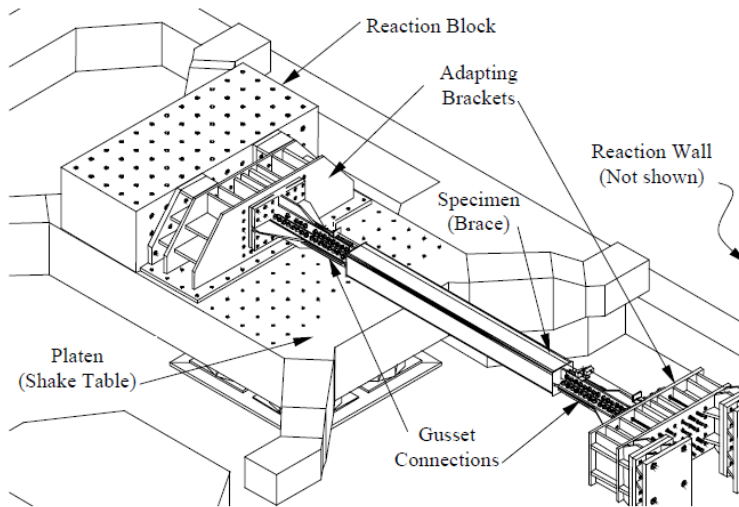


Figure 2. SRMD testing rig configuration.

A matrix of performed tests is presented in [Table 1](#). The loading sequence was chosen accordingly to the *Recommended Provisions for Buckling-Restrained Braces* [SEAOC-AISC 2001].

Displacement level	D1	D2	D3	D4	D5	D6	
Number of cycles	6	4	4	4	2	2	
Brace specimen	A1	12.7	20.3	38.1	50.8	77.7	88.1
	A2	12.7	20.3	38.1	50.8	77.7	88.1
	A3	12.7	20.3	38.1	50.8	81.3	95.3
	A4	12.7	20.3	38.1	50.8	81.3	95.3
	A5	12.7	20.3	38.1	50.8	81.3	88.1
	A6	12.7	20.3	38.1	50.8	81.3	88.1

Table 1. Shake table peak input displacements (mm).

3.2. Experimental and theoretical results. Experimental results in terms of effective stiffness and damping ratio are reported in Figures 3 and 4. Each parameter is presented as a function of the ductility level μ_Δ and compared with a theoretical value obtained from a bilinear model. The force-deformation relationship of BRBs is generally presented in literature as a bilinear relationship characterized by three terms: an elastic stiffness K_1 , a plastic stiffness $K_2 = \alpha K_1$, where α is the post-yielding ratio, and a yielding displacement

$$d_y = \frac{F_y}{K_1},$$

where F_y is the yielding force [Black et al. 2002; Kiggins and Uang 2006; Sabelli et al. 2003]. Using the bilinear model the relationship between the effective secant stiffness and the damping ratio with ductility can be written in a closed form. Accordingly, the theoretical value of the effective stiffness K_{eff} is obtained as a function of the displacement ductility μ_Δ :

$$K_{\text{eff}} = \begin{cases} K_1 & \text{for } 0 \leq \mu_\Delta < 1, \\ K_1 \frac{1 + \alpha(\mu_\Delta - 1)}{\mu_\Delta} & \text{for } \mu_\Delta \geq 1, \end{cases} \quad (3-1)$$

with $\mu_\Delta = d_{\text{max}}/d_y$, where d_{max} is the maximum displacement experienced during a deformation cycle. Similarly the damping ratio is given by

$$\xi_{\text{eff}} = \begin{cases} 0 & \text{for } 0 \leq \mu_\Delta < 1, \\ \frac{2}{\pi} \frac{(1 - \alpha)(\mu_\Delta - 1)}{[1 + \alpha(\mu_\Delta - 1)]\mu_\Delta} & \text{for } \mu_\Delta \geq 1. \end{cases} \quad (3-2)$$

In Figure 3, K_{eff} normalized to the elastic stiffness K_1 is reported versus the ductility term μ_Δ . The trend line, obtained as least-squares fit of the experimental data, is lower than the theoretical prediction (solid line) for ductility levels lower than 6. The peak variation in the ductility range between 1 and 2 is about 30%. In Figure 4, the theoretical values for ξ_{eff} under-estimates the experimental values for ductility levels lower than 2, while over-estimates test results for higher ductility.

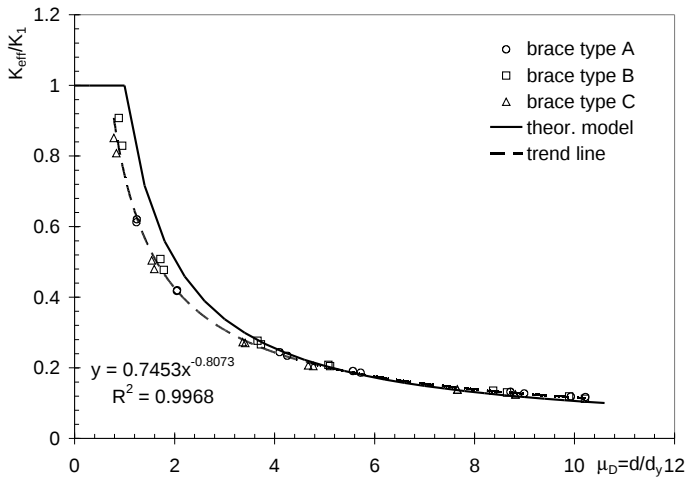


Figure 3. Normalized effective stiffness versus displacement ductility.

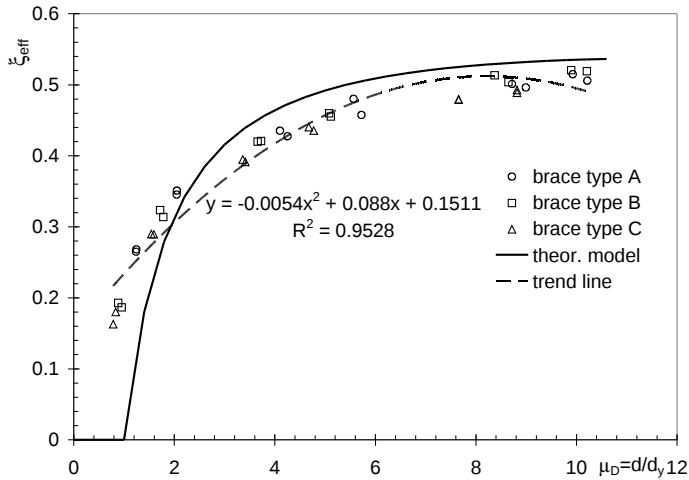


Figure 4. Damping ratio versus displacement ductility.

The relationship between the damping ratio and the effective stiffness generally indicated in equation (2-6) can be expressed as

$$\xi_{\text{eff}} = \frac{2 (1 - \alpha) (\mu_{\Delta} - 1) K_{\text{eff}}}{\pi [1 + \alpha (\mu_{\Delta} - 1)]^2 K_1} \tag{3-3}$$

The values of $\xi_{\text{eff}}/(K_{\text{eff}}/K_1)$ computed by this equation are compared with the experimental results in Figure 5 where the disagreement between theoretical and experimental data is clearly visible.

The theoretical ratio $\xi_{\text{eff}}/(K_{\text{eff}}/K_1)$ underestimates the experimental evidence for displacement ductility lower than 2.5 and overestimates the response for higher ductility levels.

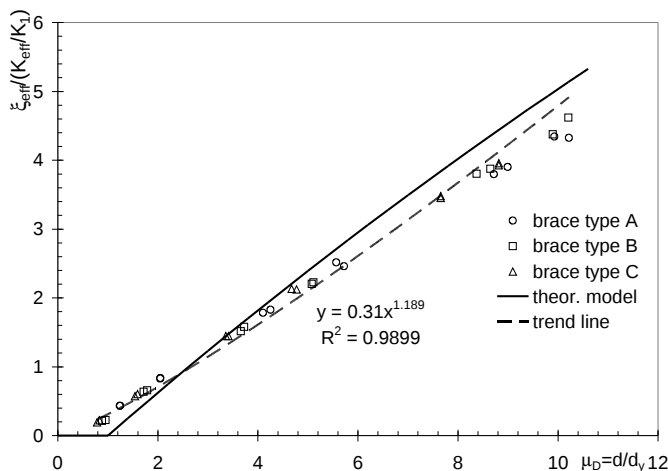


Figure 5. Ratio $\xi_{\text{eff}}/(k_{\text{eff}}/K_1)$ versus displacement ductility.

4. Discussion of experimental results and proposed model

Some of the previous observations can be organized and generalized in order to suggest an alternative analytical model of the device performance. In Figure 6 the force-displacement loops for specimen A1 are reported. The same curves are reorganized in Figure 7 after a bias with respect to the negative displacement at zero force. It can be noted the difference between the idealized and the actual response in the transition from the elastic to the plastic behavior. This difference is the main cause of the poor agreement between theoretical and experimental values for the effective stiffness and the damping ratio.

In Figure 8(a), in order to compare the effective force-displacement performance with the theoretical response, only the portion of the cycles with increasing force is plotted with a continuous line. The similarity of the curves for different specimens appears evident by using normalized forces F/F_y and

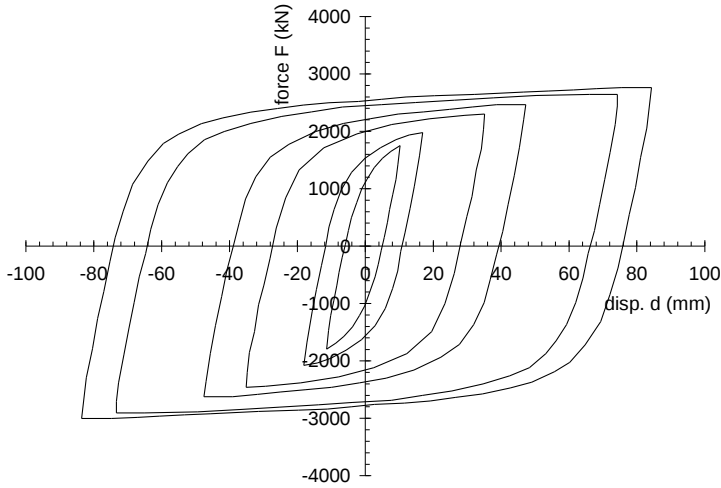


Figure 6. Experimental data for specimen A1.

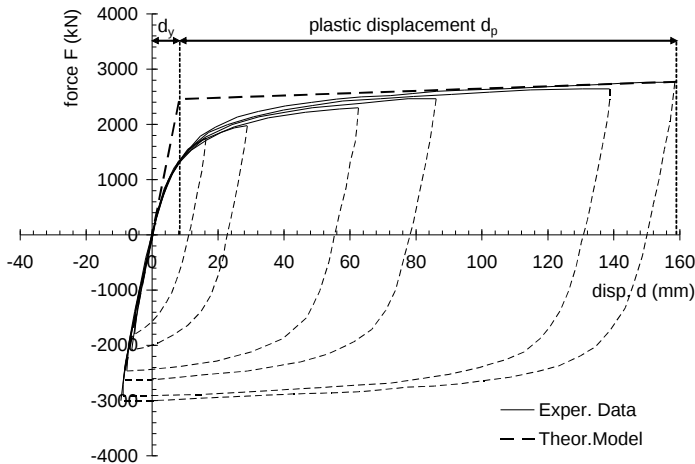


Figure 7. Experimental data and idealized response for specimen A1.

displacement ductility $\mu_{\Delta} = d/d_y$. The average values and the relative 95% confidence interval are reported in Figure 8(b).

The error of the bilinear model in terms of normalized forces over the whole ductility range is represented in Figure 9. As expected, the maximum errors occur at the yielding displacement. The average curve indicates a peak error approximately 45% of the yielding force. To improve the agreement between experimental and theoretical loops, a hysteretic function z was introduced. The function describes the transition from the elastic and the plastic phase and a force-displacement relationship can be proposed as

$$F = \alpha \cdot K_1 \cdot d + (1 - \alpha) \cdot F_y \cdot z, \quad (4-1)$$

where K_1 is the elastic stiffness, F_y is the yield force, α is the ratio of post-yield stiffness to elastic

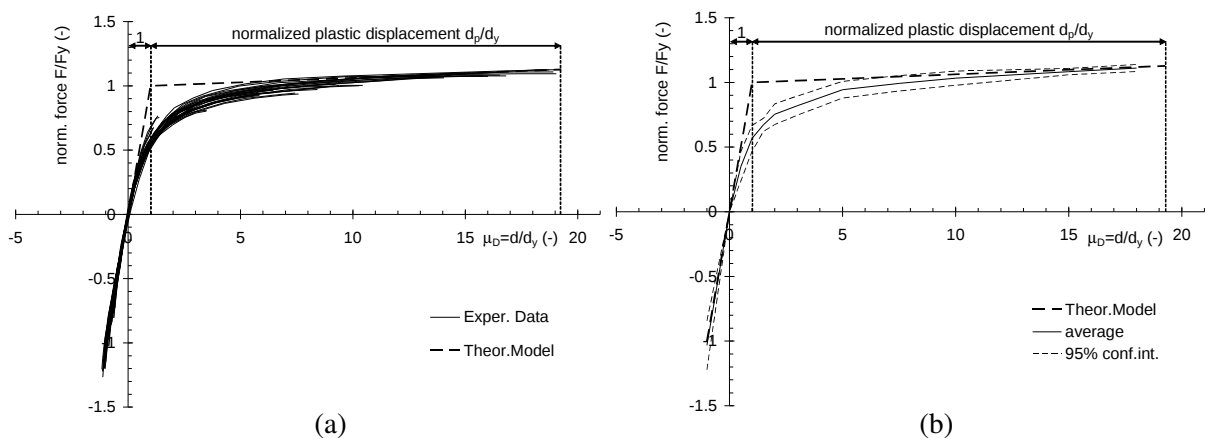


Figure 8. Normalized force-displacement curves: (a) curves for all the specimens and (b) average values and 95% confidence interval.

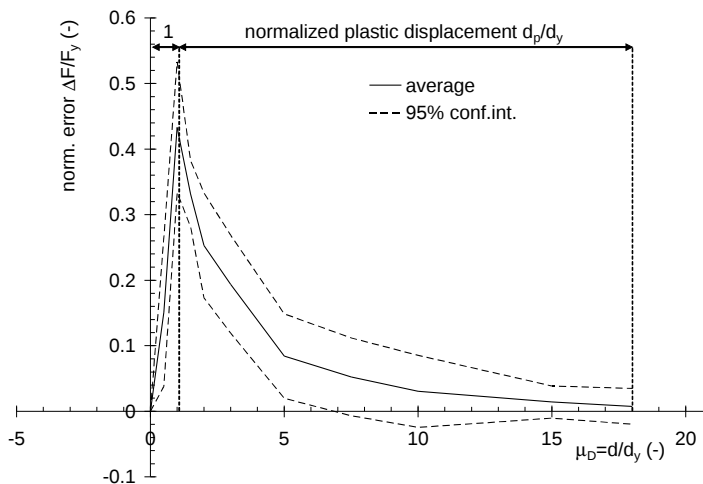


Figure 9. Normalized errors of the bilinear model.

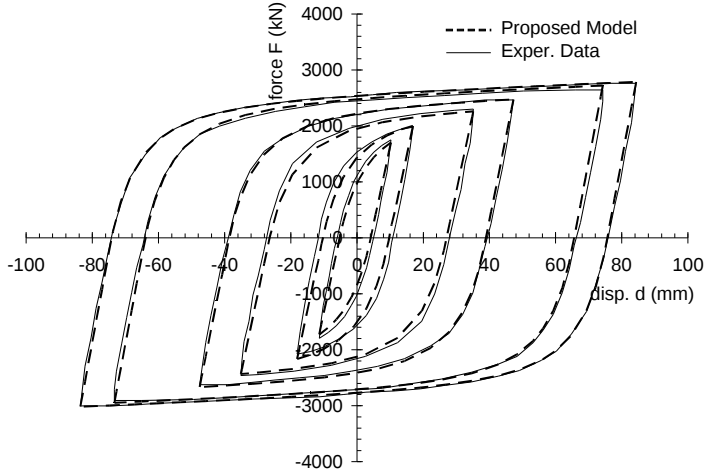


Figure 10. Comparison between theoretical and experimental loops.

stiffness and z is the hysteretic internal strain-dependent function, ranging from -1 and 1 , with the yield surface represented by $|z| = 1$.

The function z is defined as

$$z = \frac{1}{2} \cdot \left(\frac{\dot{d}}{|\dot{d}|} - \frac{d}{|d|} \right) + \frac{1}{2} \cdot \left(\frac{\dot{d}}{|\dot{d}|} + \frac{d}{|d|} \right) \cdot \left[1 - \left(\frac{\beta + \bar{d}/d_y}{\beta} \right)^{-\beta} \right], \quad (4-2)$$

where \bar{d} is the displacement measured from the last change in the velocity sign and the parameter $\beta > 1$ is obtained experimentally and controls the shape of the transition curve from the elastic to the plastic phase. For the specific results of this study, the value $\beta = 2$ was used.

In [Figure 10](#) the predicted force-displacement loops are presented with a dashed line in comparison with the experimental curves for the brace type A1.

According with the proposed model, the relationship between the normalized effective stiffness and the damping ratio with the displacement ductility μ_Δ can be written as

$$K_{\text{eff}} = K_1 \frac{\gamma + \alpha (\mu_\Delta - \gamma)}{\mu_\Delta}, \quad (4-3)$$

$$\xi_{\text{eff}} = \frac{2}{\pi} \frac{(1 - \alpha) (\mu_\Delta - \delta)}{[\gamma + \alpha (\mu_\Delta - \gamma)] \mu_\Delta}, \quad (4-4)$$

where

$$\gamma = 1 - \left(\frac{\beta + 2\mu_\Delta - x}{\beta} \right)^{-\beta} < 1, \quad (4-5)$$

$$x = 1 - \left(1 + \frac{\mu_\Delta}{\beta} \right)^{-\beta} < 1, \quad (4-6)$$

$$\delta = \frac{1}{2} \left[x + \frac{\beta}{1 - \beta} \left(\frac{\beta + 2\mu_\Delta - x}{\beta} \right)^{-\beta} - \frac{\beta}{1 - \beta} + \frac{x^2}{2} \right]. \quad (4-7)$$

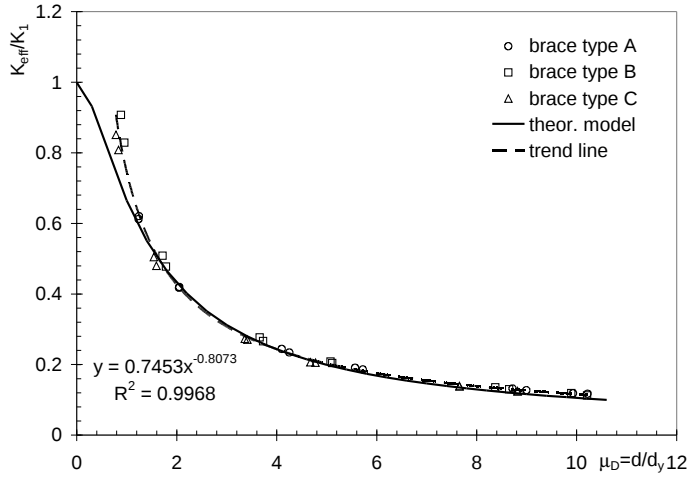


Figure 11. Normalized effective stiffness versus displacement ductility from experimental data and proposed model.

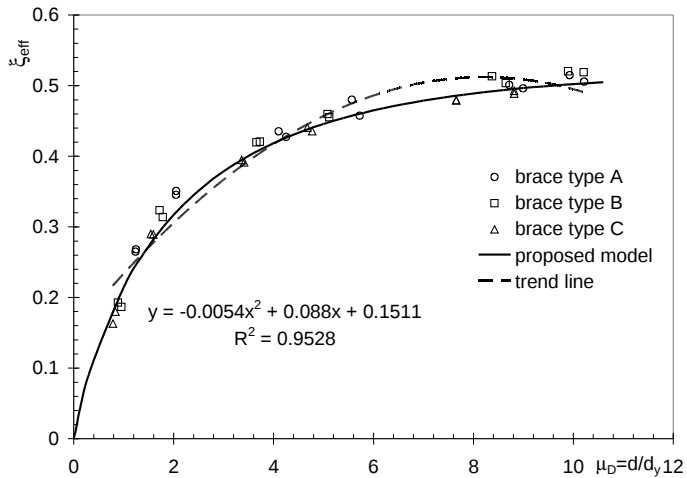


Figure 12. Damping ratio versus displacement ductility from experimental data and proposed model.

Equations (4-3) and (4-4) for the effective stiffness and damping ratio appear similar to equations (3-1) and (3-2), for the bilinear model, but take in account the smooth transition between the elastic and the plastic phase by means of the parameters γ and δ . The normalized stiffness and damping ratio predicted by using the proposed model fit well the experimental results, as shown in Figures 11 and 12, respectively.

From equations (4-3) and (4-4) the relationship between the damping ratio and the effective stiffness normalized to the elastic stiffness can be obtained as

$$\xi_{\text{eff}} = \frac{2}{\pi} \frac{(1 - \alpha)(\mu_{\Delta} - \delta)}{[\gamma + \alpha(\mu_{\Delta} - \gamma)]^2} \frac{K_{\text{eff}}}{K_1}. \quad (4-8)$$

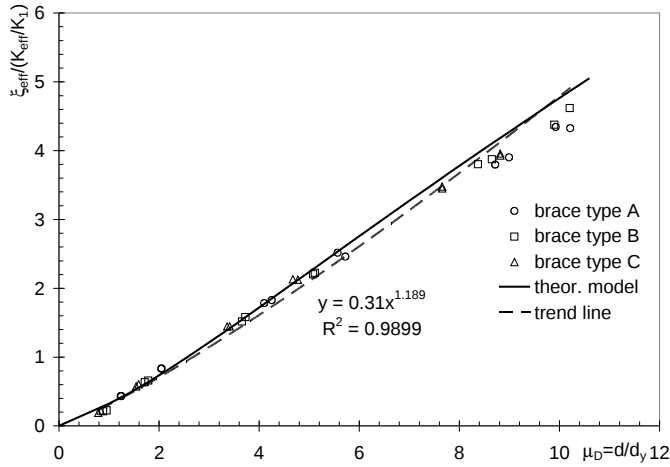


Figure 13. Ratio $\xi_{\text{eff}}/(k_{\text{eff}}/K_1)$ versus displacement ductility from experimental data and proposed model.

Values predicted by equation (4-8) are consistent with experimental results and are represented in Figure 13 versus the displacement ductility.

Equation (4-8) can be expressed in an implicit form for a generic i -th BRB as

$$\xi_i = f_{\text{BRB}}(k_i) \quad (4-9)$$

where $k_1 = K_{\text{eff}}/K_i$ is the normalized axial stiffness of the i -th BRB. Equation (4-9) is used in the optimization procedure for the design of the BRBs, where ξ_i and k_i are the design variables to be optimized.

5. Numerical case study for procedure validation

A simple structure is presented in order to show an application of the optimization procedure for BRBs in conformity with the multi-performance design philosophy. The structure consists of a single span-two floors frame subjected to horizontal loads. The whole system has 10 DOFs since the beam is assumed axially rigid, as indicated in Figure 14. Values of the material properties for the beam and columns

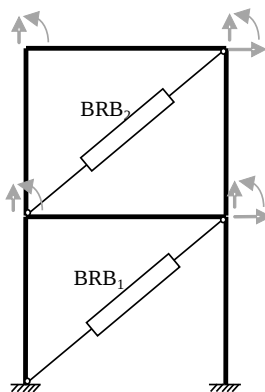


Figure 14. MDOF frame case study.

elements were selected as follows: $E = 30,000$ MPa; Poisson ratio $\nu = 0.25$. The beams have a length of 4 m and a rectangular cross-sectional area of 30×50 cm while the columns have a height of 3 m with a rectangular cross-sectional area of 30×50 cm. The optimization problem consists in the sizing of the two BRBs, 5 m long, pinned to the frames. Two allowable locations for the braces are considered, 1st floor and 2nd floor, for a total of 4 possible topology configurations for the braces (i.e., on each floor, on the 1st floor only, on the 2nd floor only, and nowhere).

The design problem has four design variables, i.e., the damping ratios ξ_1 , ξ_2 and the axial stiffnesses k_1 and k_2 for the 1st and 2nd floor braces, respectively.

The optimization problem to be solved in this case study is a nonlinear programming problem expressed as

$$\begin{aligned}
 & \text{Find } k_1, k_2, \xi_1, \xi_2 \\
 & \text{minimizing } k_1 + k_2 \\
 & \text{subject to } [k_1 \ k_2] \geq \mathbf{0}, \\
 & \quad [\xi_1 \ \xi_2] \geq \mathbf{0}, \\
 & \quad \bar{\mathbf{p}} \leq \mathbf{K}_{\text{tot}}(k_1, k_2, \xi_1, \xi_2) \cdot \bar{\mathbf{u}}, \\
 & \quad \xi_1 = f_{\text{BRB}}(k_1), \\
 & \quad \xi_2 = f_{\text{BRB}}(k_2).
 \end{aligned} \tag{5-1}$$

The vectors $\bar{\mathbf{p}}$ and $\bar{\mathbf{u}}$ represent the assigned seismic actions and the limit displacements defined for each performance level. Four levels, named Operational (O), Immediate Occupancy (IO), Life Safety (LS) and Collapse Prevention (CP), are considered [ASCE/SEI 2007]. The corresponding four levels of seismic actions are associated with the probability of exceedance of 50%, 20%, 10% and 2% in 50 years, respectively. Elastic spectra on soil type A from Eurocode 8 [CEN 2004] were used to represent seismic actions. The four sets of limit displacements are consistent with the limit drifts of 0.2%, 0.5%, 1.5% and 2.5%.

The correlation between damping ratio and axial stiffness for each BRB is established through the function f_{BRB} as indicated in (4-9) by assuming the values of α and β equal to 0.007 and 2, respectively.

The sequential solution technique and then the simplex method is applied to determinate the optimal values of the design variables, reported in Table 2 for each performance level.

The cross-sectional areas of the BRB central cores corresponding to the identified values of stiffness and damping ratio are 2.54 cm^2 and 1.61 cm^2 for the 1st and 2nd floor respectively, being the area of the 1st floor brace 1.58 times the area of the 2nd floor brace.

In order to validate the obtained design solution, a nonlinear finite element model of the structure equipped with BRBs has been carried out. For each performance level, seven ground motions were selected by means of specialized software in order to obtain an average acceleration spectrum matching the elastic design spectrum [Gasparini and Vanmarcke 1976]. The results in terms of displacement ductility of the braces and average values of the interstorey drifts are reported in Table 3 for each performance level.

From the results, it should be noted that the BRBs exceed the yielding displacement ($\mu_{\Delta} \geq 1$) only in the Life Safety and Collapse Prevention performance levels. The maximum displacement ductility

Performance level	Normalized stiffness k_i		Damping ratio ξ_i	
	1st floor	2nd floor	1st floor	2nd floor
FO	2.46	1.56	5.0%	4.8%
O	2.16	1.38	12.9%	12.6%
LS	1.28	0.80	28.3%	27.7%
CP	0.85	0.55	34.5%	33.2%

Table 2. BRB characteristics for each performance level.

Performance level	Displ. ductility $\mu_{\Delta,i}$		Interstorey drift	
	1st floor	2nd floor	1st floor	2nd floor
FO	0.22	0.22	0.20%	0.20%
O	0.54	0.54	0.50%	0.50%
LS	1.64	1.62	1.49%	1.45%
CP	2.75	2.70	2.51%	2.33%

Table 3. Displacement ductility and interstorey drifts for each performance level.

demand is 2.75, corresponding to an effective damping ratio of 34.5%. According to the experimental results, significant energy dissipation ($\xi = 12.6\%$ in Table 2) was found also for the Operational Performance level, even if the yielding displacement has not been exceeded ($\mu_{\Delta} = 0.54$ in Table 3). The average interstorey drift respects the imposed limits, and the drift-control performed by BRBs at the upper level is even more effective, as it is evident by the lower values of interstorey drifts found at the 2nd floor.

6. Conclusion

The performance of three different typologies of BRBs at several levels of plastic deformation was studied. Experimental results were compared with the bilinear model generally used for this kind of braces. A significant difference between the actual and the predicted values, in terms of stiffness and dissipated energy, was noticed, for the tested devices. By using the bilinear idealization for the force-displacement loops of the BRBs, the predicted stiffness reached a peak 30% higher than the experimental one. The dissipated energy appeared underestimated for ductility level lower than 2 and overestimated for higher ductility level, with a maximum disagreement of approximately 15% for a ductility level around 3.

A simplified model for the force-displacement loops has been proposed and it proved able to estimate the variation of stiffness and energy dissipated per cycle with the displacement induced in the brace. By using this model, the relationship between stiffness and damping ratio of BRB systems was written in a closed form expression, suitable for use in an optimization procedure for the design of BRB equipped structures.

The optimization procedure allows the assessment of size and position of the braces for the retrofit of an existing structure. The procedure follows a multi-performance approach, and the retrofitted structure complies with several performance requirements. The design procedure and the proposed model were

applied to a simple two-stories building and led to BRBs with a cross-sectional area 58% greater at the first floor than at the second. The maximum ductility demand obtained was 2.75 at the first floor. In the case study, the average interstorey drifts computed by a finite element analysis respected the imposed limit values. The procedure appears feasible for the application on more complex structures.

References

- [AISC 1998] “Manual of steel construction: load and resistance factor design”, American Institute of Steel Construction, Chicago, 1998.
- [ASCE/SEI 2007] “Seismic rehabilitation of existing buildings”, SEI 41-06, American Society of Civil Engineers, Reston, VA, 2007.
- [Benzoni and Seible 1998] G. Benzoni and F. Seible, “Design of the Caltrans Seismic Response Modification Device (SRMD) test facility”, in *Proceedings of the USA-Italy Workshop on Protective Systems*, 1998.
- [Black et al. 2002] C. Black, N. Makris, and I. Aiken, PEER report 2002/08, University of California, Berkeley, 2002, Available at <http://nisee.berkeley.edu/elibrary/Text/1276943>.
- [Bonessio 2010] N. Bonessio, *Structural optimization procedure for the design of earthquake protection system*, Ph.D. thesis, Department of Civil Engineering, University of Rome La Sapienza, Rome, 2010.
- [Breitung et al. 1998] K. Breitung, F. Casciati, and L. Faravelli, “Reliability based stability analysis for actively controlled structures”, *Eng. Struct.* **20** (1998), 211–215.
- [CEN 2004] *Eurocode 8: Design of structures for earthquake resistance - Part 1: General rules, seismic actions and rules for buildings*, EN 1998-1:2004, European Committee for Standardization, Brussels, 2004, Available at <http://tinyurl.com/bs-en-1998-1-2004>.
- [Fahnestock et al. 2004] L. A. Fahnestock, R. Sause, J. M. Ricles, and L. W. Lu, “Ductility demands on buckling-restrained braced frames under earthquake loading”, *J. Earthquake Eng. Eng. Vib.* **2:2** (2004), 255–268.
- [Frangopol 1995] D. M. Frangopol, “Reliability based optimum structural design”, pp. 352–387 (Chapter 16) in *Probabilistic structural mechanics handbook*, Springer, New York, 1995.
- [Fu and Frangopol 1990] G. Fu and D. M. Frangopol, “Reliability-based vector optimization of structural systems”, *J. Struct. Eng. (ASCE)* **116:8** (1990), 2143–2161.
- [Gasparini and Vanmarcke 1976] D. Gasparini and E. Vanmarcke, “Simulated earthquake motions compatible with prescribed response spectra”, technical report 76-4, Massachusetts Institute of Technology, Department of Civil Engineering, Cambridge, MA, 1976.
- [Kiggins and Uang 2006] S. Kiggins and C. Uang, “Reducing residual drift of buckling-restrained braced frames as a dual system”, *Eng. Struct.* **28** (2006), 1525–1532.
- [Lomiento et al. 2010] G. Lomiento, N. Bonessio, and F. Braga, “Design criteria for added dampers and supporting braces”, *Seismic Isol. Protective Syst.* **1** (2010), 55–75.
- [Lopez and Sabelli 2004] W. A. Lopez and R. Sabelli, “Seismic design of buckling restrained braced frames”, *Steel TIPS* technical report, Structural Steel Education Council, 2004, Available at http://www.steeltips.org/steeltips/tip_details.php?id=76.
- [Sabelli 2001] R. Sabelli, “Research on Improving the Design and Analysis of Earthquake-Resistant Steel Braced Frames”, EERI/FEMA NEHRP Fellowship Report, Earthquake Engineering Research Institute, Oakland, CA, 2001.
- [Sabelli et al. 2003] R. Sabelli, S. A. Mahin, and C. Chang, “Seismic demands on steel braced-frame buildings with buckling-restrained braces”, *Eng. Struct.* **25** (2003), 655–666.
- [SEAOC-AISC 2001] SEAOC and AISC, “Recommended provisions for buckling-restrained braced frames”, draft, 2001.
- [Soong and Dargush 1997] T. T. Soong and G. F. Dargush, *Passive energy dissipation systems in structural engineering*, Wiley, Chichester, UK, 1997.
- [Thoft-Christensen and Sorensen 1987] P. Thoft-Christensen and J. D. Sorensen, “Optimal strategy for inspection and repair of structural systems”, *Civil Eng. Systems* **4:2** (1987), 94–100.

[Tremblay et al. 2004] R. Tremblay, L. Poncet, P. Bolduc, R. Neville, and R. D. Vall, “Testing and design of buckling restrained braces for Canadian application”, in *Proceedings of the 13th World Conference on Earthquake Engineering* (Vancouver, 2004), Earthquake Engineering Conference Secretariat Canada, 2004.

[Wada et al. 1998] A. Wada, E. Saeki, T. Takeuchi, and A. Watanabe, “Development of unbonded brace”, pp. 1–16 in *Nippon Steel’s unbonded braces*, Nippon Steel Corporation Building Construction and Urban Development Division, Tokyo, 1998.

Received 9 Aug 2011. Accepted 5 Oct 2011.

NOEMI BONESSIO: nbonessio@eng.ucsd.edu

Department of Structural Engineering, University of California San Diego, La Jolla, CA 92093-0085, United States

GIUSEPPE LOMIENTO: glomiento@eng.ucsd.edu

Department of Structural Engineering, University of California San Diego, La Jolla, CA 92093-0085, United States

GIANMARIO BENZONI: gbenzoni@ucsd.edu

Department of Structural Engineering, University of California San Diego, La Jolla, CA 92093-0085, United States

SUBMISSION GUIDELINES

ORIGINALITY

Authors may submit manuscripts in PDF format online at the Submissions page. Submission of a manuscript acknowledges that the manuscript is original and has neither previously, nor simultaneously, in whole or in part, been submitted elsewhere. Information regarding the preparation of manuscripts is provided below. Correspondence by email is requested for convenience and speed.

LANGUAGE

Manuscripts must be in English. A brief abstract of about 150 words or less must be included. The abstract should be self-contained and not make any reference to the bibliography. Also required are keywords and subject classification for the article, and, for each author, postal address, affiliation (if appropriate), and email address if available. A home-page URL is optional.

FORMAT

Authors can use their preferred manuscript-preparation software, including for example Microsoft Word or any variant of $\text{T}_{\text{E}}\text{X}$. The journal itself is produced in $\text{L}_{\text{A}}\text{T}_{\text{E}}\text{X}$, so accepted articles prepared using other software will be converted to $\text{L}_{\text{A}}\text{T}_{\text{E}}\text{X}$ at production time. Authors wishing to prepare their document in $\text{L}_{\text{A}}\text{T}_{\text{E}}\text{X}$ can follow the example file at www.jomms.org (but the use of other class files is acceptable). At submission time only a PDF file is required. After acceptance, authors must submit all source material (see especially Figures below).

REFERENCES

Bibliographical references should be complete, including article titles and page ranges. All references in the bibliography should be cited in the text. The use of $\text{BibT}_{\text{E}}\text{X}$ is preferred but not required. Tags will be converted to the house format (see a current issue for examples); however, for submission you may use the format of your choice. Links will be provided to all literature with known web locations; authors can supply their own links in addition to those provided by the editorial process.

FIGURES

Figures must be of publication quality. After acceptance, you will need to submit the original source files in vector format for all diagrams and graphs in your manuscript: vector EPS or vector PDF files are the most useful. (EPS stands for Encapsulated PostScript.)

Most drawing and graphing packages—Mathematica, Adobe Illustrator, Corel Draw, MATLAB, etc.—allow the user to save files in one of these formats. Make sure that what you're saving is vector graphics and not a bitmap. If you need help, please write to graphics@mathscipub.org with as many details as you can about how your graphics were generated.

Please also include the original data for any plots. This is particularly important if you are unable to save Excel-generated plots in vector format. Saving them as bitmaps is not useful; please send the Excel (.xls) spreadsheets instead. Bundle your figure files into a single archive (using zip, tar, rar or other format of your choice) and upload on the link you been given at acceptance time.

Each figure should be captioned and numbered so that it can float. Small figures occupying no more than three lines of vertical space can be kept in the text (“the curve looks like this:”). It is acceptable to submit a manuscript with all figures at the end, if their placement is specified in the text by means of comments such as “Place Figure 1 here”. The same considerations apply to tables.

WHITE SPACE

Forced line breaks or page breaks should not be inserted in the document. There is no point in your trying to optimize line and page breaks in the original manuscript. The manuscript will be reformatted to use the journal's preferred fonts and layout.

PROOFS

Page proofs will be made available to authors (or to the designated corresponding author) at a Web site in PDF format. Failure to acknowledge the receipt of proofs or to return corrections within the requested deadline may cause publication to be postponed.

<i>A tribute to Dr. William H. (Bill) Robinson</i> Bill Robinson	1
<i>Lead-rubber hysteretic bearings suitable for protecting structures during earthquakes</i> William H. Robinson	5
<i>The use of tests on high-shape-factor bearings to estimate the bulk modulus of natural rubber</i> James M. Kelly and Jiun-Wei Lai	21
<i>Passive damping devices for earthquake protection of bridges and buildings</i> Christian Meinhardt, Daniel Siepe and Peter Nawrotzki	35
<i>Report on the effects of seismic isolation methods from the 2011 Tohoku–Pacific earthquake</i> Yutaka Nakamura, Tetsuya Hanzawa, Masanobu Hasebe, Keiichi Okada, Mika Kaneko and Masaaki Saruta	57
<i>An experimental model of buckling restrained braces for multi-performance optimum design</i> Noemi Bonessio, Giuseppe Lomiento and Gianmario Benzoni	75